Rotating heat pipe with Dowtherm A for intermediate temperature applications in a heat pipe assisted annealing process

An experimental study on internal heat transfer with attention for the effects of non-condensable gas described by a computational model

by

F.P.M. Verbeek

Master of Science

Sustainable Process & Energy Technology

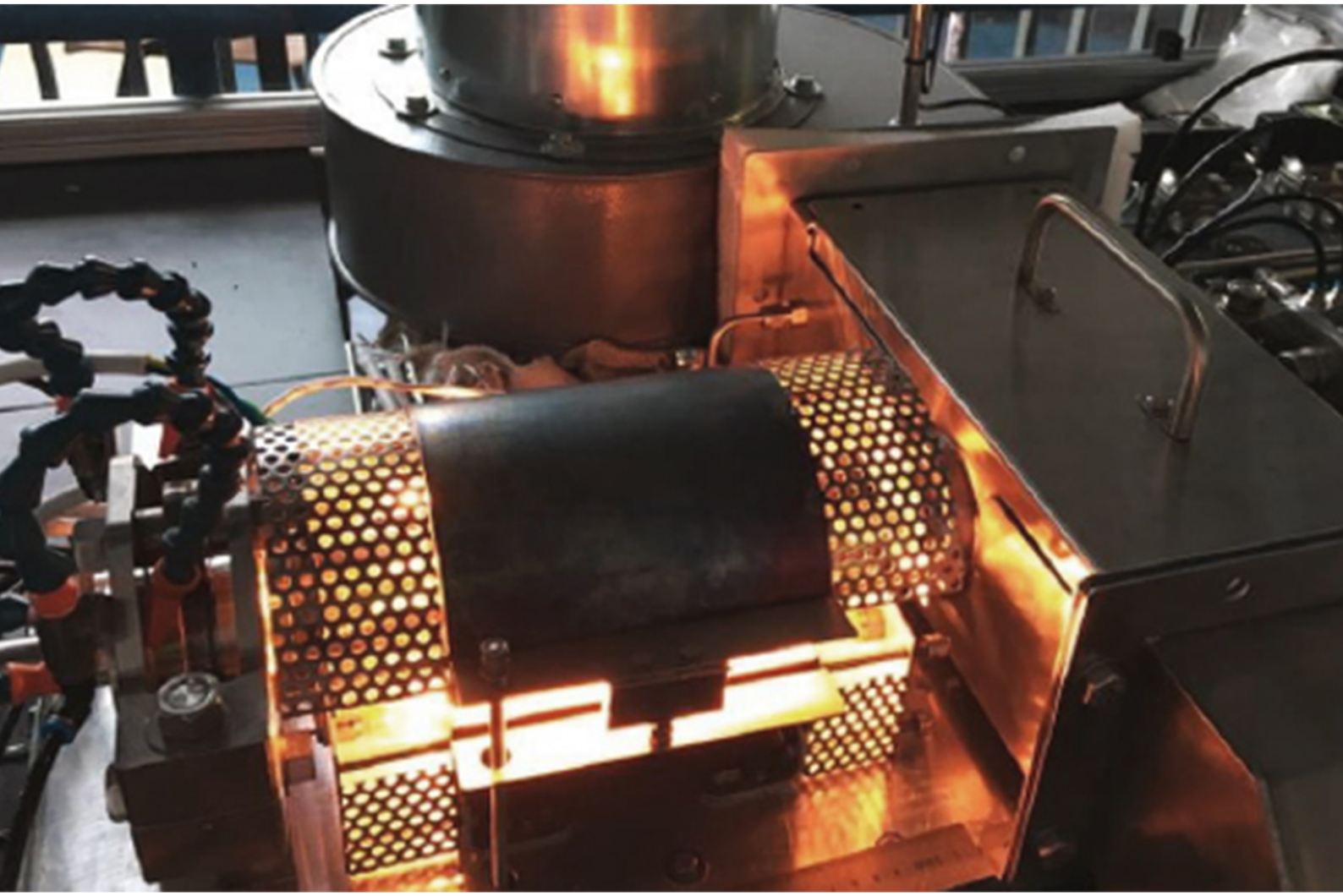

TATA STEEL

TU Delft Delft University of Technology

Rotating Heat Pipe with Dowtherm A for intermediate temperature applications in a heat pipe assisted annealing process

An experimental study on internal heat transfer with attention for the effects of non-condensable gas described by a computational model

by

F.P.M. Verbeek

to obtain the degree of Master of Science
at the Delft University of Technology,
to be defended publicly on Monday August 24, 2020 at 2:00 PM.

Student number:	4239482	
Project duration:	September 12, 2018 – August 24, 2020	
Thesis committee:	Prof. dr. ir. W. de Jong,	TU Delft, supervisor
	Dr. ir. M. Çelik,	TU Delft & TATA Steel, daily supervisor
	Prof. dr. ir. B.J. Boersma,	TU Delft
	Dr. R. Delfos,	TU Delft

This thesis is confidential and cannot be made public until August 24, 2022.

TU Delft

Preface

The study presented in this thesis has been part of a larger project led by the R&D group of Tata Steel Europe and is a collaboration between Tata Steel, Drever International and TU Delft. Geert Paulussen of Tata Steel Europe has invented the heat pipe assisted annealing concept.
Directly from the start I was not only involved in work at TU Delft, but I was also regularly invited to team meetings and discussions at Tata Steel, which I have enjoyed to the fullest and which is an extra valuable experience. I want to thank Metin Çelik for the guidance, which was very pleasant and we had many good and interesting discussions about the project. I also want to thank professor Wiebren de Jong and Geert Paulussen for the fruitful conversations we had, which definitely contributed to this research. Special thanks to Bas Overtoom for the continuous work we carried out to achieve successful heat pipe experiments, which turned out to be challenging. Furthermore, I was happy with the support from family, friends and Geerte.

F.P.M. Verbeek
Delft, August 2020

Abstract

The production of steel is an energy intensive process, using 20GJ/tonne of steel. The energy use needs to be declined by 10% in 2030 in order to be on track of the Sustainable Development Scenario(SDS). About 1GJ/tonne is required today by the annealing process, a heat treatment in which the steel strip is heated to a temperature of about 600-700°C and cooled afterwards. Tata Steel came up with a way of connecting the cooling and heating section in an innovative way, which can potentially reduce the energy requirements of an annealing line by up to 70%. Horizontal rotating heat pipes are proposed to transfer heat efficiently over its axial length from the strip in the cooling section to the strip in the heating section. Dowtherm A has been selected as the working fluid between 150 and 350°C. No research is available on rotating heat pipes with Dowtherm A.

The aim of this study is to research the relevant internal heat transfer characteristics of a rotating heat pipe and gain insight into the performance of Dowtherm A as the working fluid in terms of heat transfer efficiency. Furthermore, the aim is to gain knowledge on the effect of non-condensable gas inside a heat pipe and on the way the effects can be modelled in a computationally efficient way. Non-condensable gas is likely to be of influence on heat transfer homogeneity outwards to the relatively cool steel strip. Understanding this influence is another goal of this study.

To fulfil the aims of this study, experiments are conducted and a computational model is devised. An experimental setup with working fluid Dowtherm A is used to acquire data at different rotational speeds, operating temperatures and at different thermal inputs and outputs. The rotating heat pipe used is of smaller scale than one in a heat pipe assisted annealing line, but with comparable heat fluxes. Secondly, the devised model is used to both qualitatively and quantitatively study the effect of non-condensable gas for different operating parameters and non-condensable gas amounts, which is done for conditions as in the experimental setup and as in a heat pipe assisted annealing line.

The rotating heat pipe worked successfully during conducted experiments and Dowtherm A has shown to be able to transport at least 280W axially through the inner geometry in the non-annular flow regime, which is 192,000W/m^2 and corresponds to a vapor flow of 0.001kg/s, at an axial temperature difference of only a few degrees Celsius. Nucleate boiling was considered the dominant heat transfer mechanism through the film in the evaporator, with a typical heat transfer coefficient observed of 4200W/m^{2}K. The condenser has shown a lower film heat transfer coefficient; 1750W/m^{2}K. The effect of rotational speed, power and temperature is minor in the evaporator at conditions tested. The 1D model for determining non-condensable gas distribution showed good agreement with reported experimental data, which show a major axial temperature drop at the condenser end. It was shown that wall conduction influences non-condensable gas distribution for heat pipes with a relatively thick wall, which is modelled by the addition of wall temperature calculations to the 1D model. The effect of non-condensable gas on heat pipe performance showed to be strongly dependent on operating temperature.

Axial convective transport showed to be between two and three orders of magnitude more efficient than pure conduction. Homogeneous heat outflow is achieved when non-condensable gas is not present in the condenser, which can be achieved by extending the heat pipe at the condenser end. The devised model is suitable to predict the effect of operating conditions and design adjustments in an efficient way. Results have shown that Dowtherm A is a suitable working fluid for a heat pipe assisted annealing line, due to the low internal resistances to heat and mass transfer.

Contents

Nomenclature

Roman symbols

A	Area	m^2
C	Sum of axial conductivity-area products of wall and liquid	Wm/K
Ca	Capillary number	
c	Molar concentration	$kmol/m^3$
c_p	Specific heat	J/kgK
D	Diffusion coefficient	m^2/s
d	Diameter	m
E	Emissive power	W/m^2
Fr	Froude number	
Ga	Galileo number	
g	Gravitational acceleration	$9.81 m/s^2$
h	Heat transfer coefficient	$W/(m^2K)$
h_{fg}	Latent heat of vaporization	J/kg
Ja	Jakob number	
K	Radial conductivity through film and wall per unit length	W/mK
k	Heat conductivity	$W/(mK)$
L	Length	m
M	Molar mass	$kg/kmol$
m	Mass	kg
$\dot{m}$	Mass flow condensable	kg/s
Nu	Nusselt number	
P	Power	W
Pr	Prandtl number	
p	Absolute Pressure	Pa
Q	Heat flow	W
q	Heat flux	W/m^2
R	Universal gas constant	$8314\ J/(kmolK)$
Ra	Rayleigh number	
Re	Reynolds number	

r	Radial location / radius	m
r_v	Radius of vapor-liquid interface	m
T	Temperature	K
T_0	h_{fg}/R	K
V	Volume	m^3
v	Velocity	m/s
υ	Specific volume	m^3/kg
x	Mole fraction	
z	Axial location	m

Greek symbols

α	Thermal diffusivity	m^2/s
$\breve{\alpha}$	Thermal expansion coefficient solid	$1/K$
β	Thermal expansion coefficient gas/liquid	$1/K$
δ	Liquid film thickness	m
$\overline{\delta}$	Average liquid thickness (including pool)	m
ϵ	Emissivity	
θ	Angular region of wall covered by pool	rad
M	Figure of merit working fluid	
μ	Dynamic viscosity	$Pa\ s$
ν	Kinematic viscosity	m^2/s
ξ	Surface fraction of wall not covered by pool	
ρ	Density	kg/m^3
σ	Surface tension	N/m
σ	Stefan-Boltzmann constant	$5.6703 * 10^{-8}\ W/m^2K^4$
ϕ	Transformed variable for x_g	
χ	Filling ratio (V_l/V_{tot})	
Ω	Angular velocity	rad/s

Subscripts

air	Air property
$cond$	Condensation
cs	Cross-section
ev	Evaporator
fan	Cooling duct air property
g	Non-condensable gas property

i	Inside sensor, iteration number
l	Liquid
v	Condensable vapor property / property of vapor space of heat pipe
w	Wall property / wall sensor
wi	Inner wall
wo	Outer wall

1

Introduction

Steel is one of the main materials we see in objects throughout our daily life and for many applications one cannot do without it, due to its favorable material characteristics, raw material availability and relatively low cost. Steel started to be used and produced on a large scale from the industrial revolution onward and global production has grown incessantly. Figure 1.1 shows the increasing annual global steel production over past years and decades from which it is clear that growth still continuous today. It also shows that the energy required to produce a tonne of steel has decreased significantly over the past decades. The production of steel is an energy intensive process, today costing about 20GJ/tonne, which is 20-40% of the total production costs[4]. The energy intensity of steel production needs to be declined by 10% in 2030 in order to be on track of the sustainable development scenario(SDS). For this, it is needed to focus on recycling steel and to increase energy efficiency throughout the production process[6].
The study presented in this report focuses on the annealing process of steel and is part of a larger project where Tata Steel, Drever international and TU Delft collaborate to research this specific innovation, which has the potential to significantly decrease energy intensity of the annealing process, bringing along a reduction in production costs as well.

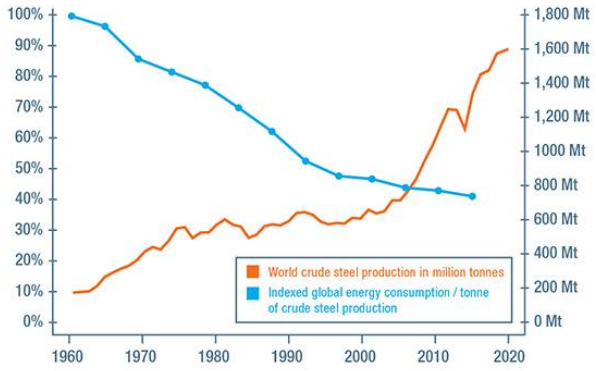

Figure 1.1: Global steel production over the past 60 years and its energy use per tonne of steel with 1960 as the base case[3]

1.1. Annealing of steel

Cold rolling is applied in a major part of the produced steel globally and is used to acquire highly accurate dimensions. During cold rolling, plastic deformation takes place, which alters the micro-structure of steel. As it is done below the recrystallization temperature, the grains do not reorganize and therefore lead to altered material characteristics of the cold rolled product. These changes translate to an increase in hardness, but a decrease in ductility.[8]
To make the material more workable and increase its ductility, cold rolled steel is thermally

treated, which is called annealing.
During the annealing process, a steel strip is heated to a temperature of about 700°C and is cooled afterwards. This process can be done in multiple ways; in batch and with a continuous process. Modern steel factories, like Tata Steel in the Netherlands, have a continuous process which is schematically shown in Figure 1.2. An infinitely long steel strip runs through different stages of the process, in which it is heated in a radiant tube furnace and subsequently cooled afterwards. The soaking and overaging stages are meant to keep the strip at a certain temperature for some time. This annealing process consumes about 1.0GJ/tonne of steel[35].
The process is characterized by a heating and cooling part, which are not connected in terms of energy. Essentially, the same amount of heat is put into the steel strip as the amount removed during cooling. Using the heat from the cooling section to heat up the strip upstream the line has significant energy saving potential. Tata Steel Ijmuiden R&D came up with a way of connecting the cooling and heating section in an innovative way, which is able to reduce the energy requirements of the annealing line by up to 70%. This innovative technique uses rotating heat pipes as passive heat exchangers linking cold and hot strip and is called 'heat pipe assisted annealing', patented by Tata Steel[37].

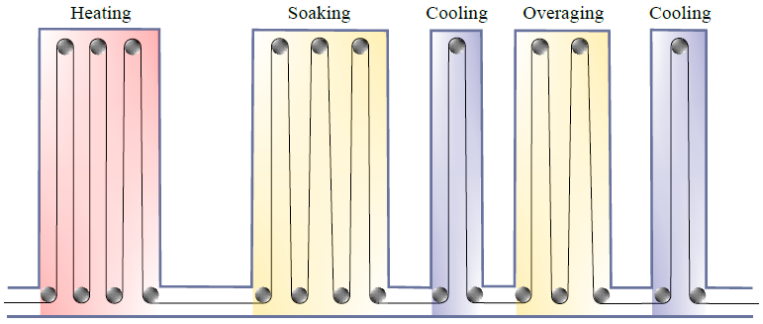

Figure 1.2: Process of annealing today with different stages[11]

1.2. Rotating Heat Pipe

Heat pipes are used as very efficient heat transfer devices. The resistance to heat transfer is relatively low, due to the heat transfer mechanism it uses. Heat pipes contain a working fluid, which vaporizes at one end and condenses at the other, making the fluid a thermal energy carrier. Axial heat transfer goes via vapor convection, which is able to transfer heat over a long distance efficiently. A heat pipe basically is a hollow cylindrical tube with closed ends. It is partially filled with a working fluid after which it is vacuumed. Ideally, the working fluid is the only liquid and vapor present. Multiple types of heat pipes exist, which mainly differ in their way of axial liquid transportation. Vapor flows from heat input to heat output side, while condensed liquid flows back. Heat pipes are orders of magnitude more efficient in transferring heat compared to other passive heat transfer devices, such as conductors.[41]
A rotating heat pipe is a type of heat pipe which rotates along its axial axis. Figure 1.3 shows its working principle, which can be explained in four steps:

- Heat enters the heat pipe radially at the evaporator(red arrows), causing liquid to evaporate and subsequently increasing the pressure at the evaporator side;
- Vapor travels to the condenser side of heat pipe due to the induced pressure difference;
- Condensation of the vapor in the condenser causes the release of heat, which leaves the heat pipe radially(blue arrows);
- Liquid flows back to the evaporator and completes the cycle. The driving force of axial liquid transport is a pressure difference due to a radial height difference of the liquid between condenser and evaporator, caused by centrifugal force or gravitational force.

The rotational type of heat pipe is obvious for the application, as heat needs to be transferred to and from a moving strip of steel. Direct contact between strip and heat pipe is possible due to the heat pipe wall moving with the same speed as the strip, just as conventional guiding rollers as in Figure 1.2.
As the main process of a heat pipe is the vaporization and condensation, the temperature at which this occurs is the saturation temperature of the working fluid. Often, the magnitude of the axial pressure difference is negligible, which causes an equal temperature over the length of the heat pipe. The internal temperature of the heat pipe at steady state is the temperature at which heat in- outflow are equal. The pressure inside the heat pipe is dependent on this temperature, as saturation temperature is dependent on vapor pressure of the working fluid. Liquid at a certain temperature will boil until its environment exceeds the associated vapor pressure. For your imagination, water at 100°C has a vapor pressure of 1 bar. Typical profiles of vapor pressure against temperature will be shown in Figure 1.6.
Besides the low thermal resistance of heat pipe, the controllability is another advantage. Steady-state can be reached at every working temperature. An increase in heat input results in an increase in vaporization rate, which in turn increases the pressure inside the heat pipe due to the net phase change from liquid to vapor. The increased pressure has a new saturation pressure, which has increased. By the risen inner temperature, the condenser heat rejection rate will increase and steady-state is reached. Furthermore, the change to another operating point requires a relatively low amount of energy, due to the relatively low heat capacity of a heat pipe compared to solid conductors. This is beneficial, as it shortens the time to get to a new steady-state point.

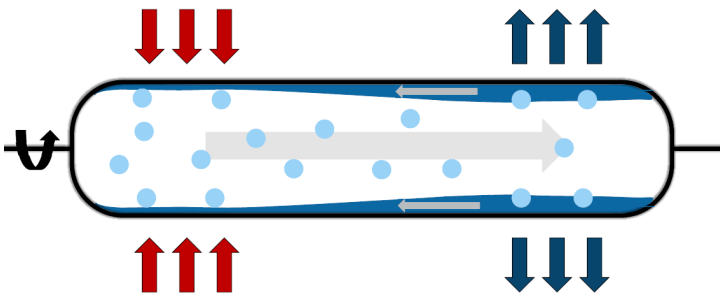

Figure 1.3: Working principle of rotating heat pipe showing heat and mass flows

1.3. Rotating Heat pipe assisted continuous annealing

As the working principle of a single rotating heat pipe has been described, the annealing line, consisting of multiple heat pipes, can be explained now. As discussed, heat pipes can effectively transfer heat from one end of the heat pipe to another end. This could bridge the distance between hot and cold strip and thereby transfer heat between them effectively. An important requirement for the heating and cooling of the steel strip is that it should be done in a homogeneous way. Conduction over the width of the strip is low compared to the power of the heat pipes. Non-homogeneous heating or cooling will therefore result in a temperature gradient over the width of the strip, which in turn causes stresses in the strip due to different expansions over the width, making strip breakage likely. Heat pipes suit the homogeneity requirement very well, due to the absence of an notable axial temperature gradient.
As large amounts of heat need to be exchanged efficiently, many heat pipes are required. Simulation results have shown that the amount of heat pipes required is in the order of 100, which is a trade-off between total heat transfer and investment costs[11]. Figure 1.4 shows the use of heat pipes as heat exchangers between hot and cold strip and shows that each heat pipe has its own unique steady-state temperature. Furthermore, it indicates the time for each part of the annealing process.

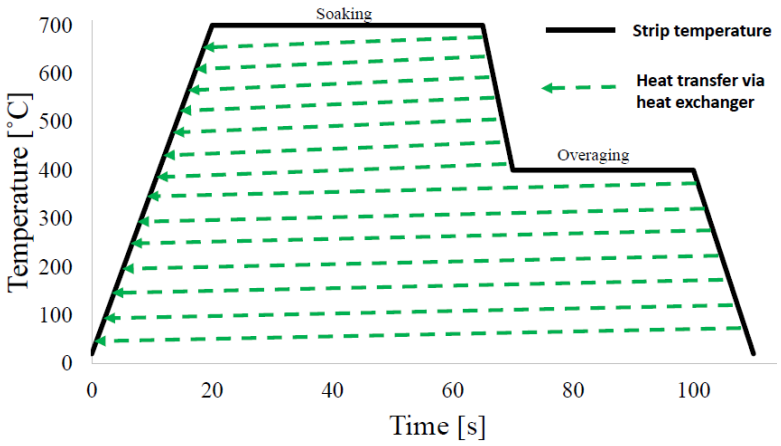

Figure 1.4: Schematic drawing of a heat pipe assisted annealing plant

1.3.1. Plant layout

Figure 1.5 schematically shows the layout of a potential heat pipe assisted annealing line. The hot part rolls over one end of the heat pipe and the cold part over the other end. The strip rolls over a part of each heat pipe, which can be expressed in a wrap angle. After the strip has been heated by all the heat pipes, the final heating to the soaking temperature is done by conventionally heating it. As a temperature gradient is required for heat transfer, final heating will always be required. The amount of conventional heating required depends on system characteristics, such as amount of heat pipes. Typical steel strip speeds are about 5m/s. The heat pipes are positioned in a horizontal way in this system, as illustrated in Figure 1.3.

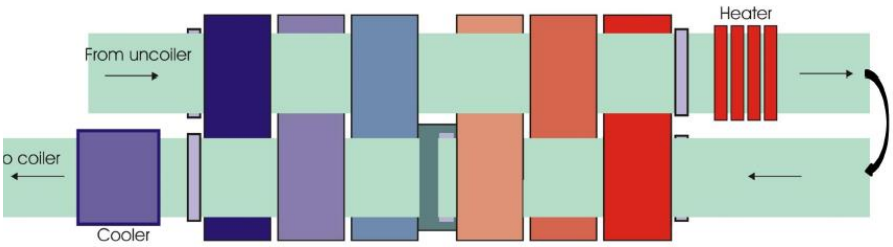

Figure 1.5: Schematic drawing of a heat pipe assisted annealing plant, showing less heat pipes than in the actual design. The strip is heated from top left to top right and cooled afterwards at the bottom of the drawing.

1.3.2. Working fluids

The heat pipe pressure is limited to 5 bar by Tata Steel for practical and safety reasons. Due to this, different working fluids are required to cover the entire temperature range of an annealing line. Figure 1.6 shows the potential working fluids most suitable for this application and their vapor pressure profile. They were chosen according to their material properties, vapor pressures and durability[11, 32]. The performance of a working fluid in a heat pipe is often presented as the following figure of merit[41]:

$$\mathrm{M} = \frac{\rho_l^2 h_{fg} k_l^3}{\mu_l} \tag{1.1}$$

This number summarizes the relevant material properties influencing the performance in a heat pipe. Heat conduction through the liquid, axial liquid transport and vapor transport are covered by this number.

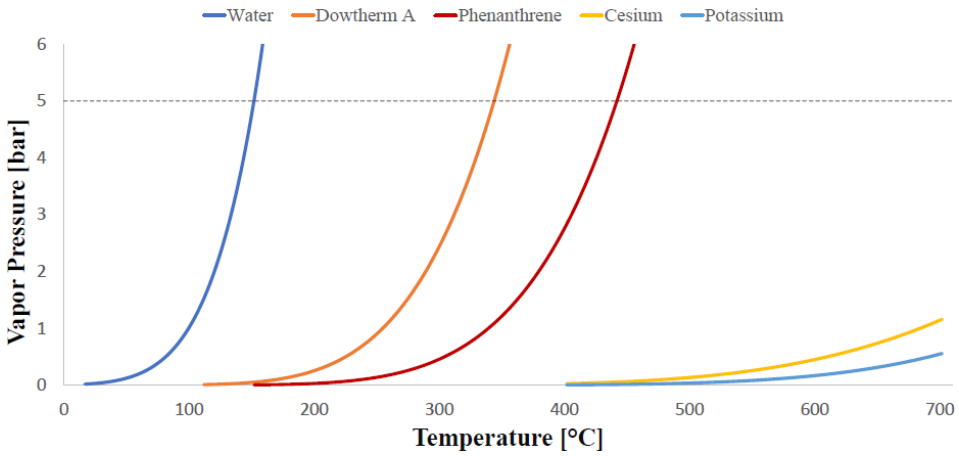

Figure 1.6: Vapor pressure of working fluids of interest[11]

1.3.3. Dowtherm A

The working fluid of focus during this study is Dowtherm A. Dowtherm A is an eutectic mixture of 26.5% diphenyl and 73.5% diphenyl oxide, which makes it an aromatic blend. It is used as fluid in common heat exchangers, but not in rotating heat pipes. Material properties of Dowtherm A can be found in Appendix F. It is surprising that this fluid is chosen as a potential working fluid, as its figure of merit M is rather low. Dowtherm A has a low conductivity k_l and a low latent heat of vaporization h_{fg}, about ten times lower than that of water. This is typical for organics. It is chosen due to the high durability requirement, as it may not degrade thermally or react with heat pipe shell during a long period of operation at high temperature. Durability is not covered by the figure of merit. It was found that Dowtherm A can potentially handle these requirements well. Furthermore, not many alternatives are available with suitable vapor pressures at the required temperature range.[32] This study will not focus on the durability of Dowtherm A, but will focus on heat transfer characteristics of the working fluid. Safety information about Dowtherm is provided by Dow Chemical[15].

1.4. Non-Condensable gas

An ideal heat pipe contains only one fluid, as mentioned in Section 1.2. However, it may occur that another fluid is present inside the heat pipe, due to a leak or improperly filling procedure for example. When this second fluid has a saturation temperature far lower than that of the working fluid, it is called a non-condensable gas, as it does not condense in the heat pipe and stays a vapor. Working fluid continuously follows the cycle of evaporation at one end and condensation at the other end, while a non-condensable gas does not participate in this cycle. It flows along with the bulk working fluid vapor from evaporator and accumulates at the condenser, as it does not condenses as the working fluid does. This resulting accumulation is shown in Figure 1.7. From the left figure, it is clear that there exists a gradient in non-condensable gas concentration. This exists at steady state and can be described by convective and diffusive transport of non-condensable gas. Convective transport is a bulk phenomenon, where it travels with the condensable vapor flow to the right. Diffusive transport is caused by the concentration gradient between the two ends of the heat pipe and brings along a transport to the left. The steady-state distribution is the one at which net transport is zero.[16]
The figure on the right suggests that this causes a temperature gradient in the heat pipe. This can be explained by first noting that the temperature in the heat pipe is equal to T_{sat}, the temperature at which condensation occurs. The temperature profile can subsequently be explained by Raoult's law, which states that the vapor pressure of a component in a mixture is equal to the mole fraction times the vapor pressure as if it was pure:

$$p_{vapor,mix} = x_v \; p_{vapor,pure} \tag{1.2}$$

This suggests a lower vapor pressure due to the presence of non-condensable gas ($x_v < 1$). A reduced vapor pressure also means a lower saturation temperature and thus temperature at which condensation takes place. Condensation occurs at the temperature associated to the partial pressure of condensable vapor, $p_i = x_v p$ according to Dalton's law. As condensation heat is the dominant supply of heat to the condenser, it directly affects the local internal temperature inside the heat pipe.

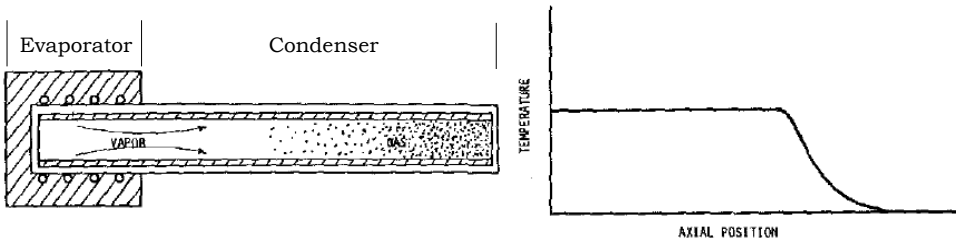

Figure 1.7: Non-condensable gas accumulation in condenser and resulting axial temperature gradient in heat pipe[16], where black dots indicate non-condensable gas molecules

1.5. Previous experimental experience

Numerous other studies were done prior to or during this study. They can be summed up into the following three:

- Working fluid degradation tests in closed small containers[11];
- Experimental campaign with a rotating heat pipe setup with water as its working fluid. Heat was added and removed from the heat pipe by actual steel strips. This study focused on the contact between heat pipe and steel strip, including heat transfer rate[11];
- Designing and building of TU Delft experimental setup, with the purpose to test internal heat transfer characteristics of Dowtherm A and phenanthrene[54];

This study continues on the work of the latter. At the start of this study, the commissioning of the setup started. The size of the setup is shown in Table 1.1, which shows that the TU Delft setup is significantly smaller and that it has a relatively thick wall compared to the full scale as in the application.

Table 1.1: Size difference between TU Delft experimental setup and size as in application. Furthermore, total power and heat fluxes at important heat transfer areas is given. A_i is the cross-sectional area of the inner geometry and A_{wi} is the inner wall area at which vaporization/condensation takes place

	TU Delft setup	**Size as in application**
Outer diameter[m]	0.06	0.60
Length[m]	0.5	3.0
Length evaporator[m]	0.16	1.0
Length condenser[m]	0.19	1.0
Wall thickness [m]	0.008	0.022
Power [W]	500	50000
P/A_i [W/m^2]	329000	206000
P/A_{wi} [W/m^2]	~21000	~29000
Angular part heat pipe in contact with sink/source [^{o}]	360	~110

1.6. Problem Statement

The rotating heat pipe experimental setup of the Process & Energy Laboratory of TU Delft is designed to obtain experimental data of a rotating heat pipe at intermediate temperatures, 150°C - 350°C, and at rotating speeds covering the main flow regimes of the working fluid. The concerning working fluid at this temperature range is Dowtherm A.[11, 32] The focus of this study is on the phenomena inside the heat pipe and how those affect the working of rotating heat pipes as heat transfer devices in a heat pipe assisted annealing line. The following research questions are formulated in order to study the working of a rotating heat pipe with Dowtherm A as its working fluid.

1. What is the effect of rotational speed on heat and mass transfer of the heat pipe?
2. How does the working temperature and thermal power input/output influence the heat and mass transfer inside the heat pipe?
3. Does Dowtherm A perform well as a working fluid of a rotating heat pipe at intermediate temperatures in terms of heat transfer efficiency?
4. How can one model the effect of non-condensable gas inside the heat pipe sufficiently accurate, but with low computational cost?
5. How does non-condensable gas, resulting from leakages, affect the heat and mass transfer in the heat pipe and in what way can non-condensable gas loaded heat pipes still be used in a heat pipe assisted annealing line?

1.7. Methodology

The method followed to answer the research questions of this study comprises of an experimental and a modelling part. First, a literature study is done on the heat and mass transfer phenomena in rotating and non-rotating heat pipes. Afterwards, an experimental plan is made in a way that the obtained data will show to what extent the relevant phenomena found in literature match the experimental data from the TU Delft setup with Dowtherm A. As the heat pipe of this setup turned out to be leaking, the effect of air as a non-condensable gas is included. The experimental work starts with commissioning and is followed by the experiments themselves.
In order to understand the effect of non-condensable gas on the TU Delft setup, a model is devised to both qualitatively and quantitatively study the effect of design parameters and working conditions of the heat pipe. As a first step, a thorough study on existing models is carried out to provide input for the modelling work. The type of model is chosen which is most suitable in answering research questions 4 and 5. After the model itself is finished, validation using comparable studies is done. Furthermore, the model is used to understand own experimental data. As a last step, an analysis of the effect of non-condensable gas in heat pipes on the performance of a rotating heat pipe assisted annealing system is made. The last step is different from the modelling work on obtained experimental data, as multiple process parameters are different at the application in an annealing system compared to at the TU Delft setup, like the sink temperature.

1.8. Thesis outline

Chapter 2 presents a literature research on past studies on heat and mass transfer mechanisms of heat pipes and on the modelling of non-condensable gas in heat pipes. Thereafter, the experimental setup and the experimental method are described in Chapter 3, followed by the experimental results and analysis in Chapter 4. Chapter 5 presents the modelling work of non-condensable gas present inside a heat pipe. The effect of non-condensable gas in a heat pipe assisted annealing system is subsequently presented in Chapter 6. Finally, the report ends with conclusions and recommendations.

2

Literature study

Research on rotating heat pipes performed in the past by other researchers is used to form the basis of this study. This chapter provides a theoretical framework, which is used to formulate hypotheses for the experimental results. This framework is used to interpret experimental results of a rotating heat pipe with Dowtherm A as its working fluid and allows to elaborate on the suitability of a rotating heat pipe filled with Dowtherm A to be used in a heat pipe assisted annealing line. Furthermore, existing models describing the effects of non-condensable gas are presented and their suitability for this study is analysed.

The heat pipe was first introduced by Gaugler in 1944[17]. This heat pipe had a wick, which used the capillary effect to transport liquid back to the evaporator. Notable studies on rotating heat pipes started around 1973, with among others a study of NASA[30] and by Daniels[13] on rotating heat pipes with an internally tapered condenser, which mainly focused on axial liquid transport. Daniels also conducted experiments on the effects of non-condensable gas in a tapered rotating heat pipe some years later[14]. Both theoretical and experimental studies on rotating heat pipes can be found in literature. Various designs of heat pipes have been tested, which mainly differ in their way of transporting liquid back to the evaporator and in the internal wall area. The effect of an internal taper and steps were researched, besides ordinary cylindrical rotating heat pipes. Internal fins and internal helical corrugations in the condenser have shown to have a positive effect on the heat transfer performance[31]. An increased axial transport of liquid by either raised centrifugal force or by for example helical corrugations, resulted in a thinner liquid layer in the condenser, which in turn yielded lower radial heat transfer resistance. An increase in internal wall area in turn resulted in a lower overall resistance as well. Dowtherm A has been used in thermosyphons before[22, 25], but no reports are available of it being used as the working fluid of a rotating heat pipe. The heat pipe of this study is purely cylindrical, so that is where this literature review focuses on.

2.1. Heat and mass transfer phenomena of heat pipes

The heat pipe's individual phenomena can be assessed, assuming the heat pipe is working as designed. The internal surface of the evaporator section should be wet at all angular positions, vapor should be able to flow to the condenser section without a significant pressure drop and the liquid transport back to the evaporator should be high enough, such that liquid is supplied to he evaporator at the vaporization rate. The temperature range at which a heat pipe could theoretically operate is between the triple and critical point, as vapor and liquid coexistence is essential. Also practical limits apply to the operation of a heat pipe, which mainly are the viscous, sonic and entrainment limit for rotating heat pipes, dealing with axial vapor and liquid transport. The viscous limit is reached when viscous forces resist vapor flow to such an extent that the vapor pressure difference does not overcome the viscous forces, resulting in a stagnation of the vapor flow. The sonic limit in turn applies when vapor

speed reaches the speed of sound. Lastly, the entrainment limit applies at high powers and concerns the axial liquid transport. Vapor and liquid flow in opposite directions, which brings along interfacial shear stresses, resisting liquid flow from condenser to evaporator and potentially limiting heat pipe power. The mentioned practical limits are all reached at high vapor speeds, which typically occur at low temperatures, where vapor pressure is low and vapor speed therefore high due to the associated low vapor density.[36, 41]

2.1.1. Flow regimes

A notable part of the heat transfer characteristics is dependent on the liquid inside the heat pipe. The path of heat transfer from inner wall to the vapor space, either by conduction or convection, logically increases with liquid layer thickness and it therefore is of importance to understand the liquid distribution in a cross-section at an axial location of the heat pipe. This section summarizes the relevant information in literature regarding this liquid distribution in rotating heat pipes.

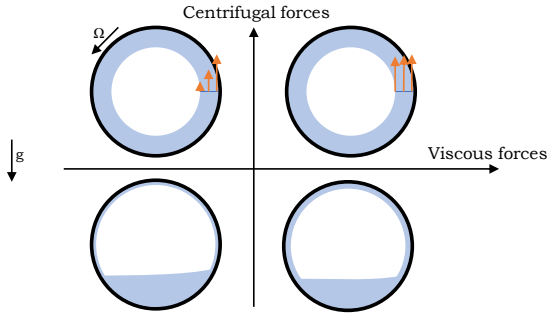

Figure 2.1: Non-annular(bottom) and annular(top) flow regime. The effects of viscous forces are also schematically shown, causing a thicker film in the non-annular flow regime and low radial velocity gradient in the annular flow regime.

Flow characteristics

Two main flow types can be distinguished; non-annular and annular flow, which are visualized in Figure 2.1. Up to a certain rotational speed, a pool exists at the bottom and only a part of the liquid is dragged upwards by the rotating wall, which causes a thin liquid film to be formed on the surface. At higher rotational speeds, all of the liquid is moving with the wall and no pool exists. Numerous studies have been made on the flow regimes in a rotating heat pipe.[11, 27, 47, 54]

Semena et al. described and showed four different regions by experiments and analytical expressions[45]. During Semena's experiments with water and methanol as the working fluid, the liquid layer thickness was measured using electric contact sensors. The four regions can be characterized by the relative size of gravitational, viscous and inertia forces. The gravitational force is dependent on density of the working fluid, viscous force on viscosity and rotational speed, and inertia force on rotational speed, radius and density. At low viscous and inertia forces, only a thin layer of liquid is entrained by the wall. When both gravitational and viscous forces dominate inertial forces, liquid is dragged upwards more easily and viscous effects can be seen in the entire thickness of the liquid film. The upward pulling of liquid by the wall is aided by the viscosity of the working fluid. The entrained thin layer and viscous flow are the two regions within the non-annular flow regime. An increase in rotational speed increases the thickness of the liquid layer outside the pool, as more liquid is dragged upwards. The annular flow regime can be divided in two regions as well. A region of inertia flow, in which the viscous and inertial forces are not large enough to diminish the effects of gravity. This results in a radial velocity gradient in the liquid layer. Solid body rotation is reached when viscous forces are larger or when rotational speed is increased. The different regions are shown in Figure 2.1.

Lin and Faghri looked at the formation of annular flow by visual experiments with a glass heat pipe and noticed that the flow first becomes annular at the ends and subsequently annularity moves towards the middle when rotational speed is increased further[26]. Baker et

al. came to the same conclusion by doing experiments with an acrylic rotating heat pipe[9]. Both studies used water as working fluid. An explanation for this could be that the ends of the heat pipe aid the pulling upwards of liquid, due to which annular flow starts there. Consequently, the neighboring liquid experiences shear forces from the annular flow at one side, which helps it to get to annular flow as well. The start of annular flow at the sides is called the onset of annular flow. Complete annular flow is reached when all the liquid is in annular flow.
Krivosheev et al. found that a hysteresis exists between the start and collapse of annular flow[24]. The start of annular flow occurs at a significantly higher rpm than the collapse, which is caused by the pool. Liquid in the layer returns in the pool after a rotation. Consequently, liquid has to be accelerated from zero to be entrained in the liquid layer again. This requires a high force compared to the situation where annular flow already exists. Annular flow requires less force to maintain its state, as there is no force needed to accelerate the liquid in tangent direction to the heat pipe wall. Semena et al. found that hysteresis is only present when moving from the entrained thin layer non-annular region with low viscous and inertial forces, to the inertia flow annular region[45]. The severity of hysteresis is large when viscous forces are relatively low. A hysteresis is to be expected when the Reynolds number, as defined in Equation 2.1, is larger than 1. In this equation, Ω is the rotational speed, $\overline{\delta}$ the average liquid layer thickness including pool and ν the kinematic viscosity of the working fluid. A high liquid amount or a low kinematic viscosity causes the Reynolds number to be high. Typical values of the Reynolds number in this study lay above 1000, therefore a large hysteresis region is expected, due to the relatively low viscous forces.

$$Re = \frac{\Omega \overline{\delta}^2}{\nu} \tag{2.1}$$

Values for flow regimes

Different studies provided values for the start and collapse of the annular flow regime. Some are purely based on experiments, while other studies have an analytical basis.
Semena et al. gave two relations between the Reynolds number of Equation 2.1 and Froude number, $Fr = \Omega^2 r_{wi}/g$, for the complete and collapse of annular flow based on experimental data in the region 0.05 < Re < 500:[45]

$$Fr_{annular} = 2.2Re^{0.44} \tag{2.2}$$

$$Fr_{collapse} = 2.2Re^{0.13} \tag{2.3}$$

Lin and Groll derived an analytic expression for the collapse of annular flow, by looking at the collapse condition. When the pressure within the liquid layer decreases with radius, the centrifugal force is not large enough to overcome the gravitational force, resulting in an unstable annular flow. This results in the following expression for the collapse of annular flow with low viscous forces, which is only dependent on the filling ratio χ:[28]

$$Fr_{collapse} = \frac{3}{(1-\chi)^2} \tag{2.4}$$

Furthermore, Lin and Faghri described an empirical correlation proposed by Ohtsuka et al. for the onset rotational speed of annular flow and concluded that their experimental observations and results of a glass rotating heat pipe matched the correlation of Ohtsuka[26]:

$$Fr_{onset} = 15.96Ga^{0.107}Ca^{-0.08}\left(\frac{L}{2r_{wi}}\right)^{-0.21}\chi^{0.91} \tag{2.5}$$

In which the Galileo number $Ga = \rho_l^2 g r_{wi}^3/\mu_l^2$, capillary number $Ca = \mu_l^2 g r_{wi}/\sigma^2$, heat pipe slenderness L/r_{wi} and filling ratio χ are factors.
Furthermore, Baker et. al performed optical experiments on rotating heat pipes with different diameter and with different filling ratios[9]. The working fluid he used was water. Baker

provided an empirical relation for the onset, complete and collapse of annular flow. These were all in the form of Equation 2.6. The coefficients for this equation are given in Table 2.1.

$$Fr = C_1(1-\chi)^{C_2} \tag{2.6}$$

Table 2.1: Empirical values of coefficients for Equation 2.6, obtained with a heat pipe with water[9]

	C_1	C_2
Onset of annular flow	9.60	-2.967
Complete annular flow	20.03	-2.421
Collapse of annular flow	3.32	-1.833

Liquid layer characteristics

In order to analyse heat transfer radially through the liquid layer, the thickness of and flow inside the layer should be known, as it determines the heat transfer coefficient. This study focuses mainly on the non-annular flow regime, which has a notable difference in liquid thickness over the range of rotational speeds. The liquid layer thickness in the annular flow regime is equal to the average thickness, $\delta = \overline{\delta}$, as no pool exists and all liquid is in rotation. Filling ratio χ and $\overline{\delta}$ are directly related when liquid is evenly distributed, according to:

$$\chi = \frac{A_l}{A_{cs}} = \frac{\pi\left(r_{wi}^2 - (r_{wi} - \overline{\delta})^2\right)}{\pi r_{wi}^2} \tag{2.7}$$

As mentioned earlier, Semena et al. measured liquid thickness of a rotating heat pipe filled with water and of a heat pipe with methanol. They obtained the following expression for liquid film thickness as a function of rotational speed and liquid properties[45].

$$\delta = 0.02 r_{wi} \frac{Ca^{0.68}}{(\overline{\delta}/r_{wi})^{0.36}}\ exp\left(11.8\frac{\sqrt{\sigma_l/\rho_l g}}{r_{wi}}\right) \tag{2.8}$$

In which Semena et. al use a different expression for the capillary number; $Ca = \Omega r_{wi}\mu/\sigma$. The liquid layer thickness is approximated by this expression with an accuracy of 2.5% in the range $\sqrt{\sigma/\rho g}/r_{wi} = 0.06 - 0.12$, $\overline{\delta}/r_{wi} = 0.002 - 0.05$ and $\delta = 0 - 0.2\overline{\delta}$.
Lin and Faghri obtained an analytic expression for the liquid film thickness in the non-annular flow regime by solving the momentum equation of flow at the point where the liquid is entrained by the wall[26]. They derived the following equation for the film thickness:

$$\delta = \frac{5}{6}\frac{r_{wi}}{\sqrt{g r_{wi}\rho_l/\mu_l\Omega}} \tag{2.9}$$

It is observed by Hashimoto et al. that liquid thickness increases with a large step when annular flow is reached[20]. It increases gradually before the rotational speed of annular flow formation is reached, after which the film suddenly increases thickness with a large step to $\overline{\delta}$, the average liquid layer thickness. This large step is easily visible in experiments measuring liquid layer thickness and the effect of it can be clearly seen when looking at the heat transfer resistance of the condenser.

Furthermore, the flow inside the liquid film is relevant for the heat transfer characteristics. Lin and Faghri showed that the heat transfer of the condenser decreases when rotational speed increases in the non-annular flow regime, which is as expected due to the increasing film thickness. However, the heat transfer coefficient was found to stop decreasing notably

after a certain rotational speed. They predicted the heat transfer coefficient by taking into account turbulence inside the film, which enhances heat transfer and therefore increases the heat transfer coefficient[26].
They determined the heat transfer coefficients through the film for both the laminar and turbulent case. For a laminar film, the heat transfer is by conduction, while a turbulent film enhances heat transfer due to the radial components of mass flow. Natural convection may also be present in the evaporator of the heat pipe. The transition is at the point where the heat transfer coefficients of a laminar and turbulent film are equal. In the case studied by Lin and Faghri, a major part of the non-annular flow regime had a turbulent film.

2.1.2. Condensation

Vapor condenses at the surface of the liquid layer and subsequently travels radially through the layer to the wall. When determining the heat transfer of the condenser, the relevant characteristics are the liquid layer thickness and the type of flow; laminar or turbulent. These two characteristics were discussed in Section 2.1.1.

As the thickness of the liquid film is very small compared to the depth of the pool, it is assumed that all heat is transferred through the film. The surface fraction of the wall covered by the film ξ is used as the effective heat transfer area. First, the angle of the wall covered by the pool θ is determined, which is afterwards used to calculate the effective heat transfer area:

$$\chi = \frac{1}{2\pi}(\theta - \sin\theta) \tag{2.10}$$

$$\xi = 1 - \frac{\theta}{2\pi} \tag{2.11}$$

The heat transfer resistance for a laminar film is rather simple, as no radial transport of heat occurs by convection. Lin and Faghri validated the following expression for heat transfer resistance through a laminar film in a rotating heat pipe with water[26].

$$R_{cond,lam} = \frac{\ln\left(\frac{r_{wi}}{r_{wi}-\delta}\right)}{\xi k_l 2\pi \Delta z} \tag{2.12}$$

They also derived a more complex expression for the heat transfer coefficient for a turbulent film, shown in Equation 2.13. This is an analytical expression for the average heat transfer coefficient at the heat pipe wall with coefficients determined by experimental data of the heat pipe with water. The calculation for film thickness is already included in this expression.

$$h_{cond,turb}\left(\frac{\mu_l^2}{k_l^3 \rho_l(\rho_l - \rho_v)g}\right)^{1/3} = C_1\ Pr^{1/3}\ \xi^{C_2} \tag{2.13}$$

The values found for the constants are $C_1 = 0.1596$ and $C_2 = 0.455$. Their experimental results showed no dependency on rotational speed for the turbulent part of the non-annular flow regime. That is opposite for the laminar layer, in which the heat transfer resistance is increasing with rotational speed. The effect of a thickening of the liquid film is being counteracted by the increase in turbulence. The Froude number was initially also part of Equation 2.13, but disappeared due to the independency on rotational speed. It could be that a rotating heat pipe at other operating conditions or with another working fluid shows different results, but at least the significant effect of turbulence in the liquid film was shown by Lin and Faghri.

2.1.3. Boiling

The heat flowing into the heat pipe is evaporating the working fluid. Standard boiling theory cannot be applied directly to describe the boiling in a rotating heat pipe. Buoyancy force is important when assessing boiling mechanisms. In a rotating heat pipe, this is not only caused by gravity, but centrifugal forces also play a key role. Gravitational force is only aiding the boiling process in the lower part of the heat pipe, which is mainly occupied by the

pool. Without a driving force, heat transport will go purely by conduction through the liquid film. Centrifugal force induces natural convection and also drives vapor bubbles from nucleate boiling to the vapor space of the heat pipe. Centrifugal force therefore determines what vaporization mechanism is dominant. Vaporization happens at the vapor-liquid interface for conduction and natural convection, while it happens at the wall surface for nucleate boiling. Just as with condensation, turbulence also causes heat transport through the film. As the dominant mechanism is unknown, all of them are taken into account.

Song et al. thoroughly researched the evaporation process in rotating heat pipes in a Nusselt type analysis and validated their findings with experiments[48–50]. Bertossi et al. modelled the evaporator heat transfer for low rotational speeds by pure conduction[10] and showed that this could be done when no natural convection is present. Song also noted that heat transfer goes via nucleate boiling when the wall is significantly hotter than the saturation temperature and states that nucleate boiling is suppressed at high centrifugal force, from 20g, due to suppression of vapor bubble formation at the wall surface. Both Song and Bertossi focused on centrifugal forces far above 20g, where nucleate boiling is suppressed. Song et al. showed that mixed convection starts taking place for Rayleigh numbers higher than 400 and showed that liquid layer thermal resistance for dominant natural convection can be determined by a mixed convection model. The Rayleigh number is calculated by:

$$Ra = \frac{\rho_l \Omega^2 r_{wi} \beta \Delta T \delta^3}{\mu_l \alpha_l} \tag{2.14}$$

For Rayleigh numbers higher than 400, the resistance of heat transfer through the liquid layer is given by Equation 2.15.

$$R_{boiling} = \frac{\ln\left(\frac{r_{wi}}{r_{wi}-\delta}\right)}{Nu_m k_l \xi 2\pi \Delta z} \tag{2.15}$$

Where Nu_m is the Nusselt number for mixed convection comprising out of a natural convection (Nu_n) and forced convection (Nu_f) part:

$$Nu_m^{7/2} = Nu_n^{7/2} + Nu_f^{7/2} \tag{2.16}$$

Nu_f is taken as 1, because of the relatively low Reynolds number of the flow in the liquid layer. A Nusselt number of 1 means heat transfer goes purely by conduction. The natural convection part is a function of the Rayleigh number. It is defined as:

$$Nu_n = 0.133 Ra^{0.375} \tag{2.17}$$

Figure 2.2 shows the typical types of boiling, which occur at certain wall surface temperatures T_{wi} above the saturation temperature T_{sat}. It is interesting that maximum heat flux is achieved at a certain wall surface temperature. By further increasing it, the heat flux will be lower. The maximum heat flux q_{max} can be determined by Equations 2.18 and 2.19. The maximum heat flux is proportional to the maximum bubble velocity, v_{max}. q_{max} can be determined by calculating velocity from the buoyancy force and by subsequently using a constant C_{max}, which is in the order of 0.1. Convection and nucleate boiling are mostly of interest for this study, as the high resistance of transition and film boiling makes it unlikely to be the dominant heat transfer mechanism through the film.[33]

$$q_{max} = C_{max} \rho_v v_{max} h_{fg} \tag{2.18}$$

$$1/2 \rho_v v_{max}^2 = \Omega^2 r_{wi} (\rho_l - \rho_v) \delta \tag{2.19}$$

Jouhara et al. performed experiments with a thermosyphon loaded with Dowtherm A at a temperature between 200 and 450°C. They looked at nucleate boiling resistance in a pool[22]. Nucleate boiling typically goes with fewer resistance than natural convection. When nucleate boiling is occurring in heat pipes, the resistance of the evaporator is often considered

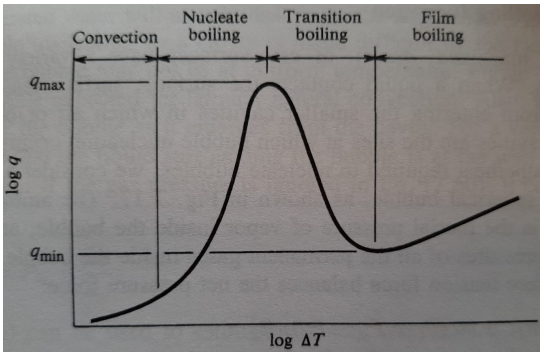

Figure 2.2: Plot of heat flux q against $\Delta T = T_{wi} - T_{sat}$ showing different types of boiling[33]

negligible compared to the condenser[48]. To compare experimental data with theory, an expression for nucleate boiling in a pool is used. Rohsenow correlated the following expression for nucleate boiling Nusselt number on a surface[43]:

$$Nu_{nucl} = \frac{Ja^2}{C_n^3 Pr_l^m} \tag{2.20}$$

Where Jakob number $Ja = c_{p,l}(T_w - T_{sat})/h_{fg}$ and C_n & m are empirical constants. The length scale for nucleate boiling is $L_{nucl} = \left(\sigma/(\rho_l - \rho_v)g\right)^{0.5}$. Jouhara et al. found values for these constants for nucleate boiling of Dowtherm A on a stainless steel surface with a regression analysis; $C_n = 0.00695$, $m = 4.15$. Their experimental data agree with the Rohsenow correlation within 25%.[22] As vapor formation starts in voids on the surface, these constants are dependent on material type and surface roughness. Using this correlation brings along high inaccuracies. Typical errors are 100% of heat flux.[33]

2.2. Modelling of non-condensable gas

Non-condensable gas inside a heat pipe has the tendency to cause a major temperature drop at the condenser end of the heat pipe, as described in Section 1.4. The temperature profile in the condenser can be predicted by determining the non-condensable gas distribution. Numerous results of modelling work have been reported, solving transport diffusion and convection equations for non-condensable gas and condensable vapor[13, 16, 19, 52]. Research on the modelling of non-condensable gas has only been done on stationary heat pipes. Due to the unavailability of work on rotating heat pipes with non-condensable gas, this section focuses on the literature on the modelling of stationary heat pipes. In essence, the basis of the to be solved problem is equal for stationary and rotating devices, provided that the effects of rotational speed on the vapor flow are limited.

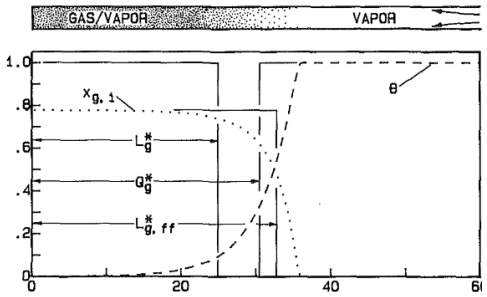

Figure 2.3: Graph showing non-condensable gas distribution and associated dimensionless temperature($T_{ev} = 1$) by Peterson et al. Different shut off lengths are shown: L_g^* the non-condensable gas inventory, Q_g^* the effective blocked condenser length in terms of heat transfer, $L_{g,ff}^*$ the length of non-condensable gas if it was a flat front[39]

Early research on the modelling of non-condensable gas dates back to 1970[29]. It started

very simple with a modelling study by Bienert et al., who modelled the front between working fluid and non-condensable gas as a sharp interface without a region of coexistence. This was under the assumption that all non-condensable gas is accumulated in a volume without any condensable vapor, resulting in a low blocked length, as shown by parameter L_g^* in Figure 2.3. Experimental observations on a heat pipe with water and air as its non-condensable gas by Edwards and Marcus showed that a region of coexistence is clearly present[16]. They developed a 1D model in which the distribution was modelled as a convection-diffusion problem, which resulted in a region of coexistence and in fairly good agreement with experimental data. This allowed to determine the effective length of the region shut down to heat transfer Q_g^*, which is a measure of power decrease of the condenser. Furthermore, they included the axial wall conductance and showed that it is of principal importance in modelling the shape of the front. An energy balance on a wall element was used to determine local condensation rate, taking into account wall conduction. This model was kept in 1D by assuming a similar wall temperature profile compared to inner temperature. Daniels and Shukla continued this work and improved it by calculating wall temperature separately[12, 46].

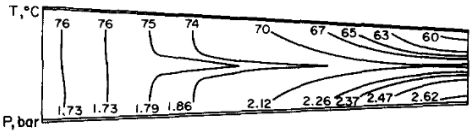

Figure 2.4: Temperature measurements by Daniels et al. inside a tapered rotating heat pipe, with arcton as working fluid and nitrogen as non-condensable gas. The contours of constant temperature are shown[14]

Daniels was one of the first measuring radial temperature profile as well, as shown in Figure 2.4[14]. This suggested that a 2D-distribution is present, where the non-condensable gas at the wall is covering a larger part of the heat pipe than in the middle. Hijikata et al. and Harley et al. succeeded in modelling this phenomenon by also modelling radial transport[19, 21]. Peterson et al. carried out a parametric study on heat pipe characteristics and operating conditions affecting the severity of 2D non-condensable gas distribution[39]. More recent studies mainly researched the transient behavior of heat pipe with non-condensable gas. Saad et al. concluded that the transient response during heating up is not affected by the presence of non-condensable gas, but the cooling down is significantly slowed down.[44].

2.3. Conclusion

From this chapter it became clear that rotational speed and filling amount are of large influence on the heat transfer characteristics of a rotating heat pipe. The liquid layer thickness is a determining factor for heat transfer resistance. We have seen that non-annular and annular flow regimes exist. An increase in rotational speed, causes the liquid layer to become thicker, which resists radial heat transfer. Expressions for transition rotational speeds to the annular flow regime from literature were given. Furthermore, relations for liquid film thickness are found in literature and the effect of turbulence in the liquid layer has been shown to decrease heat transfer resistance. Heat transfer mechanisms through the film in the condenser are conduction and turbulent mixing, while in the evaporator also natural convection and nucleate boiling may be the dominant heat transfer mechanism.
Models exists for heat pipes loaded with non-condensable gas. They almost all describe the non-condensable gas distribution by convection-diffusion transport equations. The resulting distribution succeeds in predicting the influence of non-condensable gas on heat pipe performance. The severity of 2D-effects inside the heat pipe has been quantified in literature.

No research is available on rotating heat pipes with Dowtherm A. This chapter provides a theoretical framework, which can be used to check whether Dowtherm A behaves as expected in the experimental setup used in this study and which heat transfer mechanisms are likely to play a role.

3

Experimental Setup & Method

The TU Delft Rotating Heat Pipe setup is designed to obtain experimental data with which internal heat and mass transfer of a rotating heat pipe with Dowtherm A can be characterized. It is designed to determine temperature and heat transfer rates radially through the wall and to determine the axial temperature profile inside the heat pipe. This experimental setup design differs from heat pipes in practical applications. The thickness of the wall is usually minimized to decrease heat transfer resistance. For this setup, a thick wall is chosen, as this allows more accurate measurements of radial heat flux through the wall. The setup allows experiments to be done at a temperature and pressure range which is equal to that at the application of a heat pipe with Dowtherm A in a heat pipe assisted annealing line. Furthermore, the combination of range of rotational speed and filling ratio should allow experiments within both the non-annular and annular flow regime.
The experimental work of this thesis continues on former work on this experimental setup[54]. The design of the setup, manufacturing and assembly were finished at the start of this study.[32, 54] The first phase of this experimental work was the commissioning of the setup. The commissioning showed the capabilities and deficiencies of the setup. It showed that an eccentricity of the heat pipe caused problems with the rotation and that the heat pipe could not be sealed fully hermetically.
This Chapter describes the rotating heat pipe experimental setup at the Process & Energy laboratory of TU Delft. First, the setup itself is discussed, including the deficiencies, control and safety measures. This is followed by the experimental method used in this study.

3.1. Component description

The entire setup, which is in a cabinet for safety reasons, can be seen in Figure 3.1. The TU Delft experimental setup consists of the following components, which will be discussed one by one:

- Rotating heat pipe;
- Rotational motor;
- Slip ring;
- Oven;
- Condenser cooling duct;
- Bearings;
- Cooling outside wiring tube.

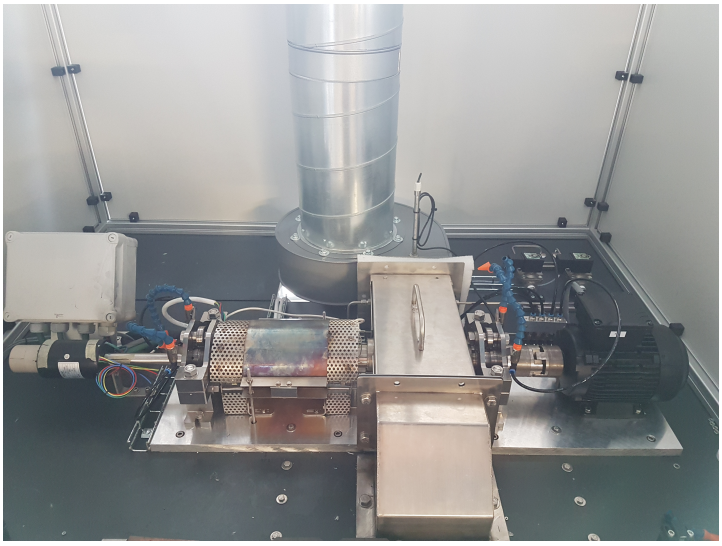

Figure 3.1: Experimental setup with from left to right surrounding the heat pipe: slip ring, bearing block, oven, condenser cooling duct, bearing block, motor coupling and rotational motor

3.1.1. Heat Pipe

The main part of the heat pipe itself is a cylindrical tube of AISI 316 stainless steel of 8mm thickness with closed ends. The most important part for this study is the cylindrically shaped chamber inside. Inside the hollow space of the heat pipe, a thin tube in axial direction at radius zero serves as thermocouple mounting and as a cover for the wiring of sensors inside the heat pipe and in the wall towards the slip ring. Figure 3.2 shows multiple drawings with the relevant components and dimensions of the heat pipe. The inner wiring tube is illustrated as well. The different components are fixed to the main cylindrical tube by means of a weld or a press fit. The only entrance to the inner space of the heat pipe is via the hole closed by the filling plug. The left end of the heat pipe accommodates wiring towards the slip ring. The right part serves as a coupling to the rotational motor and it is the place where the heat pipe can be filled, emptied and vacuumed. The heat pipe's rotation is supported by bearing blocks at the sides. Each of these bearing blocks consists out of three ball bearings rolling against the heat pipe at three different angular positions. The bearing blocks allow the radial thermal expansion of the heat pipe by the use of spring washers between the upper and lower parts of the block. The functional part of the heat pipe is located between the two bearing blocks. The length and location of the sections of the heat pipe inside the oven and cooling duct part will be shown in Figure 3.8.

Inner space heat pipe

Figure 3.2b and 3.2c clearly show the inner space of the rotating heat pipe, to be partly filled with the working fluid. The geometry of this inner space basically is a hermetically closed cylinder with a diameter of 44mm with another tube in the middle. This wiring tube covers about 4% of the cross-sectional area of the inner space. From this 9mm diameter wiring tube, small tubes run radially towards the wall which connect the wall sensors. Besides the wiring itself, the wiring tubes are entirely filled with solder and therefore are not part of the volume which can be taken up by the vapor or liquid. Furthermore, five thermocouple tips stick out a few millimeters from the center wiring tube at different axial locations. More detailed drawings, used for the setup construction, are attached in Appendix A.

Filling & Sealing

The process of getting a certain amount of working fluid inside the heat pipe and closing it hermetically while the inside is under vacuum turned out to be difficult with the tools available. Valves for vacuuming the heat pipe were not easily available, as they are required to be small and able to handle the high working temperatures. In the absence of a valve, the heat

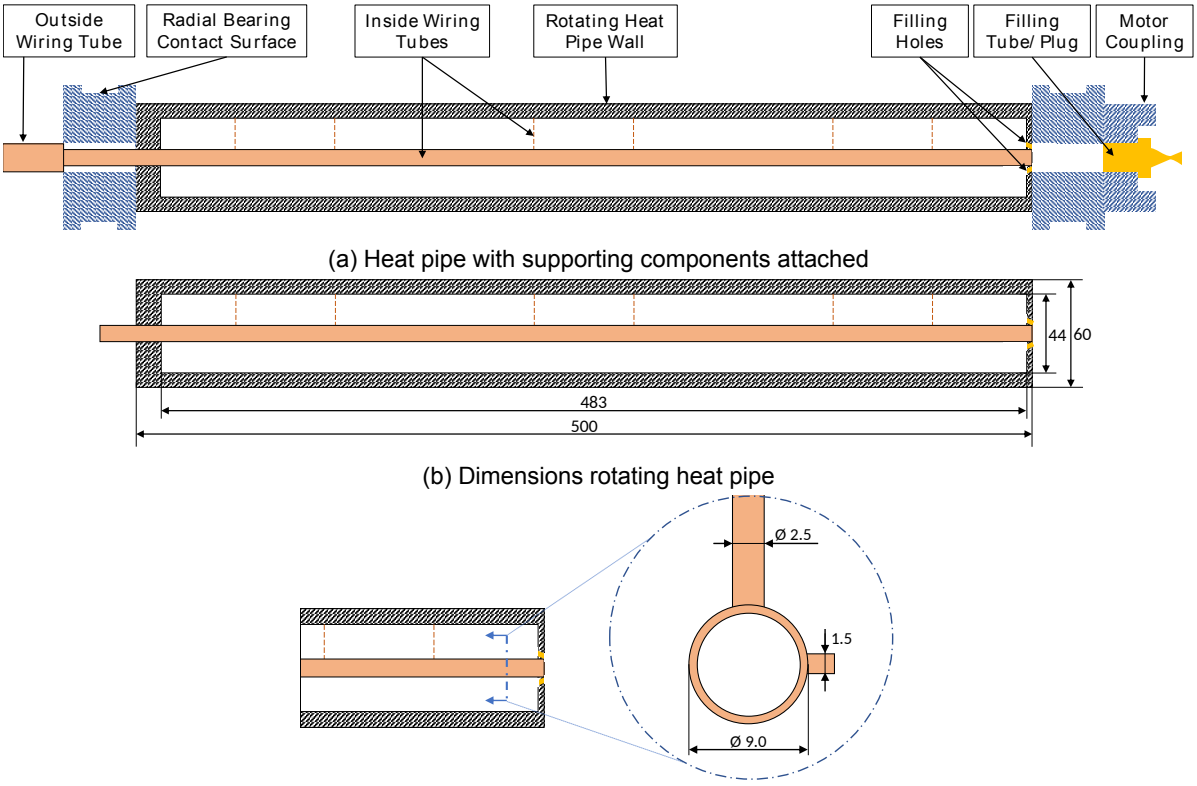

Figure 3.2: Scaled drawings of a cross section of the heat pipe. Dimensions in [mm]

pipe has to be vacuumed while being closed. Therefore, the following method is applied. Pictures of the closing are shown in Figure 3.3. A filling tube with a copper washer is screwed into the heat pipe end at the side of the motor coupling, as illustrated by Figure 3.2a. This filling tube basically is a bolt with a hole drilled through the center. A tube is fixed in this hole by a weld, forming a leak-tight connection. After the heat pipe is filled through the filling tube, the heat pipe is attached to a work bench and vacuumed by a vacuum pump attached to the filling tube. The filling tube is closed by squeezing it from two sides by a modified vise. Before squeezing, the filling tube is heated locally with a gas burner to increase its ductility and therefore prevent breaking it during deforming and it is heated to be able to fully squeeze it. The vise is modified such that its contact surfaces have a reduced area and exert most squeezing force on a contact line perpendicular to the axial length of the filling tube, sealing it along this line. The heating and squeezing is repeated several times, while the heat pipe is continuously vacuumed. Afterwards, the heat pipe is considered to be almost fully closed, but very small leak paths may be present. To fully close the heat pipe while still being squeezed, the filling tube is sawed off just beyond the squeezed part and welded inside directly afterwards. The result is shown in the right picture of Figure 3.3.
This method originates from an old patent[18] and has been used in another heat pipe study[53]. Within this project, it has been further developed for this application by collaboration with the workshop personnel of the laboratory. The filling tube diameter, wall thickness and material were of influence on the sealing performance.
This process is considered far from ideal, as it is labour intensive, requires a new filling tube every time and it turned out that this method does not guarantee a hermetically closed heat pipe consistently. It is however used as no better alternative is readily available.

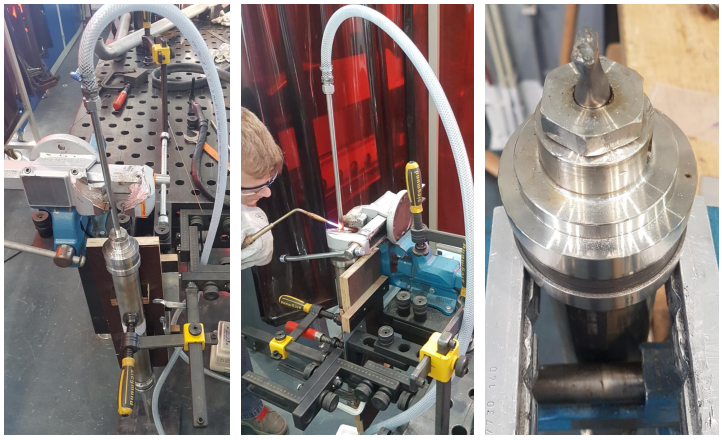

Figure 3.3: Vacuuming(left), heating and closing using modified vise(middle) and result after welding(right)

3.1.2. Slip ring

The wires from the heat pipe are of course rotating with the same angular velocity as the heat pipe. To connect the wiring to the stationary control unit, a device is needed to connect the rotating wires with stationary wires. The setup has a slip ring to realise this. It is attached to the outside wiring tube, as can be seen in Figure 3.1 and 3.4.
The slip ring used is type SRH2578-12P/24S from brand Penlink[5]. The electrical resistance of the slip ring is 100mΩ. The resulting error of this resistance is negligible, as the impedance of the thermocouple input unit is much higher[54].

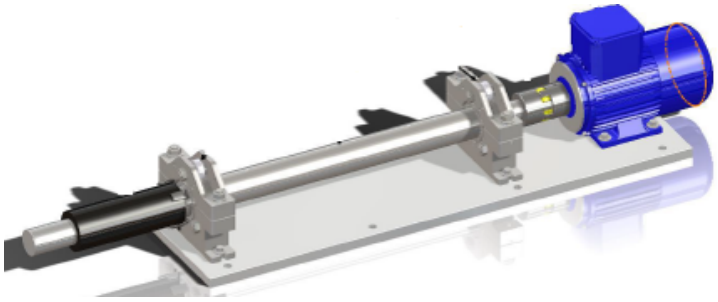

Figure 3.4: Drawing of heat pipe, slip ring(black), rotational motor(blue) and ceramic coupling(yellow)[54]

3.1.3. Rotational motor

The frequency range of the rotational motor is between 50 and 1090rpm. It can be controlled with an accuracy of 25rpm.
The motor is attached to the heat pipe by the motor coupling. A ceramic coupling is used, which is able to withstand high temperatures. This coupling allows the axial expansion of the heat pipe. The positioning of the motor relative to the heat pipe setup was determined by an estimation of the maximum thermal expansion of the heat pipe. For this estimation, linear thermal expansion of a SS316 tube is considered, as shown by Equation 3.1. For a conservative calculation, the heat pipe is considered to entirely heat up 50°C beyond the maximum working temperature causing a temperature difference of 380°C, which could actually only occur if the oven covers the entire heat pipe. The length is taken as the distance between the left bearing block in Figure 3.4 and the motor coupling, as the expansion in this area should be allowed by the motor coupling. The expansion according to this formula is 0.004m, which is a conservative estimation of the actual to be expected expansion.[2]

$$\Delta L = \breve{\alpha}_{SS316}(T_{max} - T_{min})L \tag{3.1}$$

3.1.4. Oven

Six quartz lamps provide radiant heating to the evaporator section with a maximum power of about 500W. The lamps are cylindrically shaped and are positioned at six angular positions around the heat pipe. They have an effective heating length of 165mm and can reach a temperature of 900°C. One of the lamps can be seen in Figure 3.5b. The central part of the oven is surrounded by polished steel to reflect radiation not yet absorbed by the heat pipe. The oven consists of an upper and lower section, which allows the removal of the heat pipe from the setup. The gap between these two sections is kept limited to restrict the loss of radiation from this central chamber. The same applies to the gap between heat pipe and oven wall at the left and right end of the central chamber. This is done to restrict the heat input to the section of the heat pipe in the central oven chamber. However, some of the radiation escapes the chamber. The heat pipe parts running through the two outer chambers are also likely to absorb some radiation of the lamps, as the lamps are slightly longer than the central oven chamber. The oven in operation can be seen in Figure 3.5a. It is clear that light escapes the oven.
To increase the amount of heat absorbed by the heat pipe, a black coating has been applied on the heat pipe part within the central oven chamber. This coating can be seen in Figure 3.5b.

(a) Rotating Heat Pipe in operation

(b) Coating and adiabatic section insulation

Figure 3.5: Setup in operation and a picture of oven chamber and adiabatic section

3.1.5. Cooling duct

A centrifugal pump blows air from outside the cabinet through the cooling duct, resulting in a flow perpendicular to the heat pipe. The closed condenser air duct is located at the right side in Figure 3.5a, with the intake from above and pump housing in the upper half of the picture. Figure 3.6 shows an image of the inside of the condenser, which basically is a rectangular duct. The dimensions of the cooling duct are given by Figure 3.7. The maximum air velocity of this system is well beyond the cooling requirement. Again, it is desired to concentrate the cooling on the section of the heat pipe within the cooling duct. For this reason, the gap at both sides of this section is minimized. The existing gap between heat pipe and duct is filled up with glass fibre wool. This is not a perfect seal, so some of the air escapes in the axial direction of the heat pipe.

3.1.6. Insulation and Cooling

The adiabatic section is insulated to minimize heat loss in this section of the heat pipe, as shown in Figure 3.5b. The insulation material used is thick nonadhesive glass fibre tape. It is fixed to the condenser air duct and is therefore not rotating with the heat pipe, which

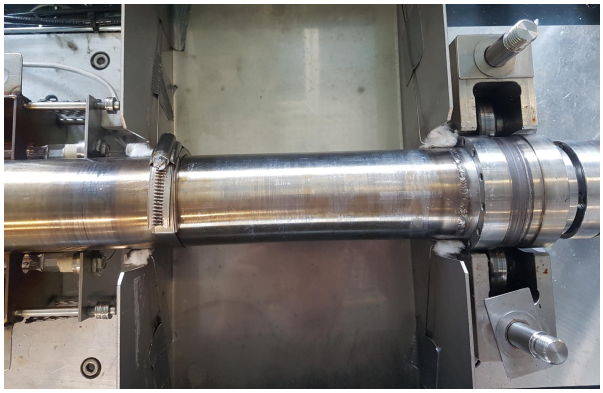

Figure 3.6: Inside the condenser air duct, also showing the location of the balancing weight on the left

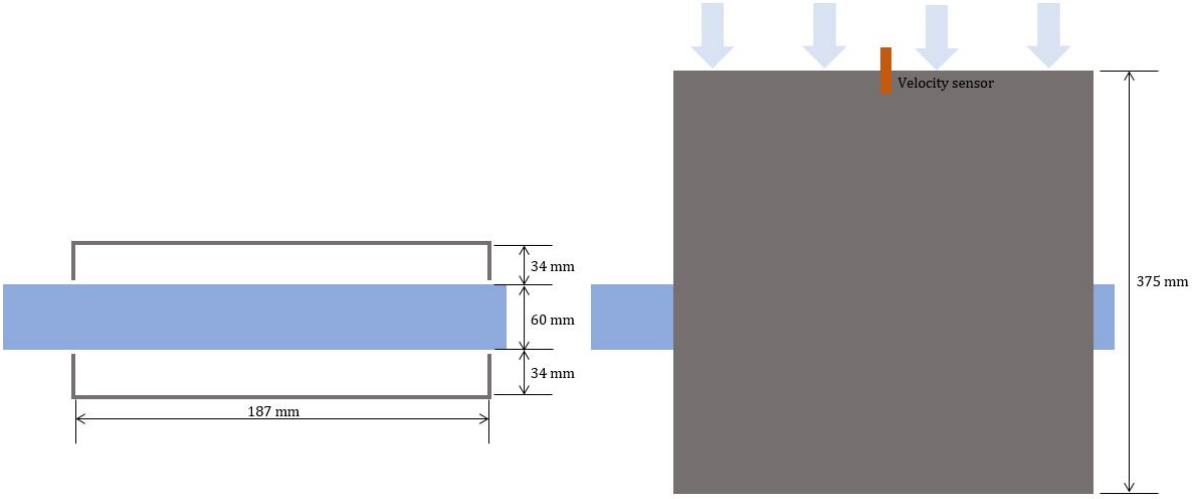

Figure 3.7: Side and top view of condenser cooling duct(grey) and heat pipe(blue)

causes a small gap between insulation and heat pipe. As mentioned earlier, some air from the condenser escapes the duct and blows along the heat pipe. This causes some cooling in the adiabatic section, which is small compared to the cooling in the condenser duct itself. However, this causes the heat loss of the adiabatic section to be depending on the air flow in the condenser.

Cooling of the outside wiring tube is required, as it is filled with resin. This resin is not able to handle the upper working temperatures. A thermocouple is mounted at the outside wiring tube end in the bearing block. This allows the monitoring of the temperature. To maintain the leak tightness, this temperature is kept below 130°C. Air cooling on the bearing block and wiring tube itself is applied to achieve this. The four blue tubes with orange nozzles in Figure 3.5a connected to a pressurized air source realise the cooling. The wiring cooling power is manually adjusted.

3.2. Sensors

The heat pipe is equipped with multiple sensors measuring temperature, heat flux and pressure. Four thermocouples are mounted to the inner wiring tube, measuring the inside temperature. At six locations in the wall, both the radial heat flux and temperature are measured. Furthermore, the pressure inside the heat pipe is measured at the oven end of the heat pipe. The axial locations of these sensors are visualized in Figure 3.8 and are given in Table 3.1. The wiring temperature sensor in the outside wiring tube and the cooling air velocity and temperature sensor are not shown in the Figure.

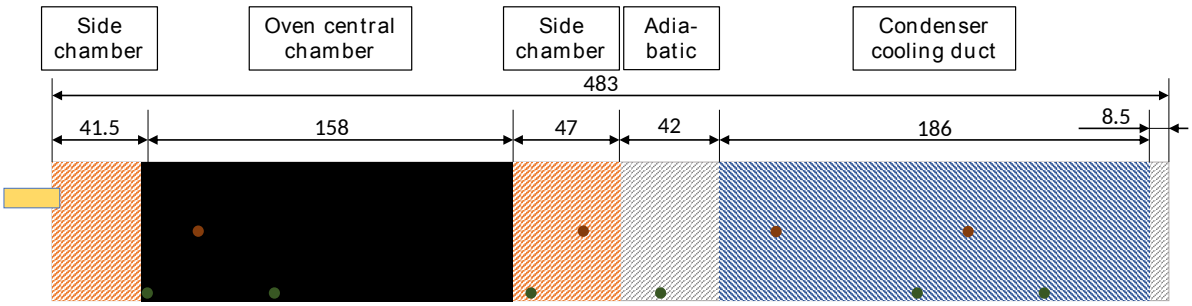

Figure 3.8: Hollow part of the heat pipe with the length of given sections in mm (+- 1mm) and the black coating. Axial location of sensors: Inside thermocouples(brown), wall sensors(green) and pressure sensor(yellow).

Table 3.1: Locations of inside and wall sensors

Type	**Axial location** [mm] from left end vapor space
Thermocouples inside	TC1: 60 TC2: 226.5 TC3: 310 TC4: 393
Heat flux sensors and thermocouple in wall	HF1: 38 HF2: 93 HF3: 204 HF4: 260 HF5: 371 HF6: 426

The wall sensors measure both temperature and the radial heat flux. Actually, the radial heat flux is determined from temperature measurements at different radial positions using Fourier's law. The temperature gradient is determined from the ΔT shown in Figure 3.9. The thermocouples are placed at 2mm and 6mm from the inside wall surface. Four thermocouples are linked in series in such a way that ΔT is measured twice, which after division by 2 gives a more accurate measurement[54]. A most inner thermocouple in the wall is used to measure the wall temperature. The sensors are placed inside the wall in such a way that the effect on the heat flux is minimal.

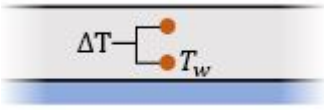

Figure 3.9: Radial location of wall temperature sensors. The blue layer indicates the liquid layer inside the heat pipe.

The characteristics of the three different type of sensors used are shown in Table 3.2. The accuracy either comes from manufacturer specifications, calibration technique or from interpretation of experimental data. Heat flux sensor calibration could only be done to 15% accuracy by the manufacturer of the heat pipe. The temperature sensors were calibrated accurately and the typical accuracy of K-type thermocouples applies. Although the pressure sensor manufacturer specifies its accuracy to be 0.2 bar, the readings from the setup suggest a lower accuracy. It jumps up and down continuously. The average of many readings can only serve as an indication of the pressure inside the heat pipe. This also happens when the

heat pipe is not rotating, so it is not likely to be due to the slip ring error. According to the manufacturer, the pressure sensor can handle temperatures up to 100°C. It could be that the pressure sensor has been damaged during testing, as temperatures far beyond the upper limit were reached.

At ambient conditions, the heat flux sensors were all measuring a radial heat inflow at the commissioning phase. As there is no driving force for a heat flow, this must be an error. The manufacturer, experts on temperature and heat flow measurement solutions, states that this error very likely is an absolute offset. Therefore, an absolute offset correction is made to the individual heat flux sensors. To be more sure about this offset, a test was carried out. During this test, the heat pipe was brought to a homogeneous temperature other than the ambient temperature, followed by it decrease to the ambient temperature while reading out the sensors. As the outside wiring tube cannot withstand high temperatures, it was decided to cool the heat pipe in a climate chamber for this test and let it warm up again due to the higher ambient temperature. The profile of the heat fluxes during the warming up, which should be about homogeneously, could give information about the heat flux sensor offset. The process and the results are described in Appendix B.
The conclusion is that no sign of a relative offset could be seen. There was no correlation seen between the offset and the heat flux difference between cold and ambient condition of the heat pipe. Furthermore, the offset corrections themselves are of the same magnitude as or smaller than the accuracy of the heat flux sensors. A doubling of the offset at a point during the experiments will therefore still fall within the accuracy margin of the heat flux sensor. No hard conclusion could be drawn, as the heat pipe did not warm up in a fully homogeneous way. The absence of an observable relative offset does however rule out a large relative error. The offset likely is an absolute offset according to the manufacturer, but even if the offset is relative, the associated error of using an absolute offset correction will fall within the accuracy at all working working temperatures. A thorough description of the test including recommendations is given in Appendix B.

Table 3.2: Characteristics Sensors

Sensor	Type	Accuracy
Temperature	K-type thermocouples	± 2.2°C or 0.75% (whichever is greater)
Heat flux	Thermocouple configuration	± 15%
Pressure	Endress PMC131-A11F1A1V	± 0.4 bar
Air velocity	DeltaOHM HD29V37TC2.2	± 0.5m/s+3%

3.3. Setup deficiencies

Unfortunately, this experimental setup has flaws which may effect the working of the heat pipe. Beside the inaccuracy of the pressure sensor, other flaws have come to light during commissioning. One of the flaws is an eccentricity in axial direction of the heat pipe. The other flaw of this setup is the disability to hermetically close the heat pipe. The eccentricity is likely to affect liquid distribution and flow inside the heat pipe, while a leak causes non-condensable gasses to enter the heat pipe, which in turn influence heat transfer characteristics in the vapor space of the heat pipe. The details of these flaws will be discussed in this section. The perceived effects will be discussed in Chapter 4.

The eccentricity formed during the construction of the heat pipe. A schematic of the eccentricity is shown in Figure 3.10, in which the defect is drawn in an enlarged way. The wall sensors are at the opposite side from the maximum eccentricity, as shown in the Figure.

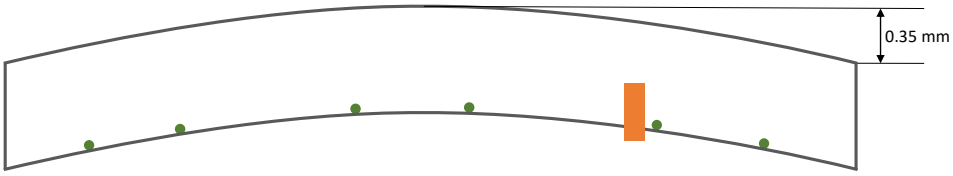

Figure 3.10: Schematic drawing of the direction of eccentricity with the wall sensors(green) and balancing weight(orange)

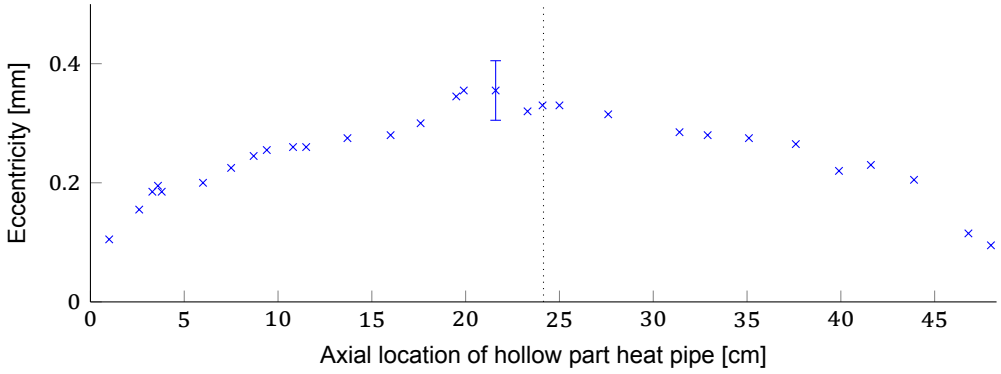

Figure 3.11: Eccentricity with marked middle of hollow space(dotted)

It is therefore likely that the eccentricity formed during the placement of the wall sensors. The eccentricity has been measured with a lever dial indicator. A change in height of the heat pipe during a full rotation indicates eccentricity, as the surface itself is smooth. The maximum change in height at an axial location divided by 2 gives the eccentricity as defined in the schematic drawing. The results of the measurements are given in Figure 3.11, which shows a parabolic profile of the eccentricity. The maximum looks like to be at the oven side of the middle, but cannot be told with certainty due to the measurement error. The eccentricity also brings along a rotational unbalance, which restricted high rotational speeds to be reached. Balancing has resolved this problem, as described in Appendix C.

The disability to close the heat pipe hermetically is another shortcoming of the setup. In ideal working conditions for heat pipe assisted annealing, only the working fluid is present inside the heat pipe. A leak causes air to leak into the heat pipe at low pressure and possibly causes working fluid vapors and air to escape at high pressure.

At ambient temperature, the pressure measurement serves as an indicator for the amount of air inside the heat pipe, as the vapor pressure of Dowtherm A at room temperature is 0.00002 bar. A higher pressure at room temperature indicates the presence of air and the magnitude is a measure for the amount of air, according to the following formula:

$$m_{air} = V\rho_{air} \tag{3.2}$$

,where V is the volume of the vapor space, which is the inside volume excluding the volume taken up by liquid. The inner wiring tube is not part of the vapor space, as it is filled with solder. ρ_{air} changes with the pressure inside the heat pipe. Although the pressure measurement is very noisy, it clearly shows an increase over time with many data points.

The leakage rate can be seen from the pressure measurements in Figure 3.12. Although the measurement error is high, a clear trend could be seen. The leakage rate differed between each closing. It is also clear that the leakage rate increased at the end of closing #1, probably due to vibrations and/or high temperatures. The increase occurred after a run with high RPM's. The leak after closing #1 was small compared to the other closings, which were similar or worse than closing #3. Unfortunately, a major part of closing #1 was taken up by the commissioning of the setup. The leakage limits the amount of time available for experiments after each closing significantly, as after a certain amount of air inside has leaked in, normal operation of the heat pipe is severely obstructed.

The location of the leak was tested and it turned out to be at the filling tube. The pressure

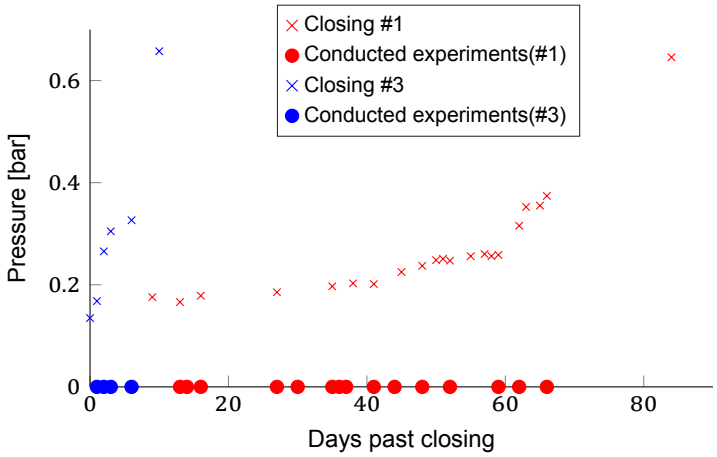

Figure 3.12: Pressure measurements at ambient temperature showing leak rate. Please note the accuracy of +-0.4bar. The conducted experiments are marked on the horizontal axis.

was measured before the filling tube was squeezed, while the heat pipe was still connected to the vacuum pump with a closed valve in between. The valve of the vacuum pump was acting as the seal in this case. No pressure increase was seen during multiple days. This was followed by closing #2 with the same filling tube, which showed a major leak. As the leak was absent with the vacuum tube attached, one can conclude that the closing process causes the leak, which tells that the leak is located at the filling tube. This is at the condenser end of the heat pipe.

3.4. Experimental method

This section describes the experimental method followed to answer the research questions of this study. The scope of this study changed after commissioning, due to the identified deficiencies of the setup. The effects of non-condensable gas were added and the influence of the eccentricity on liquid distribution and flow had to be considered during result analysis to check whether the results are representative for a rotating heat pipe without eccentricity as well. Furthermore, the amount of experiments was limited, due to the leak and labor intensity of the closing procedure. This section describes the filling amounts, the procedure followed during experiments and the conducted experiments.

3.4.1. Filling procedure and filling amount

Experiments were done with two different amounts of Dowtherm A in the heat pipe. The filling of the first round of experiments was relatively simple, as the heat pipe was delivered empty. The desired mass of Dowtherm A was added through the filling tube. The second round of experiments required a more extensive filling procedure, as the used working fluid was still inside. To get to an accurate amount of pure Dowtherm A inside, the heat pipe was first emptied. Adding or removing a part of the working fluid would bring along inaccuracies, as the used Dowtherm A could have degraded and errors on the filling amount could build up. Therefore, it was chosen to first fully empty the heat pipe before filling it again.
Sharp corners near the filling tube inside the heat pipe complicated the emptying. The liquid flowed through the small filling holes and subsequently through the hole of the removed filling tube. By pointing this side of the heat pipe downwards, most of the Dowtherm A flowed out, but a part of it remained inside. Rinsing has been used to get the remaining part out. A suitable liquid had been found, in which Dowtherm A dissolves and which evaporates relatively quickly at ambient conditions. This was required to not end up with a bit of another liquid inside, which would not evaporate out of the heat pipe. The used liquid for rinsing was acetone. The rinsing was done multiple times, until a negligible content of Dowtherm A was found in the rinsing liquid. The amount of Dowtherm A coming out was subsequently determined by letting the acetone evaporate out of the rinsing liquid, leaving the Dowtherm A.

Figure 3.13: Eccentricity with axis of rotation(dashed) and filling compensation for eccentricity(blue). The eccentricity has been drawn in an enlarged way.

The evaporation of Dowtherm A at ambient conditions is negligible. After emptying the heat pipe loaded with 95g of Dowtherm A, 93g of the working fluid was obtained, which confirms that the leak of Dowtherm A was not major. Before filling, the heat pipe was vacuumed for multiple hours to make sure that no more acetone was inside.

The amount of working fluid was determined in such a way that all the flow regimes could be reached within the accessible rotational speeds. The literature study described in section 2.1.1 has been used to calculate suitable filling amounts.
Some extra liquid was added to compensate for the eccentricity of the heat pipe. The centrifugal force from the rotation pulls the liquid to places with highest distance from the axis of rotation. This distance differed in axial and angular direction due to the eccentricity. The compensation amount was chosen such that it fills the volume with higher distance from the axis of rotation than the inner radius of the heat pipe. This volume is illustrated in Figure 3.13, where a-cross section of this volume is shown for an angular position. At high rotational speeds, liquid will be present at the sides only when the heat pipe is filled with more liquid than the compensation amount. As increments in filling amount will cause extra liquid to be present at the sides, this method is chosen to compensate for the eccentricity. It should be noted that the above applies to high rotational speeds, where enough liquid is pulled upwards with the wall such that it fills the concerning volume while rotating. At lower rotational speeds, this volume is not constantly fully occupied by liquid due to the lower centrifugal force with respect to gravity. The extra liquid will then be part of the pool, which means it can no longer be fully treated as compensation liquid. The amount to compensate for eccentricity is determined using CAD program SolidWorks using the eccentricity measurements from Figure 3.10. The concerning volume turned out to be $5.2 * 10^{-6} \mathrm{m}^3$ ($\pm 0.7 * 10^{-6}$). This corresponds to about 5ml or 4.2g of Dowtherm A, depending on the liquid density at the working temperature.
Experiments were conducted with the heat pipe filled with 95g and 85g of Dowtherm A. This corresponded to a filling ratio of 0.153 and 0.135 at $340^{o}\mathrm{C}$, respectively. Annular flow was expected at 1090 and 1065rpm for the used filling amounts, which were accessible by the experimental setup.

During the experiments, the smell of Dowtherm A could clearly be detected, so vapors of the working fluid were escaping the heat pipe. This however did not mean it changes the amount of Dowtherm A notably, as very small concentrations of Dowtherm A could already be smelled. In order to find out if the leak altered the filling amount, the closed heat pipe was weighted regularly to find a possible weight change due to the loss of working fluid. The accuracy of the used scale was ±0.5g and the maximum weight difference found was 1g over four conducted experiments. This means between 0 and 2g of Dowtherm A has leaked out. The error margin of the filling amount therefore is between 0 and -2g. The error margin of the filling itself is orders of magnitude smaller.

3.4.2. Experimental procedure

A consistant procedure is followed, such that the conducted experiments were done in the same way. Not all constant variables were easy to keep constant during experiments. One of them is the non-condensable gas amount for example. This procedure is followed in order to obtain the most reliable results, which was still feasible.

Ambient conditions

As the experiments were conducted throughout different periods of the year, the ambient temperature varied slightly. The ambient temperature at days on which experimental data was acquired ranged from 16°C to 19°C. The effect of this slight temperature variation was considered negligible, as it is small compared to the working temperatures of the setup. Furthermore, the cabinet prevented air flows in the lab which would otherwise influence the experimental setup.

Non-condensable gas

The uncontrollability of the leak of the heat pipe complicated the study on the effect of non-condensable gas. The inaccuracy of the pressure sensor impeded this as well, as the measurements only gave an indication on the amount of air inside. During experiments, the data was analysed to check for signs of a change in non-condensable gas amount. With a constant amount assumed during experiments, the effect of variables on the influence of non-condensable gas could be studied by looking at the trend of the measurements. Therefore, measures were taken to analyse the amount of non-condensable gas during experiments and to keep this constant.

Running

The following procedure was followed during all the experiments conducted. The way the setup is controlled, including safety measures, is described in Appendix D.

1. The pressure was measured for at least 30 minutes prior to heating up, in order to obtain an average of the noisy pressure readings. This was done to get an indication of the amount of non-condensable gas inside the heat pipe.

2. The heating up was done at 200 rpm, with a gradually increasing lamp power and with low cooling fan power. From 240°C onward, the heating up was done with maximum oven power.

3. Prior to the actual data acquisition, the heat pipe was operated under maximal power at a temperature between 340°C and 350°C at 200 rpm for 30 minutes. A potential leak outwards would be highest at this operating condition due to the high pressure of about 5 bar. This step might reduce the non-condensable gas amount and would give information about the leak outwards. Furthermore, it ensured all components were heated to their stable temperature.

4. The cooling of the outside wiring tube was adjusted continuously to keep the temperature at the outside wiring tube sensor between 125°C and 130°C.

5. After the startup procedure, data acquisition was started. Different temperatures were reached in descending order, which would cause a decreasing leak due to the descending working pressure. Rotational speeds were reached in both descending and ascending order.

6. Once stability was achieved at the desired operating conditions, 100 data points were acquired during 100 seconds. The heat pipe was considered stable when all temperature readings stayed within 1°C and when all heat flux readings stayed within 150W/m^2 of the initial value over the period of 100 seconds. 150W/m^2 is around 1% of typical heat fluxes in oven and condenser and therefore falls well within the accuracy of the heat flux sensors.

Experiments typically took six to eight hours of which about 75 minutes were required for heating up. Stability was reached at desired operating conditions by adjusting lamp power and/or cooling air speed. Getting to stability at a new operating point took about 15 minutes.

During two experiments, the outside heat pipe temperature of the coated part in the oven has been measured during running with a thermographic camera. This part of the heat pipe

was visually accessible through the gap between the lower and upper oven panel. This was used to approximate the total heat input supplied by the oven, as described in Section 4.2.1. The thermographic camera used was of type FLIR TG165.

Working fluid degradation

The used working fluid was analysed for degradation by gas chromatography–mass spectrometry. The fluid was sampled right after emptying and stored in a closed container. The analysis was done by a laboratory of the University of Groningen. It was of added value as the degradation of Dowtherm A could result in a significant amount of extra non-condensable gas, which affects the experiments. A decomposition of 0.1% results in about 10% extra non-condensable gas for example. However, it is not very relevant for the suitability study of Dowtherm A as the working fluid of a heat pipe assisted annealing line, as the oxygen in the air was likely affecting the degradation. Air is not likely to be present inside the heat pipe in the application, as annealing is performed in an atmosphere of H_2/N_2. The data of the analysis is shown in Appendix E. It turned out that the extra amount of potential non-condensable gas is negligible. However, any vapors at ambient temperature were not caught after emptying and therefore also not found during the spectrometry.

3.4.3. Conducted experiments

This section provides an overview of the conducted experiments, of which the results are presented in the next chapter. Besides the overall performance of Dowtherm A as a working fluid, the effect of rotational speed, temperature and power are of main interest. Furthermore, the effect of non-condensable gas was tested.

Table 3.3 summarizes the conducted experiments with the TU Delft setup. During the experiments, one of the variables is changed, while the others are kept constant. Each line in the table, except for the last four, is an experiment carried out during a single day, represented by a unique non-condensable gas amount. The experiments with changing power are carried out during experiments with changing temperature and rotational speed.
The large amounts of non-condensable gas brought along a focus on higher temperatures and high powers, as the volume and axial length taken up by the non-condensable gas is significantly lower in these cases. Furthermore, the effect of the eccentricity turned out to be large at high rotational speeds, which caused this study to focus on the lower rotational speeds. A study on the effect of eccentricity would be interesting, but would not contribute to answering the research questions.

Table 3.3: Overview of conducted experiments, with variables: Inside temperature at oven(T), Rotational speed(ω), Oven power(P_{oven}) and Cooling air speed(v_{air}).

Changing variable	Range	Constant variables	NCG amount [g](approximate)	Filling
Temperature	$350-250^oC$	$\omega(200\text{rpm})$, $P_{oven}(100\%)$	0.15	85g
	$340-250^oC$	$\omega(200\text{rpm})$, $P_{oven}(100\%)$	0.20	:
	$350-250^oC$	$\omega(200\text{rpm})$, $P_{oven}(100\%)$	0.23	:
Rotational speed	$250-450$ rpm	$T(340^oC)$, $P_{oven}(100\%)$	0.18	95g
	$200-750$ rpm	$T(340^oC)$, $P_{oven}(100\%)$	0.18	:
	$200-1090$rpm	$T(340^oC)$, $P_{oven}(100\%)$	0.19	:
	$150-950$ rpm	$T(340^oC)$, $v_{air}(0.8\text{m/s})$	0.23	:
	$150-600$ rpm	$T(340^oC)$, $P_{oven}(100\%)$	0.24	85g
	$200-700$ rpm	$T(350^oC)$, $P_{oven}(100\%)$	0.40	:
	$1000-1090$rpm	$T(350^oC)$, $v_{air}(0.5\text{m/s})$	0.46	:
Power	P_{oven} : 90 & 100%	$T(340^oC)$, $\omega(200\text{rpm})$	0.15	85g
	P_{oven} : 79 & 100%	$T(330^oC)$, $\omega(200\text{rpm})$	0.15	:
	P_{oven} : 71 & 100%	$T(320^oC)$, $\omega(200\text{rpm})$	0.15	:

Accessing the values of the changing variables was done in the order as presented in the table. One of the variables was the power of the heat pipe, which was controlled by the oven and cooling power. Stability was reached by adjusting the variable which is not constant. Most of the experiments with changing temperature and rotational speed were carried out at maximum oven power, but two of them were carried out at lower power with a constant flow of cooling air. A constant oven or cooling power did not exactly mean a constant heat pipe power, as a relatively cold heat pipe absorbs more heat than a hot heat pipe and vice versa for the cooling duct. However, this deviation was small for a small temperature or rotational speed range. For the temperature and rotational speed changing runs, it was decided to keep either the oven power or cooling power constant instead of the heat pipe power in order to ease controlling the setup. Otherwise, it would increase the time to get to steady-state at another operating condition significantly. Most of the current experiments already took a full day.
The experiments with changing oven power at 200rpm were done in a special way. The low power settings of these three experiments at different temperatures were chosen such that the maximum axial vapor velocity inside the heat pipe remained constant, starting with 100% lamp power at 350°C. Vapor velocity plays a key role in the distribution of non-condensable gas and in the axial pressure drop. The expression for 1D axial vapor velocity is:

$$v_{ax} = \frac{P}{h_{fg}\rho_v A_{cs}} \tag{3.3}$$

in which P is the total power flowing from evaporator to adiabatic and condenser sections and A_{cs} is the cross-sectional area of the vapor space of the heat pipe. The maximum axial velocity scales with $P/h_{fg}\rho_v$, where the last two properties are temperature dependent. This expression was kept constant at different temperatures by adjusting oven and cooling power, such that the heat pipe was stable at the desired total heat input value and temperature.
The experimental study on the effects of non-condensable gas was impeded by the uncertainty on the amount of air inside the heat pipe and the unsystematic increase of the amount. However, a lot of data at different non-condensable gas amounts was available in which the trends could be studied. Of each non-condensable gas amount in Table 3.3 data was available at 200rpm and 340°C or 350°C. Furthermore, the effect of temperature and power variation on the non-condensable gas distribution was analysed.

By carrying out the experiments in Table 3.3, research questions one, two and three could be answered to the extent permitted by the setup. Furthermore, the effect of non-condensable gas could be analysed qualitatively. The data associated to the non-condensable gas was subsequently compared with the model presented in Chapter 5.

4

Experimental results & discussion

This chapter provides the results and discussion of the experimental campaign defined in Table 3.3 using the TU Delft rotating heat pipe. It is especially aimed at answering research questions 1, 2 and 3, an analysis on the overall heat transfer efficiency of Dowtherm A as an internal working fluid and the influence of rotational speed, temperature and power on internal heat and mass transfer. Furthermore, the effect of non-condensable gas is explored in this chapter, although no accurate measurement on the amount of non-condensable gas was possible. First, overall characteristics found will be presented, followed by an energy balance of the heat pipe in operation. Afterwards, a study on internal axial vapor and liquid flow is given. This provides information for a thorough analysis of the condensing and vaporization process. Last, experimental results pointing to a transition to the annular flow regime is presented. Experimental data on non-condensable gas will be compared with modelling results in the next chapter.

4.1. Overall characteristics

An ideal heat pipe would be characterized by the absence of an axial temperature gradient inside. Earlier in this report, it was shown that this is not always the case. The presence of non-condensable gas brings along a temperature gradient in axial and possibly radial direction at the condenser side of the heat pipe. Figure 4.1 clearly shows the significant effect of non-condensable gas during the experiments. First only the evaporator side heats up, after which the gradient decreases with increasing temperature. At about 250°C, the temperature gradient between first three inner thermocouples (TC) has disappeared almost completely. The gap with the fourth thermocouple is slowly closed with a further increase in temperature. This is as expected and can be explained by looking at the volume of non-condensable gas. Vapor pressure increases during heating up, causing an increase in air density and thus a decrease in volume taken up by the gas. $\mathrm{d}p/\mathrm{d}T$ inside the heat pipe increases with temperature, due to the relation between vapor pressure and temperature. For Dowtherm A, the vapor pressure rises slowly to 1 bar at a temperature of about 255°C and reaches 5 bar at 345°C. Furthermore, it looks like the readings are noisy in the region of coexistence of vapor and air, which could be explained by minor fluctuations in the non-condensable gas distribution. At room temperature, Dowtherm A has a vapor pressure of 0.00002 bar, so any pressure measurement at cold state above this value indicates non-condensable gas presence. This also implies that boiling only starts when vapor pressure of Dowtherm A has risen above the initial prevailing pressure.

Figure 4.2 shows typical local radial heat fluxes through the wall and both inner and wall temperatures at steady state. It is obvious that heat fluxes at the evaporator are larger than in the condenser. Maximum heat fluxes measured in the evaporator during experiments were around Besides the somewhat larger condenser, this is caused by heat losses at the adiabatic section and at the junctions between heat pipe and bearing blocks at the sides. A maximum

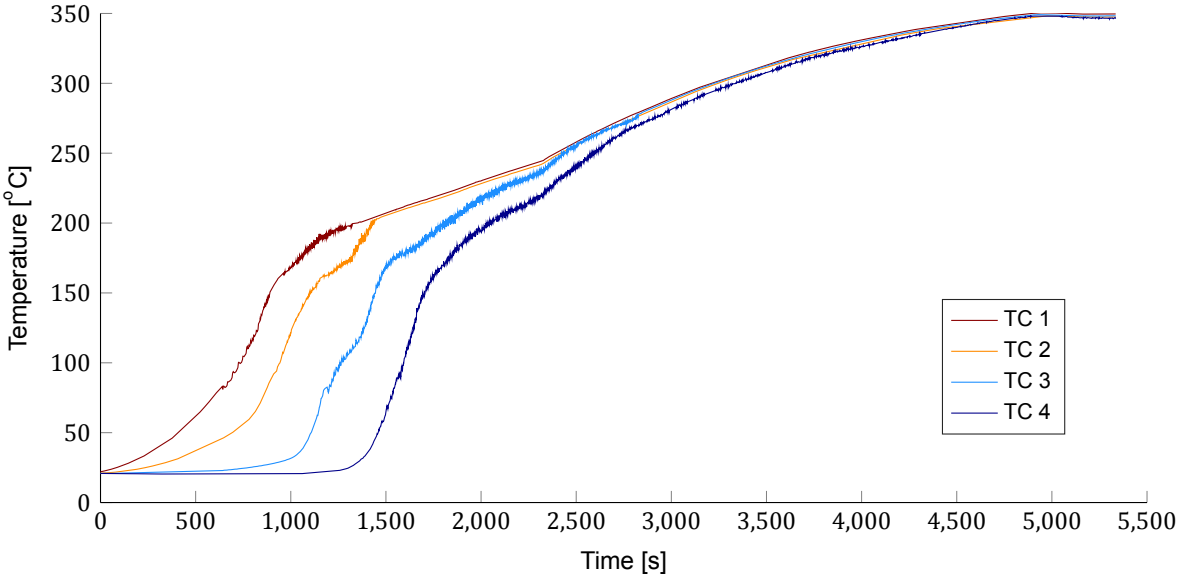

Figure 4.1: Inner temperatures during heating up of TU Delft Rotating Heat Pipe Setup(200rpm, $m_g \approx 0.15$g)

internal temperature difference of about 4°C is shown, while the maximum difference in wall temperature readings between oven and condenser is 40°C in this case. The low axial gradient of inner temperatures shows that the heat pipe is working. This graph also shows that there is a non-homogeneous axial wall temperature profile over the axial length of the heat pipe. Figure H.1 in the appendix shows the internal temperature profile for different operating temperatures. This figure shows that the axial inner temperature gradient mainly exists at the condenser end of the heat pipe. This is likely the cause of the present non-condensable gas. The difference between TC1 and TC3 typically is 1.7°C in the case of relatively high power and low non-condensable gas loading. This is smaller than the thermocouple error, so the presence of this axial temperature gradient cannot be told with certainty. ΔT_v is equal($\pm$0.1°C) for the different operating temperatures above 275°C, making the temperature drop unlikely to be from non-condensable gas effects, as the axial temperature drop due to non-condensable gas presence is expected to be strongly dependent on operating temperature/pressure. The difference between TC1 and TC4 typically is larger and dependent on operating temperature, showing the non-condensable effects at the condenser end of the heat pipe.

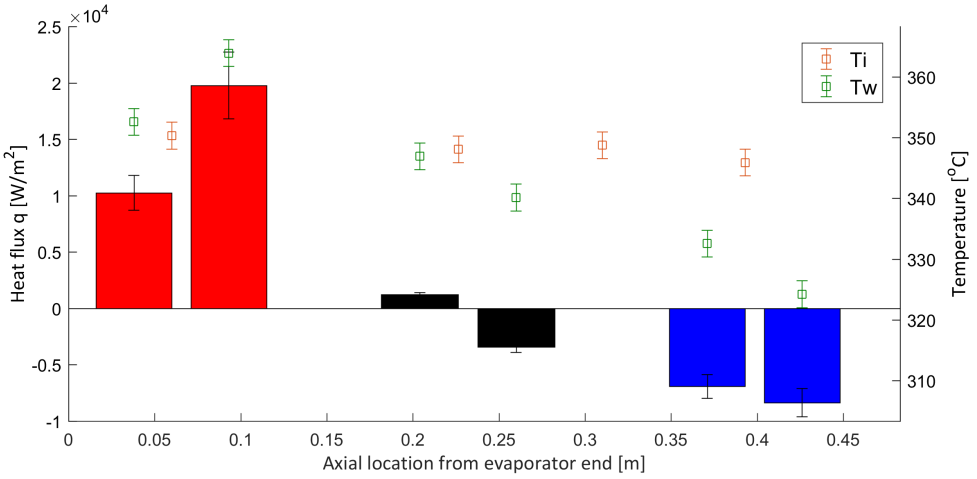

Figure 4.2: Radial wall heat fluxes (Q per unit area outside wall surface) with inside and wall temperatures. Operating conditions: $\chi = 0.14$, $m_g \approx 0.15g$, 200rpm and 100% lamp power

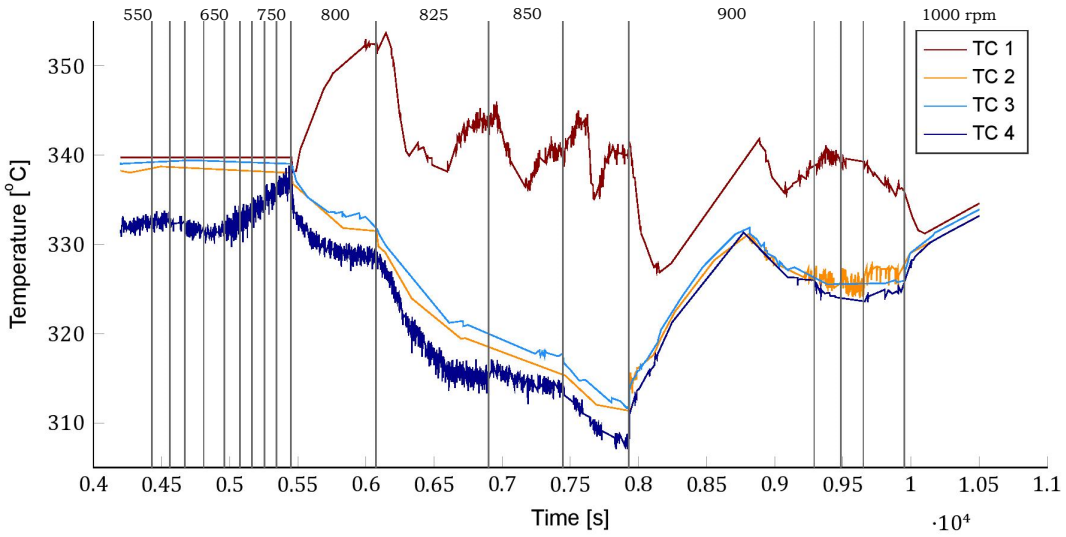

Figure 4.3: Typical inner temperatures during experiment with changing rotational speed near or at dryout. The rotational speed is increased with steps of 25 rpm, as indicated by the vertical lines and values at the top. Filling ratio: 0.16, lamp power 100%

Figure 4.3 shows an unexpected phenomenon, which was present at all conducted experiments with increasing rotational speed in the higher range. At a certain rotational speed, a large internal temperature difference between evaporator and other thermocouples appeared. At the same time, the heat transfer resistance between the wall internal surface and vapor space suddenly increases to more than 10 times its value at lower rotational speeds. The internal temperature difference is of another nature than the observed difference purely due to non-condensable gas. One can conclude that the axial vapor flow has stopped, which normally causes a homogeneous temperature distribution. This suggests vaporization has choked in the evaporator. Together with the very high radial heat transfer resistance observation in the evaporator, this allows the conclusion of a dryout causing this phenomenon. The observed high heat transfer resistance is then for heat flow from wall surface to internal vapor space directly, instead of boiling and liquid film resistance.
A dryout is caused by a too low liquid transport from condenser to evaporator. It should be high enough to accommodate the liquid feed at the vaporization rate. Flow resistance for axial liquid transport is very low for a pool. Annular flow on the other hand is more restrictive, but often goes hand in hand with high centrifugal forces, aiding the axial liquid transport. The Froude number $Fr = \Omega^2 r_{wi}/g$ is 15.7 at 800 rpm. The predicted Froude number for onset of annular flow according to two approaches is 39.1(Equation 2.5) and 16.1(Equation 2.6). Complete annular flow is expected at 49.0(Equation 2.2) and 30.5(Equation 2.6). The observed dryout rotational speed may be at the onset of annular flow speed, but is expected to be far from annular flow rotational speeds. The onset of annular flow normally starts at the sides and is likely to attract liquid from the neighbouring pool. Therefore, a dryout at 800rpm is unexpected, as it is in the non-annular flow regime with or without local annular flow at the sides, so restricted liquid transport is unlikely due to the presence of a pool. A pool has relatively low resistance to axial liquid transport, making the absence of liquid in the evaporator unlikely.
Table 4.1 gives the found dryout rotational speeds for a lower filling ratio. It is clearly visible that the power of the heat pipe is of influence on the dryout rotational speed. A higher power requires higher axial liquid transport and thus is likely to encounter dryout. This strengthens the argument of limited axial liquid transport at dryout symptoms. The values at different temperatures are not comparable, due to the heat pipe temperature dependency on heat input at a certain lamp power.
It was noted in Section 3.3 that an eccentricity exists in the middle of the heat pipe, which is the likely cause of the unexpected dryout, as expected behavior of a straight heat pipe is unable to explain dryout at this rotational speed. At rotational speeds with $Fr < 1$, liquid

will flow to the place with lowest height, which is depending on the angular position either the middle or the sides. The net flow will not be effected by this eccentricity in this case. At higher Froude numbers, the centrifugal force starts to dominate gravitational force, which causes liquid to accumulate in the region with highest distance from the axis of rotation, which is in the middle of the heat pipe, as illustrated in Figure 3.13. However, extra liquid has been added to compensate for this effect, so this does not explain the absence of liquid in the evaporator. An explanation clarifying dryout, is the onset of annular flow in the middle of the heat pipe, due to the eccentricity. This increases the amount of liquid in the middle and it may resist axial liquid transport. As no visual observations were possible, the effect of eccentricity is not certain. This possible cause for dryout has to be kept in mind when assessing further results of the experimental campaign.
Furthermore, Figure 4.3 shows that the heat pipe goes back to normal operation at high rotational speeds, in this case 1000rpm. This may be caused by the high centrifugal force aiding axial liquid transport and/or by entering the complete annular flow regime. Another interesting phenomenon is the decrease of the internal axial temperature gradient just before dryout. This suggests that the non-condensable gas is pushed further to the condenser end, which can be explained by the fact that less condensation takes place in the middle part of the heat pipe due to the high heat transfer resistance of local annular flow. This results in higher vapor velocities in the condenser, pushing the non-condensable gas to the condenser end of the heat pipe.

Table 4.1: Rotational speeds at which dry-out is suspected with filling ratio $\chi = 0.14$ of Dowtherm A inside at different lamp powers. Onset of annular flow according to Baker, Eq. 2.6: $Fr = 15.1$

Temperature/Non-condensable gas amount		Lamp power-low	Lamp power-high
240°C / ~0.2g		69%	80%
	dry-out at:(Fr)	860rpm(18.2)	830rpm(16.9)
300°C / ~0.2g		80%	100%
	dry-out at:(Fr)	790rpm(15.3)	730rpm(13.1)
350°C / ~0.5g		86%	100%
	dry-out at:(Fr)	750rpm(13.8)	725rpm(12.9)

This section has shown the significant effects of the present non-condensable gas and eccentricity of the rotating heat pipe. Non-condensable gas turned out to be of large influence at low temperatures and eccentricity at high rotational speeds. For this reason, the results discussion will be focused on high temperatures and rotational speeds lower than the rotational speeds of dryout. One exception to this is the analysis of the upper speeds, where the heat pipe retakes normal operation.

4.2. Energy balance

A heat balance formed with local heat flux and temperature measurements provides vital information for determining heat and mass flows at points where they were not measured. Local heat flux is measured at six different points in the wall, which is used to determine the total heat input by the oven, heat output in the condenser and heat loss in the adiabatic section. Furthermore, the energy balance is closed by estimating other heat losses.

4.2.1. Heat input by oven

Heat is supplied to the heat pipe by thermal radiation coming from halogen lamps. The profile of heat input by the oven is determined in this section by the heat flux measurements and by additional temperature measurements of the outside wall with a thermographic camera, as described in Section 3.4.2. The oven consists out of a central chamber and side chambers

at each side. The effective part of the halogen lamps is within the central chamber. The part of the heat pipe inside the central chamber was coated black to enhance heat absorption. Different oven sections and their size together with the relative sensors locations are schematically shown in Figure 3.8. For this analysis, the oven is divided in different sections and it is assumed that the heat input profile is symmetrical in axial direction. The profile on the left half of the oven is determined, which is equal to the other side under the assumption of symmetry.
A non-homogeneous heat profile is expected within the central oven chamber, as the amount of incident radiation at the sides is less due to a lower view factor to radiation. Figure 4.4 shows this expected profile and also shows the location of the wall sensors from which heat flux and temperature measurements are obtained. The central oven chamber is divided into a homogeneous and a non-homogeneous part. It is assumed that the wall sensor in the middle is in the homogeneous part. Furthermore, the uncoated parts of the heat pipe in the outside oven chambers are treated separately.

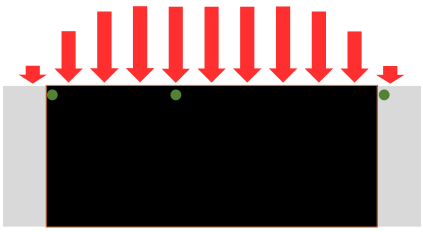

Figure 4.4: Expected profile of heat inflow in central and side oven chambers. The heat pipe part in the central oven chamber is coated black and therefore also drawn in black. The relative position of wall sensors are drawn in green.

Homogeneous part

The total heat input of the homogeneous part can be directly derived from the heat flux sensor in the middle, HF2. The total heat input of this section is given by:

$$Q_{hom} = (Q/\mathrm{d}z)_{HF2} L_{hom} \tag{4.1}$$

The length of this part, L_{hom}, is determined in the analysis of the non-homogeneous part.

Non-homogeneous part

This section is of main interest in this study, due to the unknown temperature and heat flux profile. Thermographic FLIR camera measurements of the outside wall were used to get to an estimation of the heat flux at the non-homogeneous coated part of the oven. FLIR measurements were done with a low amount of non-condensable gas, which ensured a homogeneous inner oven temperature.
This process is described in Appendix G and resulted in the following empirical expression for heat inflow in the non-homogeneous heating section of the oven:

$$Q_{non-hom} = 0.0374 T_{ev} + 0.024\Big((Q/\mathrm{d}z)_{HF1} + (Q/\mathrm{d}z)_{HF2}\Big) - 0.9282 \tag{4.2}$$

Where T_{ev} is the inside evaporator temperature in ^{o}C.

Side oven chambers

For the heat transfer of the outer chambers, heat flux sensor HF3 is used. This wall sensor is in the side chamber between central oven chamber and adiabatic section. The heat pipe in this section has no black coating and receives almost no radiation directly from the lamps, but it is covered by hot oven components. Heat flux measurements by HF3 were typically between 10% and 20% of HF2, in the middle of the oven. Homogeneous heat inflow is assumed in the side oven chambers:

$$Q_{sides} = (Q/\mathrm{d}z)_{HF3} L_{sides} \tag{4.3}$$

Total heat input

The numerous heat input sections discussed together form the profile as in Figure 4.5. The approximation of total heat input is the sum of Equations 4.1, G.5 and 4.3, according to:

$$Q_{oven} = Q_{sides} + 2Q_{non-hom} + Qhom \tag{4.4}$$

With $L_{sides} = 0.0415 + 0.047$ and $L_{hom} = 0.062m$

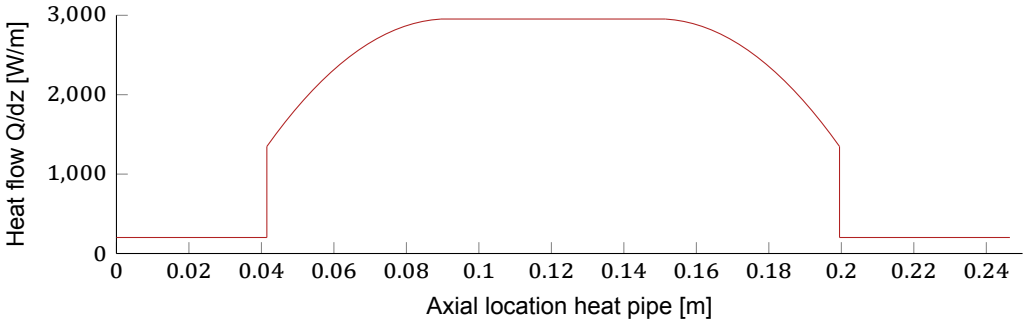

Figure 4.5: Heat input per unit length profile by oven as determined in this section

4.2.2. Heat output by cooling duct

The radial heat transfer through the wall is measured at multiple axial locations of the heat pipe. In the condenser, the heat transfer out of the heat pipe is caused by a convective and radiative heat transfer. The cross-flow of air inside the rectangular duct cools the heat pipe. Another part of the heat transfer is by radiation to the duct walls. First, total condenser heat outflow is determined from wall measurements, taking into account non-condensable gas. Furthermore, an expression for Q_{out} as a function of T_{wo} and v_{air} is determined. Heat transfer of a cylinder in a cross-flow of air can be calculated by a Nusselt number correlation. The effect of rotation of the cylinder is then added based on literature data. The expression for Q_{out} can be used in the model presented in the next chapter.

Total condenser heat outflow

The total outflow of the condenser by the cooling duct is difficult to determine as an axial temperature gradient due to non-condensable gas is present. No thermographic temperature measurements were done of the condenser, as the setup did not allow to do so while running. As shown earlier, non-condensable gas blocks the condenser partly. The blocked part of the condenser is significantly cooler, which causes heat outflow to be concentrated to the other part. The next chapter shows that region of coexistence of vapor and non-condensable gas compared to the uncertainty of front location, due to the unknown exact amount of air inside. Therefore, the front is assumed to be infinitely steep, making the blocked length of the condenser:

$$L_{blocked} = \frac{m_g}{\rho_g A_v} \tag{4.5}$$

Where A_v is the cross-sectional area of the vapor space, defined as $A_v = (1-\chi)\pi(r_{wi}^2 - r_{wiring}^2)$. The total condenser heat outflow is consequently approximated by taking the average of the two heat flux measurements in the condenser wall for the case where $(Q/\mathrm{d}z)_{HF6}$ is not significantly lower than $(Q/\mathrm{d}z)_{HF5}$, which indicates the front to be downstream of wall sensor 6. The total radial condenser outflow then is given by:

$$Q_{cond} = \frac{(Q/\mathrm{d}z)_{HF5} + (Q/\mathrm{d}z)_{HF6}}{2}\left(L_{cond} - L_{blocked}\right) \tag{4.6}$$

Where $L_{cond} = 0.186m$

Literature expression

The book Basic Heat and Mass Transfer of A.F. Mills provides the following empirical relation of the Nusselt number as a function of the Reynolds and Prandtl numbers for heat transfer between a cross-flow of air and a non-rotating cylinder[33].

$$Nu_d = 0.3 + \frac{0.62 Re_d^{1/2} Pr_{air}^{1/3}}{\left(1 + (0.4/Pr_{air})^{2/3}\right)^{1/4}} \qquad (Re_d < 10000) \tag{4.7a}$$

$$Nu_d = 0.3 + \frac{0.62 Re_d^{1/2} Pr_{air}^{1/3}}{\left(1 + (0.4/Pr_{air})^{2/3}\right)^{1/4}} \left(1 + \frac{Re_d}{282000}^{1/2}\right) \qquad (Re_d \geq 10000) \tag{4.7b}$$

in which:

$$Re_d = \frac{v_{air} d_{wo}}{v_{air}}, \qquad Pr_{air} = \frac{\nu}{\alpha} \tag{4.8}$$

Rotation of the heat pipe enhances heat transfer out by convection. Peller studied this increase in heat transfer by looking at experimental data and plotted the ratio of Nusselt number with and without rotation $MF_{rot} = Nu_d / Nu_d(v_{rot} = 0)$ against v_{rot}/v_{air} for $5.7 * 10^3 < Re_d < 7.13 * 10^4$ and $0 < v_{rot}/v_{air} < 1$, where v_{air} is the freestream velocity[38]. This plot is used to quantify the enhancement of rotation on the convectional heat transfer. MF_{rot} is seen as a multiplication factor for the convective heat transfer due to the rotation.
The heat transfer out by convection is then given by:

$$h_c = MF_{rot} \frac{Nu_d k_{air}}{d_{wo}} \tag{4.9}$$

$$Q_c = A_{wo} h_c (T_{wo} - T_{air}) \tag{4.10}$$

Another part of the radial heat transfer out from the heat pipe is by radiation. Radiative heat transfer can be calculated by the Stefan-Boltzmann law for the emittance of a black body. The total emissive power of a black body is defined as:

$$E_b = \sigma T^4 \tag{4.11}$$

Of course, the heat pipe of this study does not behave like a black body. The surface has an emittance ϵ based on its material and surface roughness. The emissive power of the heat pipe surface is:

$$E = A_{wo} \epsilon \sigma T_{wo}^4 \tag{4.12}$$

As ϵ of the stainless steel duct walls is not close to 1, reflection might have to be taken into account in order to get to an accurate expressions of the heat transfer. Mills provides the following expression of radiative heat transfer between two objects:[33]

$$Q_{12} = \frac{E_{b1} - E_{b2}}{\frac{1-\epsilon_1}{\epsilon_1 A_1} + \frac{1}{A_1 F_{12}} + \frac{1-\epsilon_2}{\epsilon_2 A_2}} \tag{4.13}$$

As every spot of the condenser wall only sees the duct wall, the shape factor $F_{12} = 1$. Equation 4.13 reduces to:

$$Q_{12} = \frac{\epsilon_1 A_1}{1 + \frac{\epsilon_1 A_1}{\epsilon_2 A_2}(1 - \epsilon_2)} (E_{b1} - E_{b2}) \tag{4.14}$$

The term $(\epsilon_1 A_1)/(\epsilon_2 A_2)(1 - \epsilon_2)$ in the denominator accounts for the reabsorbed reflected radiation of object 2 by object 1. This term can be neglected if it is close to unity. This is the case if A_2 is much larger than A_1 with a comparable value of ϵ for example. This expression of the radiative heat transfer assumes the duct to be isothermal.

The translation of this equation to the condenser results in the equation of the radiative heat transfer between heat pipe and duct walls:

$$Q_r = \frac{\epsilon_{wo} A_{wo}}{1 + \frac{\epsilon_{wo} A_{wo}}{\epsilon_{duct} A_{duct}} (1 - \epsilon_{duct})} \sigma \left(T_{wo}^4 - T_{duct}^4 \right) \tag{4.15}$$

The total radial heat transfer out is the sum of the convective and radiative heat flows described by equations 4.10 and 4.15 respectively.

$$Q_{out} = Q_c + Q_r \tag{4.16}$$

Experimental data comparison

Table 4.2 states the values used for the variable in the equations for convective and radiative heat flow. Figure 3.7 in the previous chapter shows the relevant dimensions and the position of the air velocity sensor.

Table 4.2: Values used for convection and radiation calculation

Variable	Value	Unit
v_{air}	$1.44 v_{intake}$	$[m/s]$
A_{wo}/A_{duct}	0.13	
T_{air}	295	$[K]$
T_{duct}	$(295 + T_{wo})/2$	$[K]$
ϵ_{wo}	0.55 [34]	
ϵ_{duct}	0.35 [33, 34]	

The Nusselt number expression of Equation 4.7 is for a cylinder in an unbounded flow of air. In the cooling duct of the TU Delft setup, the flow of air is bounded by the cooling duct. This results in an increased air velocity as the air flows along the heat pipe. For this approach, the Nusselt number for unbounded air is used, but with an adjusted value for v_{air} to take the local increased air velocity into account. For v_{air}, the average is taken of the freestream velocity, v_{intake}, and the maximum at full height of the heat pipe due to the decreased cross sectional area for the air flow.
The fraction A_{wo}/A_{duct} is the ratio between the area of radiation exchanging surfaces. A_{wo} is the area of the heat pipe in the cooling duct. A_{duct} is the area of the six surfaces of the cooling duct. The intake and outtake cross sections are taken as surfaces as well, as the connected ducts have little impact on the radiation and for simplicity reasons. The effect of this simplification is low.
T_{air} increases by about 2-6K from ambient temperature in the cooling duct, based on a simple heat capacity calculation as a function of the power and mass flow. An average value of T_{air} is used in the convection calculation. An estimation of T_{duct} is more difficult to get to. The duct temperature was not measured during the experiments. A rough estimate is made for the duct temperature. In this estimation, it is taken into account that any water droplets on the outside of the 2mm thick duct wall were instantly vaporizing during operation at high temperatures, which means the duct was well beyond 373K. It is assumed to be isothermal for this analysis.
The values for ϵ are taken from literature and interpolated to the values corresponding to the working temperatures used. The temperature dependence is limited for the range used, so constant values are taken.

The experimental data set contains many radial heat flow and wall temperature combinations with an associated air velocity. As described in section 3.2, the wall sensors are radially located as shown in Figure 3.9. For the heat flow calculations, the temperature and heat flow at the outside wall is needed. The heat flow derived from ΔT is equal at every radial position in the wall, provided that the flow of heat is not changing angle, e.g. from radial to partly axial when flowing outwards. For this heat outflow study, we want to use the heat flow from

measured ΔT, so the data is used upstream of the front where $\mathrm{d}^2T_w/\mathrm{d}z^2 \approx 0$. In this case, the heat flow is not changing in radial direction. T_w is transferred to T_{wo} by Equation G.1. Table 4.3 shows typical results of the comparison between experimental values and values from theory. For $v_{air} < 5\mathrm{m/s}$, the error is less than 25%. Theory over-predicts heat outflow at high temperature and under-predicts it for high air velocities. The deviation could be due to the fact flow is in a closed duct in this case, where flow is not restricted for the theory used. High air velocities occurred at low working temperatures.

Table 4.3: Results of theoretical heat transfer calculation for heat pipe in cooling duct using Equation 4.16, compared with measured values during experiments

RPM	Lamp p.	$T_{wo,5}[^oC]$	$v_{air}[m/s]$	MF_{rot}	$(Q/\mathrm{d}z)_{HF5}$	$(Q/\mathrm{d}z)_{theory}[W/m]$	% off
200	100%	329.7	1.6	1.07	1306	1591	21.8%
150	100%	317.6	0.4	1.11	809	821	1.5%
200	100%	314.6	2.8	1.05	1861	1833	-1.5%
200	71%	298.1	0.4	1.11	691	744	7.6%
200	100%	297.7	3.5	1.05	2145	1844	-14.0%
200	98%	265.9	4.4	1.03	22312	2080	-6.8%
200	100%	221.8	6.5	1.02	3125	2053	-34.33%
150	100%	212.5	4.8	1.02	2133	1656	-22.4%

4.2.3. Heat losses

Heat losses will always be present at rotating heat pipes, especially at high working temperatures. Bearings are often not able to handle high temperatures, due to which the sides need to be cooled, which results in axial heat losses. The TU Delft heat pipe was cooled at the wiring tube. No measurements were done to measure heat loss at the sides. The adiabatic section had a wall sensor, from which the heat loss can be approximated:

$$Q_{adia} = (Q/\mathrm{d}z)_{HF4} L_{adia} \tag{4.17}$$

Where $L_{adia} = 0.042\mathrm{m}$. The remaining heat losses, are the heat losses at the sides.

Figure 4.6a shows the total heat flows as approximated by Equations 4.4, 4.6 and 4.17 for a conducted experiment with low amount of non-condensable gas. The difference between Q_{oven} and $Q_{cond} + Q_{adia}$ indicates the size of heat losses at the sides. It is remarkable that $L_{blocked}$ is high and suggests that the entire condenser is blocked at 250°C, because the condenser wall heat fluxes still measure high heat fluxes, especially the one at the adiabatic side of the condenser, making a fully blocked condenser unlikely. The non-condensable gas amount, m_g, is calculated from inaccurate pressure measurements at cold state. The accuracy is 0.4 bar, which is higher than the absolute value in this case. Although the presence of non-condensable gas is certain from internal temperature profiles, it seems to be less drastic as is suggested by the pressure measurements. Figure 4.6b shows the energy balance without a blocked part of the condenser. These figures can be seen as a best and worst case scenario. The actual case will be in between. From the heat flow approximations at 350°C it can be seen that the heat losses at the sides are significant. Especially at high operating temperatures, these are expected to be high at the evaporator side, due to the forced cooling of the wiring tube to $125^oC - 130^oC$.
The condenser power in the case of 300°C was between 280 and 480W in the case shown in Figure 4.6. This means axial heat fluxes through the inner geometry between evaporator and condenser at this temperature are in the range of 192,000-330,000W/m^2. As these values are based on radial heat flux measurements in the wall, this is considered the power through the hollow space of the heat pipe. From Figure 4.2 a clear axial gradient in wall temperature is visible, which is in that case $\mathrm{d}T_w/\mathrm{d}z \approx 120\mathrm{K/m}$, resulting in an axial flow through the wall of $Q = -kA_w\mathrm{d}T_w/\mathrm{d}z \approx 3\mathrm{W}$, making it two orders of magnitude smaller than axial transport

through the vapor space. The wall temperature gradient in the condenser may be of influence on local condensation rate, as the wall at the adiabatic side of the condenser is relatively hot. This clarifies the lower radial wall heat flux measured at the adiabatic side of the condenser compared to the wall sensor further downstream, as the temperature difference between vapor space and wall is relatively low.

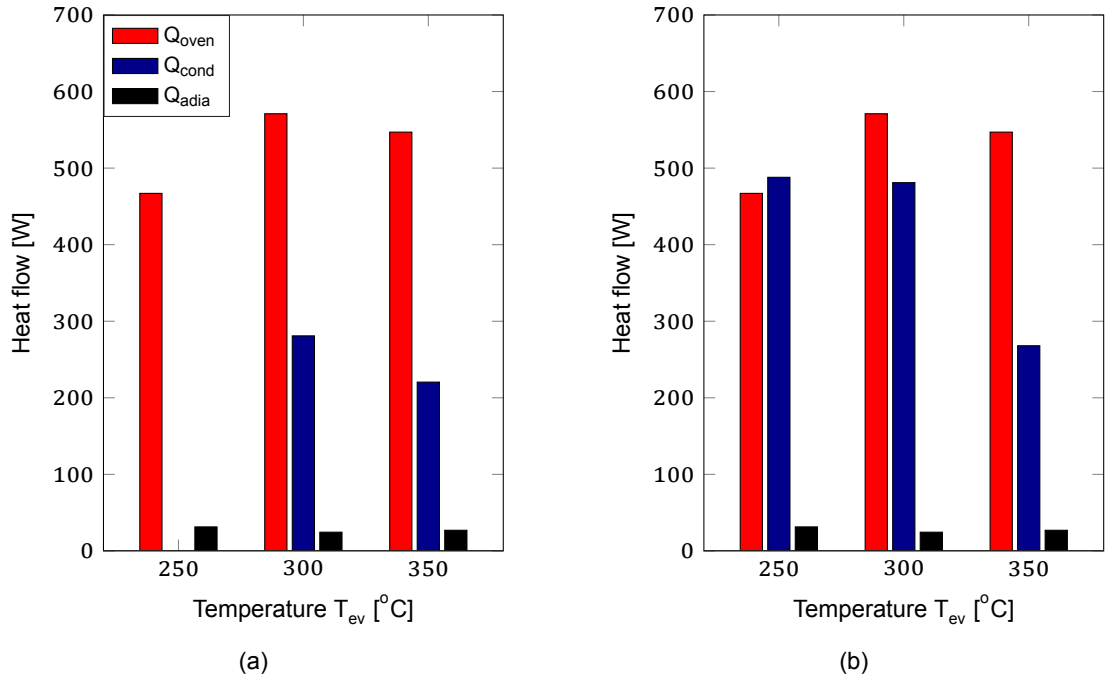

Figure 4.6: Plots showing approximated total energy flows of oven, condenser and adiabatic section. (a) shows Q_{cond} with $L_{blocked}$ as calculated by Equation 4.5. (b) shows Q_{cond} with $L_{blocked} = 0$. Working conditions: 200rpm, lamp power: 80%(250°C), 100%(300&350°C), $m_g \approx 0.15g$, $\chi = 0.14$

4.3. Axial transport of working fluid

Dowtherm A moves around the heat pipe serving as an efficient energy carrier between evaporator and condenser. This section describes the transport and elaborates on the driving force for this transport. The axial transport of vapor from evaporator to condenser is considered, and the transport of liquid back to the evaporator.

4.3.1. Transport of vapor

A pressure difference drives the flow of vapor from evaporator to condenser. This pressure difference is dependent on friction losses. Incompressible and fully developed flow is assumed for an approximation of friction losses of vapor flow through the annulus between inner wiring tube and liquid-vapor interface, of which the geometry is shown in Figure 3.2. First, the Reynolds number for axial flow is defined as:

$$Re_d = \frac{\rho_v v d_e}{\mu_v} \tag{4.18}$$

$$d_e = \frac{4 \text{ x cross-sectional area}}{\text{perimeter}} = \frac{4\pi\left((r_{wi} - \overline{\delta})^2 - r_{wiring}^2\right)}{2\pi\left((r_{wi} - \overline{\delta}) + r_{wiring}\right)} = 2\left((r_{wi} - \overline{\delta}) - r_{wiring}\right)$$

In which the liquid distribution is assumed to be annular. The method for determining pressure loss described in the book: Heat pipes: theory, design and applications[41] is used. For laminar flow, the Hagen-Poiseuille equation is used, while turbulent flow pressure loss

comes from the Fanning equation:

$$\mathrm{d}p/\mathrm{d}z = \frac{-vA_v 8\mu_v}{\pi\left(r_2^4 - r_1^4 - \frac{(r_2^2 - r_1^2)^2}{ln(r_2/r_1)}\right)} \quad (Re_d < 2100) \tag{4.19}$$

$$\mathrm{d}p/\mathrm{d}z = -\frac{4}{d_e} f \frac{1}{2}\rho_v v^2 \quad (Re_d > 2100) \tag{4.20}$$

In which $r_2 = r_{wi} - \overline{\delta}$, $r_1 = r_{wiring}$ and $f = 0.0791/Re_d^{0.25}$ according to the Blasius equation. Highest pressure losses are expected at high vapor velocities, which appear at low operating temperatures due to the relatively low vapor density. The pressure loss in the worst case is calculated; at 250°C with a typical heat input of 475W. For the worst case scenario, it is assumed that all vapor flows from one end of the heat pipe towards the other end. Normally, a velocity profile exists, as vapor vaporizes and condenses on its way. $v_{max} = Q/h_{fg}\rho_v A_v = 0.37\mathrm{m/s}$, $d_e = 0.0318\mathrm{m}$ and $Re_d = 4096$. As the Reynolds number is not equal along the vapor flow path, both laminar(Equation 4.19) and turbulent(4.20) pressure loss is calculated and result in: $\mathrm{d}p/\mathrm{d}z = -0.17$(laminar) and $-0.29\mathrm{Pa/m}$(turbulent). The pressure loss is therefore not expected to be higher than $\mathrm{d}p/\mathrm{d}z\mathrm{L} = 0.14\mathrm{Pa}$. A drop in pressure causes a lowered T_{sat}, but in this case that is limited to a change of 0.0001K and therefore is considered negligible. Besides the friction loss, a pressure change is caused by accelerating the vapor to v_{max}. This can be calculated by: $\Delta p = \rho_v v_{max}^2 = 0.5\mathrm{Pa}$. This pressure change is of the same order of size as the friction loss and is therefore considered to be negligible as well.
This simple calculation showed that the pressure change due to flow in the TU Delft heat pipe setup causes a negligible temperature change over the axial length. In Section 4.1 it was shown that a typical internal temperature difference of 1.7°C was measured upstream of the region which was affected by non-condensable gas, although the thermocouple error is too large to conclude with certainty. Due to the negligible calculated flow friction, this temperature gradient is unexpected. An explanation could be that the vapor in the evaporator is superheated by about 1.7°C, but it could also be a measurement error.

4.3.2. Transport of liquid

The driving force for liquid transport is either gravitational or centrifugal force. In non-annular flow, a pool exists which is not rotating itself and therefore gravitational force will be causing an axial pressure gradient, driving liquid transport. The pressure gradient follows from a liquid height difference, resulting in hydrostatic pressure. In the annular flow regime, Froude numbers are high and liquid layer will therefore be exerted to dominant centrifugal forces. Due to the very thin liquid film in the non-annular flow regime, it is assumed that all liquid transport goes via the pool. Bertossi et al. derived an equation for the axial gradient of liquid layer thickness as a function of mass flow for annular flow based on momentum conservation equations and a no-slip condition at the wall, with the assumption of negligible shear stresses at liquid-vapor interface[10]:

$$\frac{\mathrm{d}\overline{\delta}}{\mathrm{d}z} = \frac{-3\mu_l}{\rho_l^2 r_{wi}\Omega^2 \overline{\delta}^3} \frac{\dot{m}_l}{2\pi r_{wi}} \tag{4.21}$$

Although this equation is based on an axisymmetric, this equation is adjusted for the analysis of liquid transport in the pool to get to an estimation. The average height of liquid in a circle segment $\overline{h}$ is used in this calculation and centrifugal force $r_{wi}\Omega^2$ is replaced by gravitational force g:

$$\frac{\mathrm{d}\overline{h}}{\mathrm{d}z} = \frac{-3\mu_l}{\rho_l^2 g \overline{h}^3} \frac{\dot{m}_l}{2r_{wi} sin(1/2\theta)} \tag{4.22}$$

$$\overline{h} = \frac{A_l}{2r_{wi} sin(1/2\theta)}$$

Where pool angle θ is defined by Equation 2.10 and A_l is the cross-sectional area of liquid, in which the film area is considered negligible compared to the pool. Calculating the pool height

difference over the length of the heat pipe using Equation 4.22 using the average pool height will give a conservative value, due to the third power of $\overline{h}$. In the case without a partly blocked condenser, the distance of condensation and vaporization are on average 0.26m apart. For the most viscous and conservative case, at 250^oC with a viscosity μ_l of 0.00028Pas, the low filling ratio of 0.135, $Q = 475W$, $\dot{m}_l = Q/h_{fg} = 0.0016kg/s$, $\theta = 1.82rad$, $\overline{h} = 0.0059m$ this yields $\mathrm{d}\overline{h}/\mathrm{dz} = 2.5 * 10^{-5}m/m$, resulting in a height difference of $7 * 10^{-6}m$, which is only 0.1% of the height of the pool.
In the case of annular flow at a rotational speed of 750rpm, a height difference of $2.3 * 10^{-5}m$ is calculated by Equation 4.21, which is 0.4% of $\overline{\delta}$. For this calculation, the filling compensation amount for eccentricity is deducted, as this liquid is expected to only be in the middle of the heat pipe. This gives a filling ratio $\chi = 0.128$. A filling ratio of 0.04 would result in a thickness difference in the same order as the liquid layer thickness itself, which makes a dry-out theoretically possible.
This section showed that the head required for axial liquid transport is negligible for our operating conditions at both non-annular and annular flow. Liquid transport should be severely obstructed in order to be too low and causing a dry-out.

4.4. Heat transfer condenser

The heat transfer in the condenser is of significant effect to the overall performance of a rotating heat pipe. This is due to the relatively high heat transfer resistance of conduction through the liquid film or layer, which is the concerning heat transfer mechanism in the condenser, as described in Section 2.1.2. Therefore, the liquid film thickness for non-annular flow is included in this analysis, as well as the effect of turbulence inside the film. Figure 4.3 showed the severe effects of dry-out, likely caused by the eccentricity of the heat pipe. This analysis of heat transfer in the condenser is limited to rotational speeds lower than the rotational speed at which dry-out occurs, due to the disruptive effect of dry-out, which is not considered as a normal heat pipe operation. Furthermore, results with minimal effect of the non-condensable gas are presented. The effect of non-condensable gas on heat transfer is handled in Chapter 5.

It is assumed that the radial pressure gradient in the vapor space is negligible, $\mathrm{d}p/\mathrm{d}r = 0$, as the radial flow of vapor is very small. Furthermore, due to the negligible resistance of condensation itself, it is assumed that the liquid-vapor interface is at the saturation temperature of Dowtherm A. From the working principle of heat pipes and the absence of a radial pressure gradient, it can be concluded that also no radial temperature gradient exists in the vapor space. It is consequently assumed that condensation only happens at the vapor-liquid interface, due to the absence of a radial temperature gradient. Last, it is assumed that all heat transfer takes place through the film and not through the pool, as the pool height is more than 50 times larger than the expected film thickness during the experiments of this study.
From Section 4.3.2 it became clear that the liquid is equally distributed along the heat pipe in the case of non-annular flow in a heat pipe with no eccentricity. Eccentricity is expected to have little effect at low rotational speeds, at low Froude numbers. With this information, the liquid film thickness can be calculated using Equations 2.8 and 2.9 derived by Semena and Lin respectively. The outcome of these equations for film thicknesses expected in the TU Delft setup are shown in Figure 4.7. The working conditions of the TU Delft heat pipe fall just outside the region for which the expression of Semena holds, so the accuracy of the relation in this region is uncertain. Lin provided a more general expression. At low rotational speeds, the two expressions are very similar. Higher rotational speeds show a larger discrepancy. Lin approximates a lower thickness there. The typical temperature dependency is also shown in this graph, which is mainly due to the change in viscosity. A lower temperature yields a thicker film. The dependency on the filling ratio is considered low. It is not part of the expression of Lin and the dependency of Semena's expression on filling ratio is minor, only about 2% for the two different filling amounts of this study. The thickness in case of annular flow is about 0.0016m.

A notable difference in this study compared to Semena's and Lin's is the relatively high volumetric rate of vaporization and condensation, due to the low latent heat of vaporization of Dowtherm A. Semena did not include vaporization and condensation and although Lin researched a rotating heat pipe with higher power, it still does not make up for the about ten times lower value of latent heat of vaporization of Dowtherm A compared to water. Therefore, a correction is set up for the film thickness change due to condensation and vaporization. Condensation adds liquid to the film and liquid is removed from it by boiling. As the film moves with the same speed as the wall, v_w, the relative size of the correction is large at low rotational speeds. It is assumed that phase change happens homogeneously over the film, which results in the biggest effect to be seen in the film where it is about to return in the pool and no effect on the film is yet seen where it is pulled out of the pool. The average thickness change for evaporator and condenser then can be given by Equation 4.23, which is negative for the evaporator and positive for the condenser. The corrected film thickness is included in Figure 4.7. One could conclude that the effect is significant at low rotational speeds, which results in an evaporator film thickness to approach zero locally. In this case, the amount of liquid in the film is too low for the power of the heat pipe, which results in a not fully wettened wall surface, which in turn increases heat transfer resistance of the evaporator. The rotational speeds from this study started from 150rpm, showing a less severe correction. $\Delta\delta$ is higher for the evaporator due to the higher heat fluxes in the oven.

$$\Delta\delta = \pm\frac{1}{2}\frac{Q/\mathrm{d}z}{h_{fg}\rho_l v_w} \tag{4.23}$$

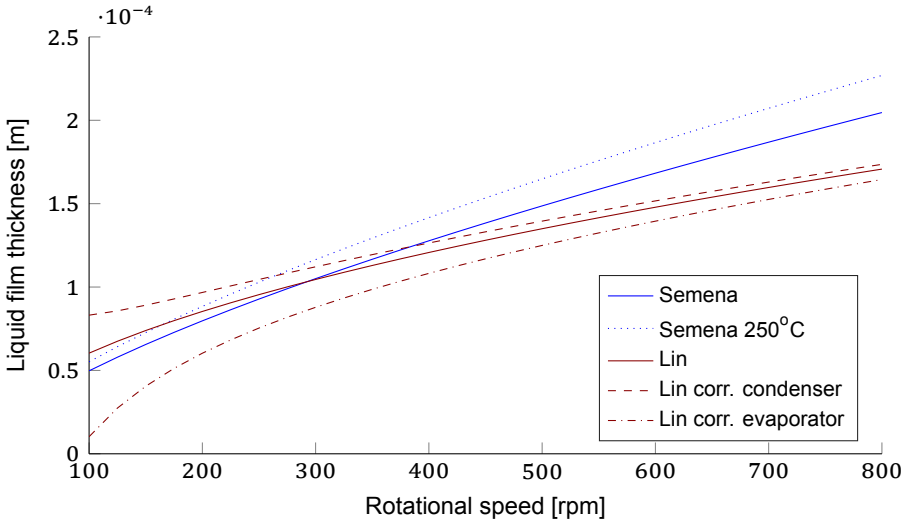

Figure 4.7: Liquid film thickness calculation for TU Delft heat pipe at 340^oC, 100% lamp power and 0.16 filling ratio by expressions from Semena and Lin. Figure includes temperature dependency and applied film thickness correction of Equation 4.23.

In the following graphs, experimental results are compared to expressions found in literature. The data of wall sensor 5, the sensor at the adiabatic side of the condenser, is used, as it is expected to suffer less from non-condensable gas inside the heat pipe. First, the internal wall surface temperature is determined using wall measurements as follows:

$$T_{wi} = T_w + \frac{Q/\mathrm{d}z \ln\left(\frac{r_w}{r_{wi}}\right)}{2\pi k_w} \tag{4.24}$$

Subsequently, a measure for resistance is found in the numerator of the equation below, $R\mathrm{d}z$:

$$Q/\mathrm{d}z = \frac{\Delta T}{R\mathrm{d}z} = \frac{\left((T_i)_3 + (T_i)_4\right)/2 - (T_{wi})_{HF5}}{R\mathrm{d}z} \tag{4.25}$$

Where ΔT is the temperature difference over the film or liquid layer. As it is assumed that no radial temperature gradient exists, it is the difference between inner wall surface temperature and the temperature in the middle of the heat pipe. For the condenser, this is the average of measurements by TC3 and TC4, of which the locations are shown in Figure 3.8. Results following from film thickness calculations are plotted as Rdz using Equation 2.12 and turbulent transport is included from Equation 2.13.

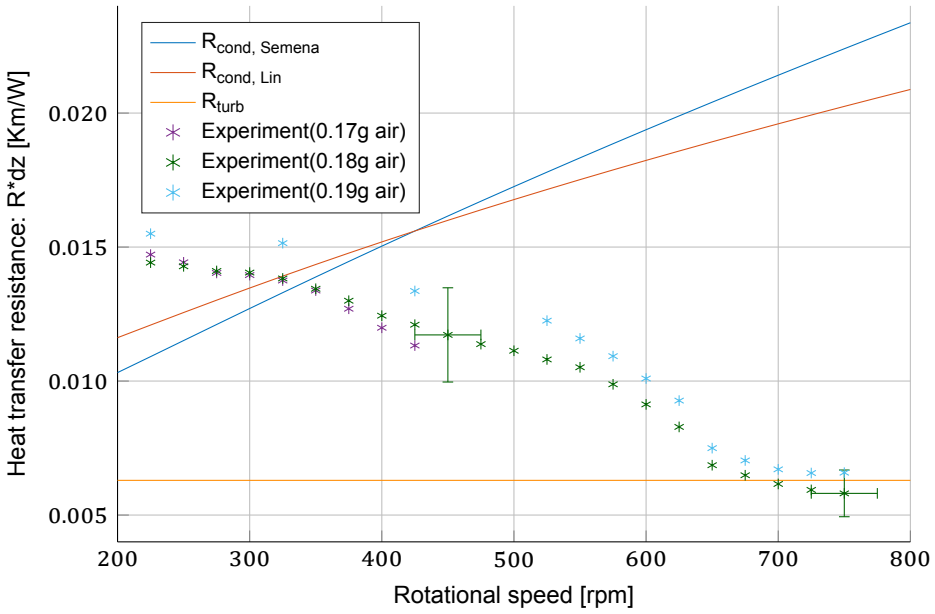

Figure 4.8: Condenser heat transfer resistance of liquid film for different rotational speeds. Solid lines are the resistances calculated using corrected layer thicknesses for conduction and Equation 2.13 for transport due to turbulence. Working conditions: $T_{ev} = 340^oC$, 100% lamp power, filling ratio χ=0.16

Figure 4.8 shows the film resistance versus rotational speed of the heat pipe, ranging from about 0.015 to 0.006Km/W. For comparison; The resistance of radial conduction through the wall is much lower, $(R * \mathrm{d}z)_w = 0.0027$Km/W. With the assumption that all radial heat transport happens outside the pool, where surface fraction outside the pool $\xi = 0.69$, the heat fluxes through the film ranged from about 20875(225rpm) to 24000(750rpm)W/m^2 for the data points plotted. A decreasing trend is visible in the experimental results. The difference between the three conducted experiments is small, although the experiment with the most amount of non-condensable gas looks to show a higher resistance. According to the expression of turbulent heat transport, it is the dominant heat transfer mechanism in the entire range plotted. Resistance for conduction is also shown in the plot, which increases due to the increases in film thickness with rotational speed.
The results of these experiments are overall different than the values derived from literature. First of all, the resistance at low rotational speed is in the same order as the expected resistance for conduction, but it is definitely higher. It is far from the expected values due to turbulent transport. Dowtherm A shows no sign of turbulent transport at low rotational speed from this plot. Secondly, the experimental values are decreasing, while the theoretical value either stay constant or increase with rotational speed. Due to the effects of eccentricity, it could be that the pool is becoming smaller in the condenser with increasing rotational speed. As the liquid thickness is considered independent of filling ratio, this is not expected to result in a thinner film at high rotational speed. However, the area for heat transfer, ξ, increases with a decrease of the pool height. This does however not fully clarify the difference between low and high rotational speed. Another effect could be that turbulent transport is starting to have its effects on heat transfer through the film. It is remarkable that the values at the upper rotational speeds show good agreement with turbulent resistance value.
One should note that the way of determining resistance from experimental values could lead

to inaccuracy when non-condensable gas is present, as the internal temperature at the axial location of the wall sensor is not measured, but taken as an average of two measurements at closest axial locations according to Equation 4.25, which may vary due to the prevailing non-condensable gas. Furthermore, non-condensable gas could cause a radial temperature gradient, which increases resistance as calculated. Figure 4.3 shows the typical decreasing temperature difference between TC3 and TC4 prior to dry-out, which suggests that the region with non-condensable gas effects starts more downstream. Therefore, the accuracy is expected to be higher at the high rotational speeds before dry-out, as the influence of non-condensable gas is lower. The most accurate obtained radial heat transfer resistance of the film in the condenser is therefore considered to be just before dry-out: $R * \mathrm{d}z = 0.006\mathrm{Km/W} \pm 15\%$, which equals a heat transfer coefficient $h = 1750\mathrm{W/m^2K} \pm 15\%$ at $750\mathrm{rpm}(Fr = 13.8)$ with an expected liquid film thickness $\delta = 0.00017\mathrm{m}$(Lin,corrected).

Figure 4.9 shows resistance versus working temperature of conducted experiments at constant rotational speed. A clearly decreasing trend could be seen from the experimental data, although the predicted values show a slightly increasing resistance with temperature, which is mainly due to a decrease in conductivity. The resistance to heat transfer by turbulent transport decreases slightly. At low temperatures, the found resistances show a large discrepancy.
The most obvious explanation is the effect of non-condensable gas again. The volume of non-condensable gas decreases with temperature and so its influence will decrease as well. The way of calculating used can be inaccurate with the presence of non-condensable gas and 2D effects of it causes a radial temperature profile in the vapor space, increases resistance as calculated. As already discussed in the resistance-rotational speed graph, the values at high temperature are in the same order as the resistance for heat transfer by conduction.

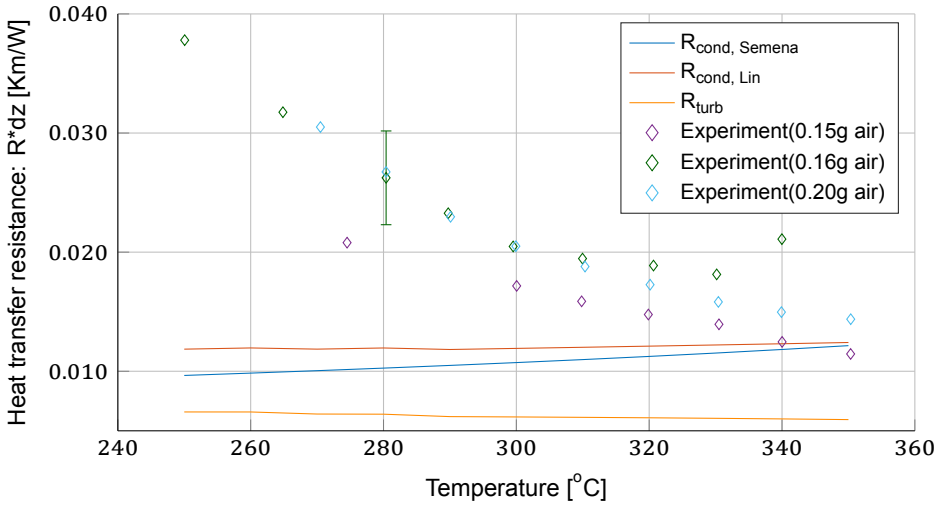

Figure 4.9: Condenser heat transfer resistance of liquid film for different internal temperatures T_{ev}. Working conditions: 200rpm , 100% lamp power, $\chi = 0.14$

4.5. Heat transfer evaporator

For the analysis of the vaporization process, the same method is followed as for the condenser in the previous section. More accurate results are expected, due to the limited effect of non-condensable gas in the evaporator. This time, wall sensor 2 is used, which is in the homogeneous part of oven.

Figure 4.10 shows the resistance of the film versus rotational speed. Typical resistances of $R * \mathrm{d}z = 0.0025\mathrm{Km/W}$ were found, which corresponds to a $h = 4200\mathrm{W/m^2K}$ of the film. The experimental results are closely related and are slightly decreasing with rotational speed.

Again, heat transfer resistance by conduction is plotted. The correction of Equation 4.23 causes the film thickness to be very low at the start rotational speed. Also natural convection in the film is considered, starting from $Ra > 400$, in this case from 575rpm. Furthermore, the resistance to heat transfer due to turbulent flow is predicted to be lowest and independent of rotational speed. A fourth heat transfer mechanism, nucleate boiling according to Equation 2.20 is included, which is found to occur at least till a centrifugal force of 20g. The error is in the order of 100% of the heat flux, which makes it predicting only the order of size of the heat transfer resistance.
The resistance to heat transfer across the liquid film is significantly lower than the values predicted for different transfer mechanisms at all shown rotational speeds, except for nucleate boiling. This is in contrast to condenser results, which yielded mostly higher resistance values than predicted. Furthermore, both condenser and evaporator results show a decreasing trend. In the condenser this was most probably partly caused by non-condensable gas effects. It is very unlikely that non-condensable gas is present in the evaporator. The slight decrease could be caused by a decrease of pool angle θ and therefore an increase in surface fraction prone to vaporisation ξ, it could be caused by more turbulent transport than predicted by literature or it could be the centrifugal force helping transport by either enhancing natural convection and/or nucleate boiling.
The only mechanism resulting in comparable low heat transfer resistance is nucleate boiling. The theory used for this prediction is based on pool boiling, which is likely to be different than for a thin film. However, as all other mechanisms have higher resistances and nucleate boiling has shown to be possible in rotating heat pipes at the concerning centrifugal forces, it is most certain that nucleate boiling is the dominant heat transfer mechanism. The resistance corresponds to a film thickness of $2.3 * 10^{-5}$m for pure conduction, which is about half the thickness approximated by Lin at 175rpm and one fifth of the thickness at 400rpm. The effect of eccentricity is considered to be minimal at low rotational speeds.

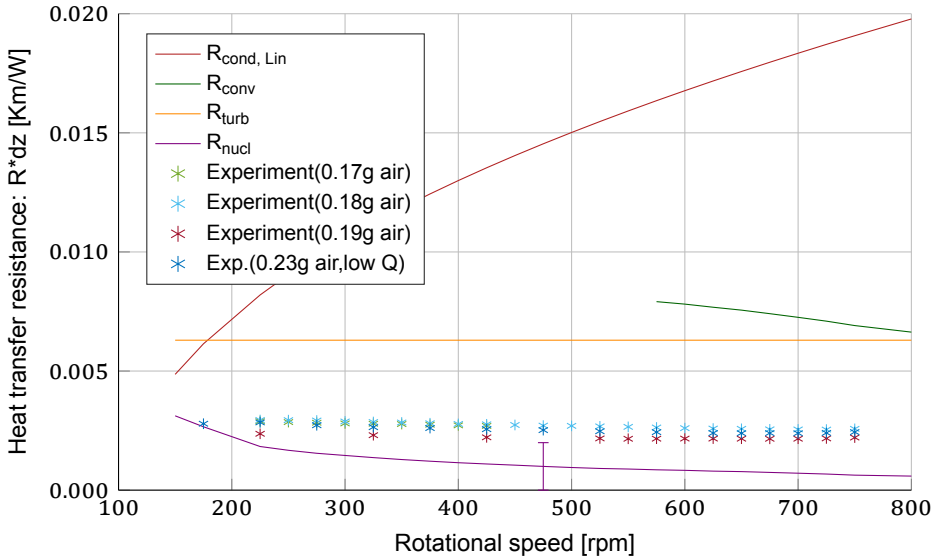

Figure 4.10: Evaporator heat transfer resistance of liquid film for different rotational speeds. For Rayleigh numbers larger than 400, resistance for natural convection is shown. Working conditions: $T_{ev} = 340^oC$, 100% lamp power, filling ratio of 0.16

Figure 4.11 shows heat transfer resistance versus internal temperature. The approximations show a decreasing resistance with temperature, mainly due to an decrease of viscosity μ_l. The experimental data seem to show this decreasing trend as well, but show a lower resistance. The error of nucleate boiling is large, 100% of its value as shown in the graph. The correlation for nucleate boiling is based on pool boiling, while in this case the heat transfer takes place through a film, which brings along uncertainty as well. One should also note that the film thickness is low at 200rpm, causing the resistance of conduction to be close to

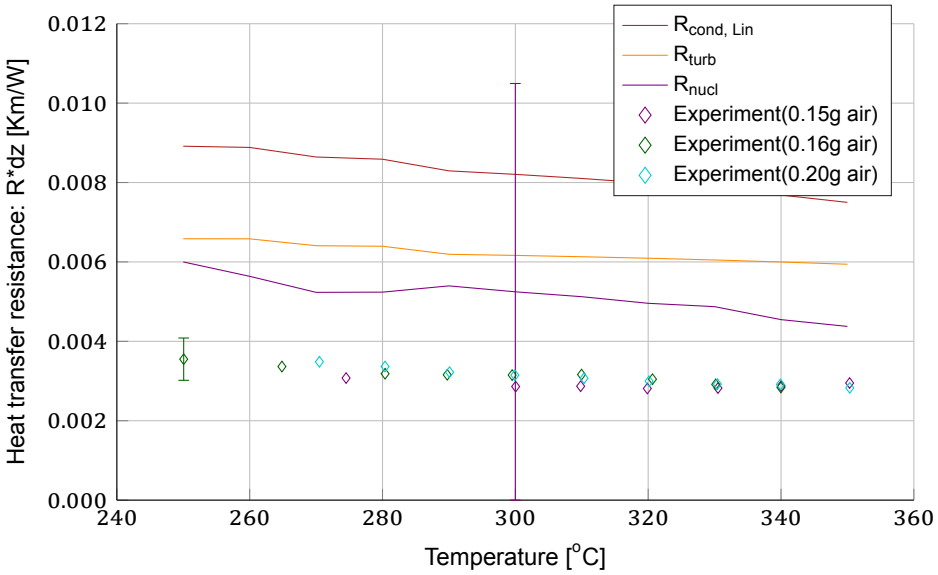

Figure 4.11: Evaporator heat transfer resistance of liquid film for different internal temperatures T_{ev}. Working conditions: 200rpm , 100% lamp power, filling ratio of 0.14

the other mechanisms.
Figure 4.12 shows resistance for different powers at multiple inner temperatures. The difference in resistance between condenser and evaporator is clearly visible. Furthermore, a strong dependency on resistance as calculated for the condenser is visible, but this does not apply to the evaporator. At the evaporator, a slight decrease in resistance can be seen. The large decrease for the condenser can be explained by non-condensable gas being pushed further to the condenser end due to an increase in vapor speed with power. This could have decreased local radial temperature gradient and thus resistance. Condenser heat transfer rates tested radially through the film were in the range 7300-24000W/m^2. For the evaporator this was higher: 26200-39300W/m^2. The used expressions from literature either considered conduction, natural convection, turbulent mixing and nucleate boiling as the driving force for heat transport. As discussed in Section 2.1.3 and shown in Figure 2.2, different boiling mechanisms occur at different temperature differences for unforced flow. As the experimental data show a slight decrease of the resistance with power, transition boiling seems to be not the case during our experiments. An approximation of q_{max} is made using Equation 2.18 to check whether typical heat fluxes during conducted experiments were close to the stop of nucleate boiling. Equation 2.19 gives the maximum velocity of vapor. For the conservative case at 250°C, at low vapor density and low rotational speed(200rpm), maximum vapor bubble velocity through film is $v_{max} = 0.53$m/s. For a typical value of C_{max} of 0.1 in Equation 2.18, this results in $Q/\mathrm{d}z_{max} = 6000$W/m at restricting operating conditions. This is well above the maximum heat fluxes seen during the experiments and therefore it is expected to not reach transition or film boiling.

4.6. Annular flow

The results presented in this chapter fully focused on the non-annular flow regime, as dryout severely obstructed heat pipe operation at high rotational speed. However, at even higher rotational speeds, the heat pipe of this setup started operating again, which could be seen from the disappearance of the axial temperature gradient in Figure 4.3. Section 2.1.1 presented two ways of predicting the rotational speed at which complete annular flow is expected, namely Equation 2.2 and 2.6.
Figure H.2 in the appendix shows resistances for evaporator and condenser in the upper range of rotational speeds for two different filling ratios, $\chi = 0.13$ and 0.15. The compensation amount for eccentricity has been subtracted, as this liquid is assumed to be fully in the mid-

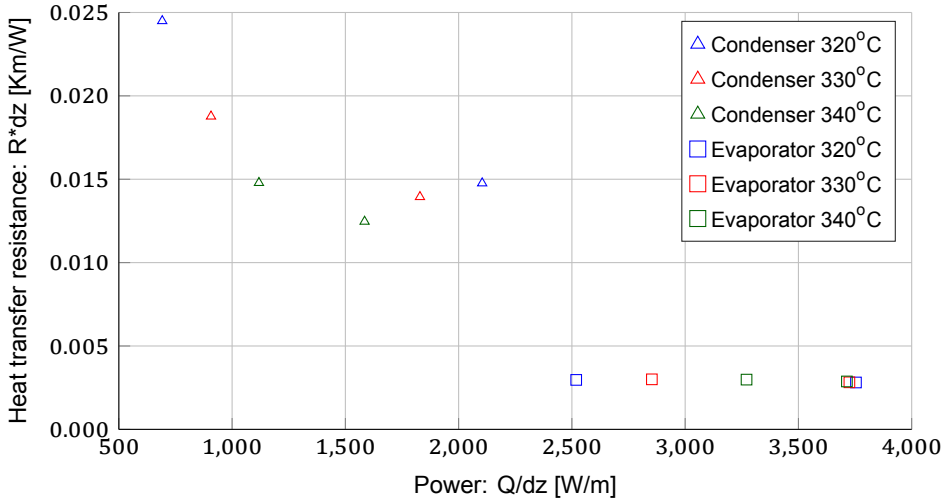

Figure 4.12: Heat transfer resistance of liquid for different local powers at condenser and evaporator at different internal temperatures T_{ev}. Working conditions: 0.15g air, 200rpm, filling ratio of 0.14

dle of the heat pipe due to the high Froude number. The graph clearly shows a large jump in condenser resistance at 1050rpm($\chi = 0.13$) and 1070rpm($\chi = 0.15$) at 340°C. The condenser resistance increases by more than 5 times, while the evaporator stays more or less constant. This matches the expectations of annular flow. A significant increase in liquid layer occurs when going from non-annular to annular flow. As the heat transfer mechanisms in the condenser are not expected to be enhanced by centrifugal force in particular, this significant increase in layer thickness is likely to cause a large increase in resistance. This does not hold for the evaporator, as nucleate boiling resistance is not dependent on layer thickness, according to Equation 2.20. As the centrifugal force is about 30g, nucleate boiling may be partly suppressed, but can still be the dominant heat transfer mechanism.
According to Baker's expression for the Froude number of complete annular flow, the transition is expected at $Fr = 28.06(\chi = 0.13)$ and $Fr = 29.69(\chi = 0.15)$, which is 1068 and 1100rpm respectively. Semena's expression predicts complete annular flow at much higher rotational speeds, 1360 and 1450rpm. Baker's expression seems to have predicted complete annular flow accurately.
For $\chi = 0.15$, the found resistance is $R * \mathrm{dz} = 0.050\mathrm{Km/W}$. This corresponds to a liquid layer thickness of 0.0006m for pure conduction, according to Equation 2.12. The liquid layer thickness associated to χ is $\delta = \overline{\delta} = 0.0017\mathrm{m}$. This discrepancy could be explained by turbulent mixing enhancing heat transfer again.

4.7. Conclusion

The aim of this chapter was to answer research questions regarding the performance of Dowtherm A as a working fluid of a rotating heat pipe in terms of heat transfer efficiency and to research the effect of rotational speed, temperature and power on heat transfer. The heat pipe of this experimental study successfully operated and the maximum power was estimated to be in between 280 and 480W. This study focused on internal heat transfer phenomena at temperatures above 250°C and below the rotational speed at which dry-out occurred. Dry-out was seen around Froude numbers where the onset of annular flow is expected and it drastically disturbed heat pipe operation and controllability. It is considered an effect of the eccentricity. The following can be concluded for the non-annular flow regime. The measured axial temperature difference in the vapor space between evaporator and adiabatic side of the condenser was 1.7 ± 2.2°C and the axial resistance is two orders smaller than conduction through the wall, which has a similar cross-sectional area. This shows that the heat pipe is working. The axial vapor temperature gradient measured more to the condenser end of heat pipe was larger and likely due to non-condensable gas. The condenser

showed signs of efficient heat transfer by turbulent mixing through the film at high rotational speeds(700-750rpm), which is not widely reported in literature. It matches the predicted heat transfer coefficient of turbulent mixing in the film within 10%. The found heat transfer coefficient through the film at those rotational speeds is $h = 1747\mathrm{W/m^2K} \pm 15\%$. No conclusion can be made for the condenser at lower rotational speeds due to the likely effects of non-condensable gas. It seems clear that nucleate boiling causes efficient heat transfer in the evaporator causing low resistance compared to the condenser. The heat transfer resistance showed a minor decrease with an increase in temperature, rotational speed and heat flux rate. The heat transfer coefficient of boiling at the film typically is $h = 4200\mathrm{W/m^2K} \pm 15\%$. The thickening of the liquid film with rotational speed did not lead to a noticeable increase of its resistance. Baker's expression seems to predict complete annular flow well, as signs of annular flow were seen at rotational speeds within 3% of the correlation. The resistance of heat transfer through the film in the condenser increased by 5 times when entering annular flow, while the evaporator showed little dependence.
The upper half of the operating temperatures of the intended use of heat pipes with Dowtherm A in a heat pipe assisted annealing line have been tested. Furthermore, the same axial heat fluxes as noted in Table 1.1 were reached during conducted experiments. 60% of the radial heat flux through the film in the condenser was reached, while in the evaporator heat fluxes of 95% the heat fluxes as in the application were reached. The expected film thickness scales with $\sqrt{r_{wi}}$, while radial heat transfer area scales with r_{wi}, according to Equation 2.9. This may cause local dry-out when too little liquid is dragged upwards with the wall for the vaporization rate, as described by Equation 4.23. For a filling ratio of $\chi = 0.14$, onset of annular flow is expected at 220rpm($Fr = 15.0$) and complete annular flow at 305rpm($Fr = 28.9$) at a full scale heat pipe.

5

Modelling of Non-Condensable Gas

The presence of non-condensable gas greatly influences the working of a heat pipe condenser, therefore understanding the effects is key in the internal analysis of heat pipes with non-condensable gas. A steady-state model has been developed which shows the quantitative and qualitative effects of non-condensable gas. Existing models, as described in Section 2.2, have been taken into account.

As pointed out in Section 1.4, the accumulation of non-condensable gas at the condenser end is caused by the convective flow from evaporator to condenser. Due to the high non-condensable gas concentration at the condenser end and a lower concentration at the adiabatic side, a concentration gradient exists. This gradient causes a diffusive transport of non-condensable gas in the opposite direction as the convective flow.
This diffusive transport causes a region of coexistence instead of a sharp front with condensable at one and non-condensable gas on the other side. The region of coexistence can be characterized by the distribution of non-condensable gas, shown by the profile of mole fraction x_g in axial direction at the condenser. As the condensable and non-condensable fractions are directly related by definition ($x_v = 1 - x_g$), the profile of non-condensable gas also gives the partial pressure p_v profile in the condenser at equilibrium according to Raoult's law for the vapor pressure in an ideal mixture. The vapor pressure in turn is related to the temperature at which condensation occurs, T_{sat}, which is the equilibrium temperature for a certain mole fraction.

This chapter describes the model developed to predict the influence of non-condensable gas in the condenser of the rotating heat pipe setup of TU Delft. The effects of amount of gas, temperature, power and rotational speed are shown. For application of rotating heat pipes in a future innovative annealing line of a steel factory, the size of the blocked heat pipe section in terms of heat transfer rate and temperature is of main relevance.

5.1. Type of Model

The model is based on equilibrium conditions inside the heat pipe and therefore gives a stationary solution of the non-condensable gas distribution in the condenser with the associated saturation temperature. From the heat transfer to the sink, the local condensation rate is determined, which gives information about the condensable flow inside the heat pipe.
Furthermore, the model is in 1D, in the axial direction. An additional model for the wall temperature is used to iteratively provide the model for the non-condensable gas distribution with the corresponding wall temperature profile.

The radially outward flow of condensable vapor to the condenser wall is known to cause a gradient of non-condensable gas concentration in radial direction[21, 39]. The extent of this effect depends on several system characteristics. For simplicity reasons, the model is kept

in 1D. The disability to take this effect into account should however be kept in mind when analysing the results.
Peterson published a dimensionless parametric study for the non-condensable gas distribution in a heat pipe, more specifically in a vertical thermosyphon with a wick. The difference of a flat front, a 1D and a 2D model in terms of the shut off length for condensation is shown for different parametric values and a parametric analysis on the radial distribution of non-condensable gas is presented. The study is based on two parameters:[39]

$$E = \frac{c_e M_v D h_{fg}}{h(T_e - T_c) r_v} \qquad \text{(Diffusion parameter)}$$

$$W = \frac{C}{2\pi r_v^3 h} \qquad \text{(Wall conduction parameter)}$$

Low values of E and W bring along large 2D-effects, according to the study of Peterson. E is a measure of diffusion versus heat transfer rate outwards. W is a measure of axial wall conductance versus heat transfer rate outwards. A rough calculation for E and W of the TU Delft setup for two cases in Table 5.1 shows if 2D-effects are likely. The values shown are obtained from experimental data.

Table 5.1: Values for parametric study Peterson

	Variable	TU Delft (300°C)	TU Delft (350°C)	Unit
c_e	= molar density in evaporator	0.055	0.123	$[kmol/m^3]$
M_v	= molecular weight condensable	166	166	$[kg/kmol]$
D	= mass diffusivity coefficient	$7.93 * 10^{-6}$	$3.99 * 10^{-6}$	$[m^2/s]$
h_{fg}	= latent heat of vaporization	$274.2 * 10^3$	$244.0 * 10^3$	$[J/kg]$
h	= heat transfer coefficient from liquid -vapor interface to sink condenser	50	33 (lower power)	$[W/m^2K]$
T_e	= temperature evaporator	573	623	$[K]$
T_c	= temperature sink condenser	303	303	$[K]$
r_v	= radius of vapor space	0.022	0.022	$[m]$
C	= sum of axial conductivity-area products $\sum k_j A_j$	0.0213	0.0213	$[Wm/K]$
E		0.067	0.086	
W		6.4	9.6	

The heat transfer coefficient includes a liquid layer, the wall and both convection and radiation at the outside wall. It is converged to a single value of h, such that $Q_{out} = 2\pi r_{wi} \Delta z h (T_i - T_c)$ holds for the part upstream of the front.
A comparison can be made between the non-condensable gas distribution in the vapor space of a vertical thermosyphon and a horizontal rotating heat pipe, as the flow in the vapor space is essentially the same and:

- The effect of gravity on the non-condensable gas distribution is negligible;
- The effect of rotation on the gasses is limited in the non-annular flow regime, as described in 4.3.1;
- The parameters are adjusted to be applied to a liquid layer instead of a wick.

Peterson concluded that 2D-effects become important when Wall conduction parameter W is less than 10 and Diffusion parameter E is less than 1. He presented the severity of 2D-effects of cases with different values of E and W. To conclude from the values in Table 5.1 and the findings of Peterson, the TU Delft setup is likely to have a 2D distribution of non-condensable gas, but it is not severe. The expected concentration difference between $r = 0$ and $r = r_v$ is expected to be in the order of 0.01. The associated temperature difference is in the order of 1°C

To summarize, the goal of the model presented in this chapter is to calculate the non-condensable gas distribution in the condenser and the associated temperature profile in the vapor space and wall. Also to obtain the flow of condensable vapor. This is done by a 1D-model of the vapor space of the condenser, with the addition of a separate model for the wall temperature, to iteratively get to the solution. The magnitude of 2D effects is estimated and can subsequently be used for the analysis of the results where a 1D distribution was assumed.

5.2. Working principle model: Vapor space

The basis of this model originates from a 1D study of heat and mass transfer in the vicinity of the non-condensable gas front in a heat pipe by Edwards and Marcus[16]. This study has some shortcomings, especially because the TU Delft setup has relatively thick walls. Furthermore, the model by Edwards and Marcus is made for non-rotating wicked heat pipes.

The used coordinate system and variables characterizing the vapor flow, the size and liquid layer thickness of the heat pipe are shown in Figure 5.1. According to this coordinate system, the convective flow is in the negative z-direction.

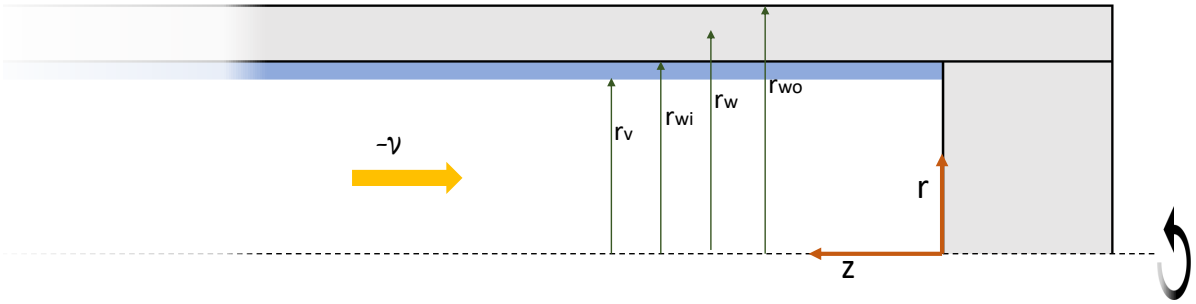

Figure 5.1: Coordinate system, velocity direction and size variables of condenser

5.2.1. Governing of equations

The equations used describe the axial transport of non-condensable gas, condensation rate and heat flows in and out of a wall element.

Non-condensable gas transport

$$-cD\frac{\mathrm{d}x_{g_s}}{\mathrm{d}z} + cvx_{g_b} = 0 \tag{5.1}$$

Equation 5.1 describes the stationary transport of non-condensable gas per unit area cross section. The first term is the diffusive transport due to the axial concentration gradient by Fick's law of diffusion, where D is the binary diffusion coefficient of a mixture of vapor and gas. The second term is the transport of non-condensable gas by the bulk convective flow. Velocity v is the mole average velocity. As the distribution is stationary and no net flow of non-condensable gas is present, the sum is zero. The change of condensable flow, $\mathrm{d}\dot{m}/\mathrm{d}z$, and non-condensable gas distribution are qualitatively visualized in Figure 5.2.
x_{g_s} is the spatial/area weighted average mole fraction, whereas x_{g_b} is a bulk property, area-velocity-weighted average. In this 1D model, these values are assumed to be equal. Equation 5.1 becomes $-cD\mathrm{d}x_g/\mathrm{d}z + cvx_g = 0$, the subscripts drop out. Downstream of the front, where radial flow is very low, this 1D assumption has little effect. At other sections, where radial flow is significant, this assumption can bring along inaccuracies. These inaccuracies will be estimated with the study of Peterson.

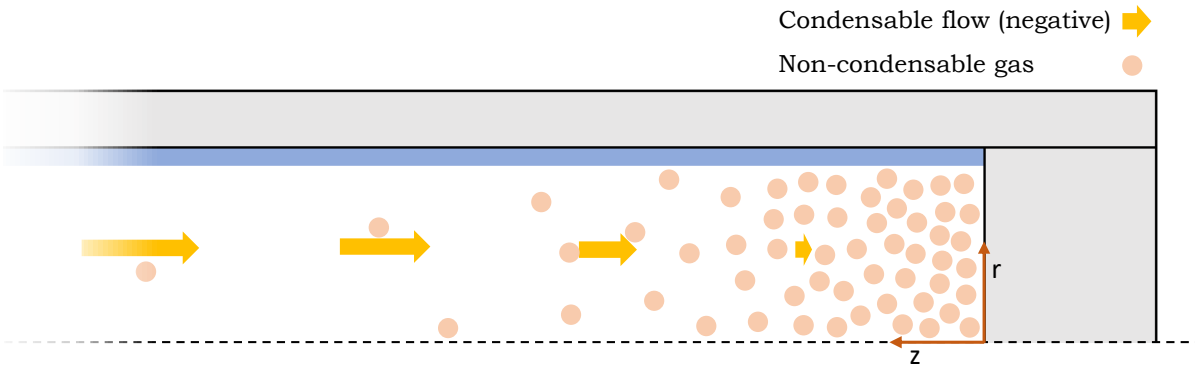

Figure 5.2: Non-condensable gas distribution due to convective and diffusive transport

Condensation rate

Next, the heat flow through liquid layer and wall due to the radial temperature gradient is calculated. This heat flow, coming from condensation of the working fluid, gives the condensation rate, which in turn can be used to calculate the condensable flow.

$$Q_{cond} = \frac{2\pi \mathrm{d}z}{\frac{ln\left(\frac{r_{wi}}{r_v}\right)}{\xi k_l} + \frac{ln\left(\frac{r_w}{r_{wi}}\right)}{k_w}} (T_v - T_w) \tag{5.2}$$

Variable K is introduced, such that:

$$Q_{cond} = K \mathrm{d}z (T_v - T_w) \tag{5.3}$$

,where

$$K = \frac{2\pi}{\frac{ln\left(\frac{r_{wi}}{r_v}\right)}{\xi k_l} + \frac{ln\left(\frac{r_w}{r_{wi}}\right)}{k_w}}$$

The condensation rate per unit length is represented by the change in axial mass flow of condensable vapor $\dot{m}$. From the working principle of a heat pipe, we know that the condensable vapor flow is 0 @ z=0 and reaches its absolute maximum at the evaporator end of the condenser, or at the adiabatic section in case of an adiabatic section with heat losses. As the convective flow is in negative z-direction, $\dot{m}$ is negative.

$$\frac{\mathrm{d}\dot{m}}{\mathrm{d}z} = -\frac{Q_{cond}/\mathrm{d}z}{h_{fg}} \tag{5.4}$$

Heat balance wall element

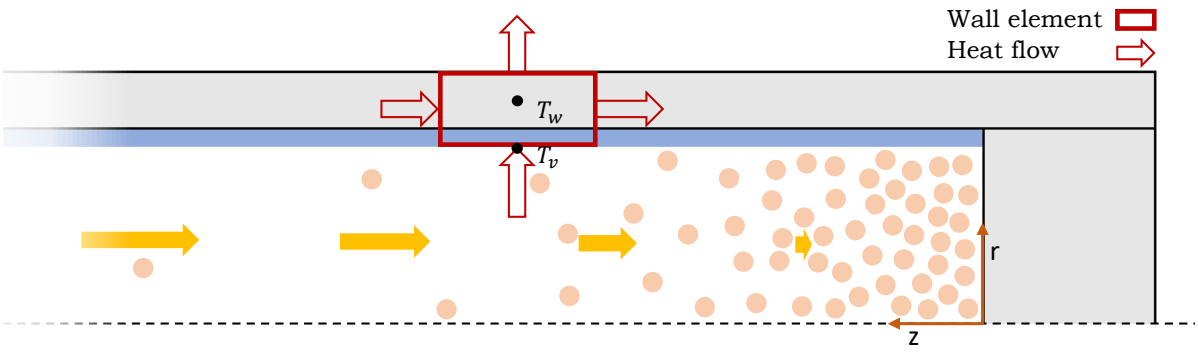

Figure 5.3: Heat balance of a wall element

The wall is an important part of this study, as the determining heat flows go through it. The heat flows in and out of a stationary wall element including liquid layer are shown in Figure 5.3. The heat balance of a stationary element with length dz is given by Equation 5.5.

$$C\frac{\mathrm{d}^2T_w}{\mathrm{d}z^2} + K(T_v - T_w) - Q_{out}/\mathrm{d}z = 0 \tag{5.5}$$

,where C is the conductivity-area product of the condenser cross section, which comprises out of conduction through wall and liquid layer. The first term is the net axial heat inflow of a wall element of length dz, the second term the radial inflow of heat of condensation through liquid to wall center and the third term is the outflow of heat from the middle of the wall to surroundings by forced convection and radiation. The share of the wall on C is dominant, so the second derivative of the middle of the wall temperature, T_w, is taken as the driver for axial heat flow through the wall.

$$C = k_w\pi(r_{wo}^2 - r_{wi}^2) + k_l\pi(r_{wi}^2 - r_v^2) \tag{5.6}$$

For the heat transfer out, $Q_{out}/\mathrm{d}z$, the equations for radiation and forced convection from Section 4.2.2 are used. These have been compared with the TU Delft setup experimental data. Above wall temperatures of 500K, the heat transfer out matches the experimental data within 20%. Below 500K, an underestimation of the heat transfer out can be expected. Equation 4.16 gives the heat transfer out. The quantities from Table 4.2 are used.

$$Q_{out}/\mathrm{d}z = Q_c/\mathrm{d}z + Q_r/\mathrm{d}z = \frac{\epsilon_{wo}2\pi r_{wo}}{1 + \frac{\epsilon_{wo}A_{wo}}{\epsilon_{duct}A_{duct}}(1-\epsilon_{duct})}\sigma\left(T_{wo}^4 - T_{duct}^4\right) + 2\pi r_{wo}h_c(T_{wo} - T_{air}) \tag{5.7}$$

For this 1D study, without the integration of wall, the wall temperature is considered to closely follow the temperature inside the heat pipe. In the case that this holds, the following assumption can be made:

$$\frac{\mathrm{d}T_w^2}{\mathrm{d}z^2} = \frac{\mathrm{d}T_v^2}{\mathrm{d}z^2} \tag{5.8}$$

Equation 5.5 changes to:

$$C\frac{\mathrm{d}^2T_v}{\mathrm{d}z^2} + K(T_v - T_w) - Q_{out}/\mathrm{d}z = 0 \tag{5.9}$$

The validity of this assumption requires a thorough analysis of the wall temperature. Especially with thick walled heat pipes, this assumption does not hold and requires the addition of a wall temperature calculation to the model. It is a major shortcoming of 1D models. The addition of wall calculations is described in Section 5.3 and the effect is shown in Section 5.5.2, where also a characteristic number is presented at which this wall calculation addition is necessary in showing the effect of non-condensable gas.

Temperature and mole fraction relation

Empirical data for the vapor pressure at a certain temperature has been used in the analysis of the experimental data. Two alternatives are the theoretical Clausius-Clapeyron relation and the empirical Antoine equation for vapor pressure. These are however considered less accurate compared to the empirical data for Dowtherm A.
For the analytical term $\mathrm{d}^2T_v/\mathrm{d}z^2$, an expression of x_v as a function of T_v is needed. As the aim is to describe the influence of the gas using physical analytical equations, the Clausius-Clapeyron relation is used. This also allows the model to be used for other working fluids. The Clausius-Clapeyron relation defines the vapor pressure curve as[51]:

$$\frac{\mathrm{d}p}{\mathrm{d}T} = \frac{h_{fg}}{T(\upsilon_v - \upsilon_l)} \tag{5.10}$$

where the specific volume of liquid is a lot smaller than that of the vapor and where the vapor is assumed to behave like an ideal gas:

$$\upsilon_l \ll \upsilon_v = \frac{RT}{p} \tag{5.11}$$

Equation 5.10 can be rewritten and integrated to:

$$\frac{\mathrm{d}p}{\mathrm{d}T} \approx \frac{h_{fg}p}{RT^2} \tag{5.12}$$

$$ln(p) = -\frac{h_{fg}}{RT} + ln(C_{int}) \tag{5.13}$$

As discussed in Section 2.2, Raoult's law can be used to relate the partial pressure of condensable p_v to the mole fraction x_v. The Clausius-Clapeyron derived equation can then be used to relate T_v to x_v, to be used for an analytic expression of $\mathrm{d}^2T_v/\mathrm{d}z^2$.

$$x_v = \frac{p_v}{p} \tag{5.14}$$

$$ln(x_v) = -\frac{h_{fg}}{R}\left(\frac{1}{T_v} - \frac{1}{T_{ev}}\right) \tag{5.15}$$

where p is the pressure in the heat pipe, which is assumed to be constant.
The ideal gas law and Clausius-Clapeyron relation were used to get to this expression. Inaccuracy can be expected at high pressure and low temperature, as molecule interaction makes a gas behave less like an ideal gas, causing a value of compressibility factor Z to be far from 1.

5.2.2. Model differential equations

The governing equations discussed in previous section are reduced to two first order differential equations for condensable flow $\dot{m}$ and non-condensable mole fraction x_g. The full derivation of these two differential equations can be evaluated in Appendix I.

To mathematically ease the derivation of the two differential equations, the dependent variable x_g is transformed to another domain and named ϕ, according to:

$$\phi = ln\left(\frac{1}{x_g}\right), \qquad x_g = e^{-\phi} \tag{5.16}$$

Gradient gas fraction

The following expression of the condensable flow rate $\dot{m}$ can be inserted in Equation 5.1, which after transformation becomes:

$$\dot{m} = cvA_vM_v \tag{5.17}$$

,where v is the mole average velocity.

$$cA_vM_vD\frac{\mathrm{d}\phi}{\mathrm{d}z} + \dot{m} = 0 \tag{5.18}$$

This directly results in the first equation of the model:

$$\boxed{\frac{\mathrm{d}\phi}{\mathrm{d}z} = -\frac{\dot{m}}{cA_vM_vD}} \tag{5.19}$$

This differential equation of the gradient of the transformed gas fraction is based on stationary non-condensable gas distribution and therefore no net transport of the gas molecules. It is a function of local condensable flow, molar concentration, cross sectional area of the vapor space and the diffusion coefficient. A relatively large convective flow results in a high gradient, whereas a high diffusion coefficient yields a low gradient. Remember that $x_g = e^{-\phi}$, at low ϕ the gradient affects x_g(high) the most due to the negative exponential.

Gradient condensable mass flow

If we get back to the working principle of a heat pipe, we know that the condensable vapor flow is zero at condenser end and reaches its maximum value at the evaporator side. The flow gradually increases. The condensation rate is a measure for this increase, as it is the only sink of the condensable vapor. The following method is used to obtain an expression for $\mathrm{d}\dot{m}/\mathrm{d}z$.

From Equation 5.3 and 5.4 follows:

$$K(T_v - T_w) = -\frac{\mathrm{d}\dot{m}}{\mathrm{d}z} h_{fg} \tag{5.20}$$

which can be inserted in the heat balance of a wall element, Equation 5.9:

$$C\frac{\mathrm{d}^2 T_v}{\mathrm{d}z^2} - \frac{\mathrm{d}\dot{m}}{\mathrm{d}z} h_{fg} - Q_{out}/\mathrm{d}z = 0 \tag{5.21}$$

It can be seen that under assumption in Equation 5.8 and this insertion, the wall temperature has been eliminated, provided that Q_{out} is provided as a function of T_v and not of T_w.

Next, an analytic expression of $\mathrm{d}^2T_v/\mathrm{d}z^2$ is made by derivation of transformed Equation 5.15 with respect to z.

$$e^{-\phi} = 1 - x_v = 1 - e^{-\frac{T_0}{T_{ev}}\left(\frac{T_{ev}}{T_v} - 1\right)} \tag{5.22}$$

where

$$T_0 = \frac{h_{fg}}{R}$$

$$\frac{\mathrm{d}e^{-\phi}}{\mathrm{d}z} = \frac{\mathrm{d}}{\mathrm{d}z}\left(1 - e^{-\frac{T_0}{T_{ev}}\left(\frac{T_{ev}}{T_v} - 1\right)}\right) \tag{5.23}$$

$$\frac{\mathrm{d}T_v}{\mathrm{d}z} = \frac{\mathrm{d}\phi}{\mathrm{d}z}\frac{T_v^2}{T_0}\frac{e^{-\phi}}{1 - e^{-\phi}} = -\frac{\dot{m}}{cA_v M_v D}\frac{T_v^2}{T_0}\frac{e^{-\phi}}{1 - e^{-\phi}} \tag{5.24}$$

$$\frac{\mathrm{d}^2T_v}{\mathrm{d}z^2} = -\frac{1}{cA_v M_v D}\frac{T_v^2}{T_0}\frac{e^{-\phi}}{1 - e^{-\phi}}\frac{\mathrm{d}\dot{m}}{\mathrm{d}z} + \left(\frac{\dot{m}}{cA_v M_v D}\right)^2 \frac{T_v^2}{T_0}\left(2\frac{T_v}{T_0}\frac{e^{-2\phi}}{(1 - e^{-\phi})^2} - \frac{e^{-\phi}}{(1 - e^{-\phi})^2}\right) \tag{5.25}$$

Equation 5.21 and 5.25 can be combined to form an expressions for $\frac{\mathrm{d}\dot{m}}{\mathrm{d}z}$

$$\frac{\mathrm{d}\dot{m}}{\mathrm{d}z} = \frac{C\frac{\mathrm{d}^2T_v}{\mathrm{d}z^2} - Q_{out}/\mathrm{d}z}{h_{fg}} \tag{5.26}$$

$$\boxed{\frac{\mathrm{d}\dot{m}}{\mathrm{d}z} = \frac{C\left(\frac{\dot{m}}{cA_v M_v D}\right)^2 \frac{T_v^2}{T_0}\left(2\frac{T_v}{T_0}\frac{e^{-2\phi}}{(1-e^{-\phi})^2} - \frac{e^{-\phi}}{(1-e^{-\phi})^2}\right) - Q_{out}/\mathrm{d}z}{C\frac{1}{cA_v M_v D}\frac{T_v^2}{T_0}\frac{e^{-\phi}}{1-e^{-\phi}} + h_{fg}}} \tag{5.27}$$

Equations 5.19 and 5.27 form the basis of the model. The first is based on the stationary transport of non-condensable gas and the latter is based on the heat balance of a wall element. The Clausius-Clapeyron relation is used for the expression of $\mathrm{d}^2T_v/\mathrm{d}z^2$.

5.2.3. Boundary conditions

Now we have the equations to be solved by the model, the boundary conditions can be set up. As the two equations are of first order, two boundary conditions are required to get to a solution. They are of the Dirichlet boundary condition type.

BC's @ $z = 0$:

$$\dot{m}\Big|_{@\ z=0} = 0 \tag{5.28a}$$

$$\phi\Big|_{@\ z=0} = \phi_0 \tag{5.28b}$$

The first boundary condition directly follows from the working principle of the heat pipe, as earlier discussed. As the wall is supposed to be the only sink of condensable vapor in the condenser, the mass flow is zero at $z = 0$.
The second boundary condition prescribes the mole fraction of gas at the condenser end. This is a guess at first and gives a solution with a certain amount of non-condensable gas in the heat pipe, which is unknown on forehand. Iteratively this value of ϕ_0 is changed, as described in Section 5.2.5.

5.2.4. Assumptions

1. The radial concentration gradient is negligible: $\frac{\mathrm{d}x_g}{\mathrm{d}r} \approx 0$.
2. The energy of subcooling of liquid and superheated vapor is considered negligible compared to the energy of condensation.
3. Radial transport of condensable vapor is not limiting the condensation rate.
4. The supply of vapor by the evaporator is sufficiently large to not limit the condensation rate.
5. Condensation only takes place at the vapor-liquid interface at the wall, not at the condenser end side or away from the interface.
6. Pressure drop due to flow losses is considered to be small and not causing a temperature drop in the vapor space.
7. The second derivative of the wall temperature is equal to that of the vapor temperature: $\frac{\mathrm{d}^2T_w}{\mathrm{d}z^2} = \frac{\mathrm{d}^2T_v}{\mathrm{d}z^2}$
8. The Clausius-Clapeyron relation accurately gives an expression for $\frac{\mathrm{d}^2T_v}{\mathrm{d}z^2}$.
9. The heat transfer out, Q_{out} can be expressed as a function of T_v and v_{fan}.

The last three assumptions will fall out if the wall model of Section 5.3 is used. These assumptions will then only be used to get an initial solution for the iteration process.

5.2.5. Solver of vapor space model

Since the differential equations and boundary conditions are now set up, the part left is solving them. The equations are ordinary non-linear differential equations of ϕ and $\dot{m}$ and the boundary conditions are imposed at one side. Very low values of ϕ and $\dot{m}$ are expected at low z. At the downstream side of the front, $\mathrm{d}\dot{m}/\mathrm{d}z$ starts to increase(more negative) and gets to a stable value upstream of the front. As $\dot{m}$ gets more negative with an increase in z, $\mathrm{d}\phi/\mathrm{d}z$ increases, which causes an exponential growth of ϕ from just downstream of the front till the end at $z = L_{condenser}$.
Special attention should be paid to the section at the upstream side of the front. In this section, T_v increases rapidly followed by it getting stable at the value T_{ev}. Therefore, $\mathrm{d}^2T_v/\mathrm{d}z^2$ is very negative in this section and so $\mathrm{d}^2T_w/\mathrm{d}z^2$ will be very negative as well. From the heat balance derived Equation 5.26, we can conclude that this causes a large negative $\mathrm{d}\dot{m}/\mathrm{d}z$.
To conclude, a suitable solver should be used to deal with a locally large $\mathrm{d}\dot{m}/\mathrm{d}z$ at the upstream side of the front, a large $\mathrm{d}\phi/\mathrm{d}z$ at high z and very low values of ϕ and $\dot{m}$ at low z. As we are interested in x_g and not in transformation variable ϕ after all, inaccuracy of ϕ at large ϕ is not of concern, because it is not affecting x_g at large ϕ ($x_g = e^{-\phi}$), provided this inaccuracy does not affect the rest of the solution.

Computational method

A suitable solver for this problem is the boundary value problem bvp4c solver of Matlab. It uses the implicit Lobatto IIIA fourth order accuracy collocation method, which can be called part of the Runge-Kutta family of solving methods. An implicit solver is chosen for stability reasons, as the solver has to deal with high and quickly changing gradients. Furthermore, it is characterized by its limited damping of extremes. Damping could lead to inaccuracy of the expected local peak of $d\dot{m}/dz$, due to the damping out of the peak. However, a fine mesh here is probably required to get stability. The computational cost of the implicit method is chosen to be of less importance at this time, as the model is only in 1D and for a stationary solution. One of the advantages of the bvp4c solver of Matlab is the ability to deal with poor guesses. As the exact location of the front is unknown on forehand, it is extremely hard to make a good guess, so this ability comes in handy. The Lobatto IIIA is considered to be accurate for stiff equations demonstrated by multiple studies. Due to the accuracy and the favorable stability characteristics, the bvp4c is chosen as the solver.[23, 40]

Model setup

Due to the fact that the boundary conditions are both imposed at the same side, the problem actually is an initial value problem. Matlab's boundary value problem solver bvp4c treats a case with boundary conditions at one boundary the same way as common initial value problem solvers, so the bvp4c solver is suitable for our case, although we have an initial value problem.[23]

The condenser is split into small sections of 0.001m, which are solved individually one after the other. The section at $z = 0$ is solved first, using the boundary conditions given by Equations 5.28. The final values of ϕ and $\dot{m}$ at the other side of the current section are used as boundary conditions of the following section, until $z = L_{condenser}$ is reached. The individually solving with the passing on of the end values at one side to the next section is possible, because the boundary values are set at one side only and the gradients $d\phi/dz$ and $d\dot{m}/dz$ are a function of local values only and do not depend on gradients of neighbouring nodes.
The splitting up is done to ease the solving and to get more insight in the solving process. The mesh can be defined differently for each section, based on the expected local stiffness of the equations. When no convergence is reached in a section, the solution of previous sections can still be analysed to visualise the problem. Furthermore, the error in small sections can be controlled better compared to a single large section. Each section is allowed to reach its maximum tolerated error, which can be individually controlled. However, care must be taken to set the error tolerance such that accurate values of ϕ and $\dot{m}$ are passed to the next section, such that the building up of the error passed on is not affecting the rest of the solution. Also, a guess method can be used which does not require knowledge about the front location.

As already mentioned, it is hard to make a good guess for the solver, as the location and shape of the front are unknown. A different guess method is used for the initial run of the vapor space model compared to during the iteration.
For the initial run, the guess of each small section is equal to the given value at the low z side of the section. A constant value is guessed, but due to the small size of the section, it is not far off the solution.
During the iteration with the wall temperature model, the values of ϕ and $\dot{m}$ of the previous solution of the vapor space model are used as a guess. With this guess method, the necessity of the use of small sections partly disappears.

Mesh

The bvp4c solver of Matlab tries to get to a solution complying with the error tolerance by using a small amount of mesh points. The maximum amount of points to be used can be set individually for each small section of the condenser. This is set to 1000 points/mm for $x_g > 0.01$ and 100 points/mm for the remaining section. The determination of the mesh size is explained in Appendix J.

Iteration non-condensable gas

The solver finds a solution associated with $\phi = \phi_0$ at $z = 0$. The mole fraction of non-condensable gas is set at the condenser end of the heat pipe. A change of this boundary conditions results in a shift of the front. Lowering ϕ_0 moves the front upstream and thus results in a solution with a higher amount of non-condensable gas. The amount of non-condensable gas is defined as:

$$m_g = \rho_g A_v \int_0^{L_{condenser}} x_g \mathrm{d}z \tag{5.29}$$

For the initial run of the vapor space model, ϕ_0 is iteratively changed until a solution is found with the right amount of non-condensable gas. The acceptable error of this amount can be changed according to the application and will be given in Section 5.5.1 for the model runs in this study.
During the iteration of the vapor space model and the wall temperature model, this method of finding a solution with the right amount of non-condensable gas is not applied. Instead, the solution is just shifted to a position with the right amount of gas. This can be done if the values of ϕ and $\dot{m}$ are constant at the condenser end of the heat pipe and if this shift is only small. This shifting instead of iterating decreases the computational time needed. As the integration of the wall causes only a minor change in front location, this shift is indeed small. During the iteration with the wall, ϕ_0 is taken as the value of ϕ at $z = 0$ of the previous shifted solution. Boundary condition 5.28b during iteration with the wall model is:

$$\phi\big|_{@\ z=0,\ n} = \phi_{0,\ n} = \phi(0)_{n-1}$$

The amount of non-condensable gas and total heat rejection of the condenser are related, as the influenced part of the condenser is dependent on the non-condensable gas amount. The vapor space model iteration can be changed in order to find a solution with the desired heat rejection of the condenser. A decrease of ϕ_0 results in the front to move upstream, which causes a lower total heat rejection of the condenser. If desired, the iteration can be changed such that a solution is found for a certain heat rejection instead of amount of non-condensable gas.

5.3. Working principle model: Wall temperature

The main model equations are derived using some questionable assumptions to make the study a 1D case. As a recap, the main model outputs the profile of mole fraction x_g and the profile of condensable flow $\dot{m}$. The temperature inside is obtained by relating the mole fraction x_v to the saturation temperature using Raoult's law. By detailed study of the model results, the necessity of the integration of a wall model can be analysed. For this analysis, values for $\mathrm{d}^2T_w/\mathrm{d}z^2$ are obtained for the condenser and compared to the values of $\mathrm{d}^2T_v/\mathrm{d}z^2$ used by the main model. To make this comparison and potential integration, a wall temperature model has been devised.

5.3.1. Model differential equation

For this wall model, a heat balance of a wall element is set up again. This time, the balance is used to determine the wall temperature instead of the condensation rate. The input of the wall model is the vapor temperature, which comes from the mole fraction of the main model. Equation 5.5 can be rewritten to:

$$\boxed{\frac{\mathrm{d}^2T_w}{\mathrm{d}z^2} = \frac{Q_{out}/\mathrm{d}z - K(T_v - T_w)}{C}} \tag{5.30}$$

This second temperature derivative in axial direction is needed to balance the heat flows in and out of a wall element. Q_{out} is a function of T_{wo}, sink temperatures and cooling air velocity v_{fan}. in this wall calculation and can be found in Equation 5.7.

5.3.2. Boundary conditions

The second order differential equation requires two boundary conditions. The first boundary condition is a result of the constant($\mathrm{d}/\mathrm{d}z = 0$) heat flux and temperature inside, T_v, upstream of the front as x_g becomes zero. In equilibrium, a constant T_v yields a constant T_w if the heat flux is constant as well.
The second boundary implies a constant T_w as well, but then at $-\infty$. As the gradient and temperature at $z = 0$ are unknown, the rotating heat pipe wall in the model is extended beyond $z = 0$ to apply the zero gradient wall temperature at the imaginary end. The location of this imaginary end is taken as $z = -4L_{condenser}$. Afterwards, it should be checked that $\mathrm{d}T_w/\mathrm{d}z \approx 0$ well away from the imaginary end. No condensation takes place in this imaginary part beyond the vapor space, so the heat balance is achieved by Q_{out} and the axial heat inflow. In common rotating heat pipe designs, the pipe will not end at the vapor space, as space is required for the mounting by means of bearings and for the connection to the motor for example. The heat outflow and the conductivity-area-product C is assumed to be equal in this negative z section as in the condenser. Another expression for C and Q_{out} could also be set in the model.
This results in the following two Neumann type boundary conditions, which are shown in Figure 5.4.

BC's:

$$\left.\frac{\mathrm{d}T_w}{\mathrm{d}z}\right|_{@\ z=L_{condenser}} = 0 \tag{5.31a}$$

$$\left.\frac{\mathrm{d}T_w}{\mathrm{d}z}\right|_{@\ z=-\infty} = 0 \tag{5.31b}$$

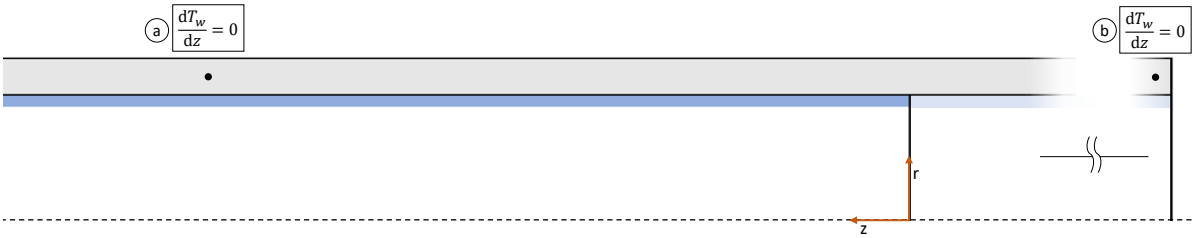

Figure 5.4: Boundary conditions of wall temperature model

5.3.3. Assumptions Wall model

The following additional assumptions need to be made for the wall model:

1. $Q_{out}/\mathrm{d}z(T_w)$ and C in the heat pipe part without vapor space ($z < 0$) is the same as in the part with condensation ($z > 0$).
2. Constant wall temperature at the condenser end: $\frac{\mathrm{d}T_w}{\mathrm{d}z} = 0\ @\ z = L_{condenser}$

5.3.4. Solver of wall temperature model

The term $K(T_v - T_w)$ gives the radial heat inflow between vapor-liquid interface and wall, as shown in Equation 5.30. The source of the heat inflow at r_v is the condensation of vapor. Vapor space temperature T_v comes from the 1D axial mole fraction profile of condensable vapor in the heat pipe, determined by the vapor space model.

Condensation limit

At low mole fractions of condensable vapor, the condensation can be limited by the transport of condensable vapor molecules to the vapor-liquid interface. For the vapor space model, it was assumed that the supply of vapor was not limiting condensation rate, which seems valid for the TU Delft experimental setup due to the expected negligible pressure drop, as

discussed in Section 4.3.1. The presence of non-condensable gas could however also limit the transport of vapor towards the vapor-liquid interface. When looking at this transport, one could analyse this by looking at an imaginary cell in the vapor space right at the vapor-liquid interface. Condensable vapor molecules leave this imaginary cell due to condensation. The same amount of molecules enter this cell by a convective inflow driven by a pressure difference. This entering flow consists partly out of non-condensable gas molecules in the region of coexistence. This means that a convective inflow alone yields a net transport out of condensable molecules. Equilibrium is reached by a diffusive inflow of condensable molecules, which means a negative radial concentration gradient $\partial x_v/\partial r < 0$ is present in equilibrium. A condensation rate therefore requires a certain diffusive rate and thus a radial concentration gradient. As T_v in condensation rate $K(T_v - T_w)$ is taken to be equal over a vapor space cross-section due to the 1D approach, this results in the assumption that radial diffusive transport is not limited, which does not hold in the region of coexistence. An expression is derived for the limit on condensation rate to prevent unrealistic condensation rates in the non-condensable gas area. This limit is applied to the axial region of the heat pipe where diffusive transport is significant and larger than convective transport:

$$\frac{-x_v v}{D\frac{\mathrm{d}x_v}{\mathrm{d}z}} < 1 \tag{5.32}$$

This limit expression is based on the diffusive transport in an outer annulus of a slice of the vapor space, as shown in Figure 5.5. For this, the net diffusive inflow of the annulus is defined equal to the condensation rate of vapor supplied by diffusion, which is $(1 - x_v)\mathrm{d}\dot{m}/\mathrm{d}z$ as discussed above:

$$-(1 - x_v)\frac{\mathrm{d}\dot{m}}{\mathrm{d}z} = cDM\pi(r_v^2 - r_x^2)\frac{\partial^2 x_v}{\partial z^2} = -cDM2\pi r_v \frac{\partial x_v}{\partial r}\bigg|_{r=r_v} \tag{5.33}$$

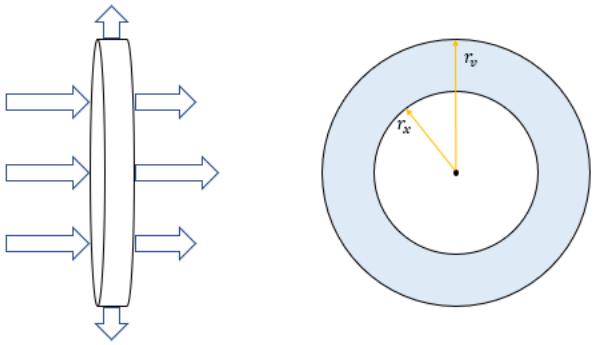

Figure 5.5: Left: A slice of the vapor space of the heat pipe. Arrows indicate condensable vapor transport. Right: Cross-section of the vapor space, showing outer annulus(blue) in which radial diffusion takes place

$\mathrm{d}^2x_v/\mathrm{d}z^2$ is assumed equal over the cross-section for this approach. By integrating Equation 5.33 for the case where the limit is reached: $x_v = 0$ @ $r = r_v$, an expression for the radial profile of x_v is derived. By taking the average of x_v over the cross-sectional area of the vapor space, a limit for the condensation rate with 1D variables is acquired, a function of x_v and $\mathrm{d}^2x_v/\mathrm{d}z^2$, shown in Equation 5.34. This limit holds for the region where diffusion is the dominant heat transfer mechanism. The full derivation is shown in Appendix K.

$$\frac{\mathrm{d}\dot{m}}{\mathrm{d}z}\bigg|_{limit} = -\frac{\sqrt{8x_v\frac{\mathrm{d}^2x_v}{\mathrm{d}z^2}}\,\pi r_v cDM}{1 - x_v} \tag{5.34}$$

Furthermore, when $T_w > T_v$, the term $K(T_v - T_w)$ suggests an inflow of heat to the vapor space. As conduction through gas is considered to be negligible, this term suggests vaporization when $T_w > T_v$ in the condenser. As the pressure is nearly homogeneous in the heat

pipe, vaporization occurs at T_{ev} in the condenser as well. T_w can become higher than T_v due to axial heat flow in the front. In the front, T_v is lower than T_{ev}, which means no vaporization of liquid occurs in the condenser:

$$\frac{\mathrm{d}\dot{m}}{\mathrm{d}z} \leq 0 \tag{5.35}$$

Model setup

The wall temperature model uses the same solver as the vapor space model. A description of the Lobatto IIIA Matlab solver can be found in Section 5.2.5. The to be solved problem of the wall is less difficult, as the single component is less stiff compared to the components in the vapor space model, especially compared to $\mathrm{d}\dot{m}/\mathrm{d}z$. Furthermore, a guess of the solution is easier to make, as the location of the front is known from the vapor space model. Although the accuracy and stability of this fourth order accuracy method may not be needed, it is chosen for consistency and user-friendliness reasons. A mesh size which is not large limits the computational time.

The information of the vapor space model is valuable input for the guess of wall temperature model solution. The wall temperature profile will have a similar shape as the vapor temperature profile, especially for thin walled heat pipes, therefore the educated guess in Table 5.2 could be made.

Table 5.2: Guess for Wall Temperature model solution

	Guess	
	Initial	Iteration
$T_{w,i} =$	$T_v - \frac{Q_{cond}/\mathrm{d}z}{K}$	$T_{w,i-1}$
$\frac{\mathrm{d}T_w}{\mathrm{d}z}_i =$	$\frac{\mathrm{d}T_v}{\mathrm{d}z}$	$\frac{\mathrm{d}T_w}{\mathrm{d}z}_{i-1}$

5.4. Combined vapor space and wall temperature model

The solution of the non-condensable gas distribution gets more accurate by combining the vapor space and wall temperature model, as multiple assumptions fall out, which are not valid at all conditions. The wall model provides values for $T_w(z)$ and $\mathrm{d}^2T_w/\mathrm{d}z^2(z)$ as an input for the vapor space model. Instead of solving Equation 5.26, the original equation for the change in condensable flow can be solved. $Q_{out}/\mathrm{d}z$ is a function of T_w in Equation 5.36.

$$\boxed{\frac{\mathrm{d}\dot{m}}{\mathrm{d}z} = \frac{C\frac{\mathrm{d}^2T_w}{\mathrm{d}z^2} - Q_{out}/\mathrm{d}z}{h_{fg}}} \tag{5.36}$$

The two models are combined by iterating them. The results of the vapor space model are the input of wall temperature model and the other way around. This iteration process is illustrated by Figure 5.6.

5.5. Results

This section provides results of the model presented in this chapter. First, the general outcome and effect of the combined vapor space model is presented. Afterwards, the sensitivity of multiple parameters is shown. Furthermore, the validity of the developed model is presented and subsequently a comparison with obtained experimental data is given.

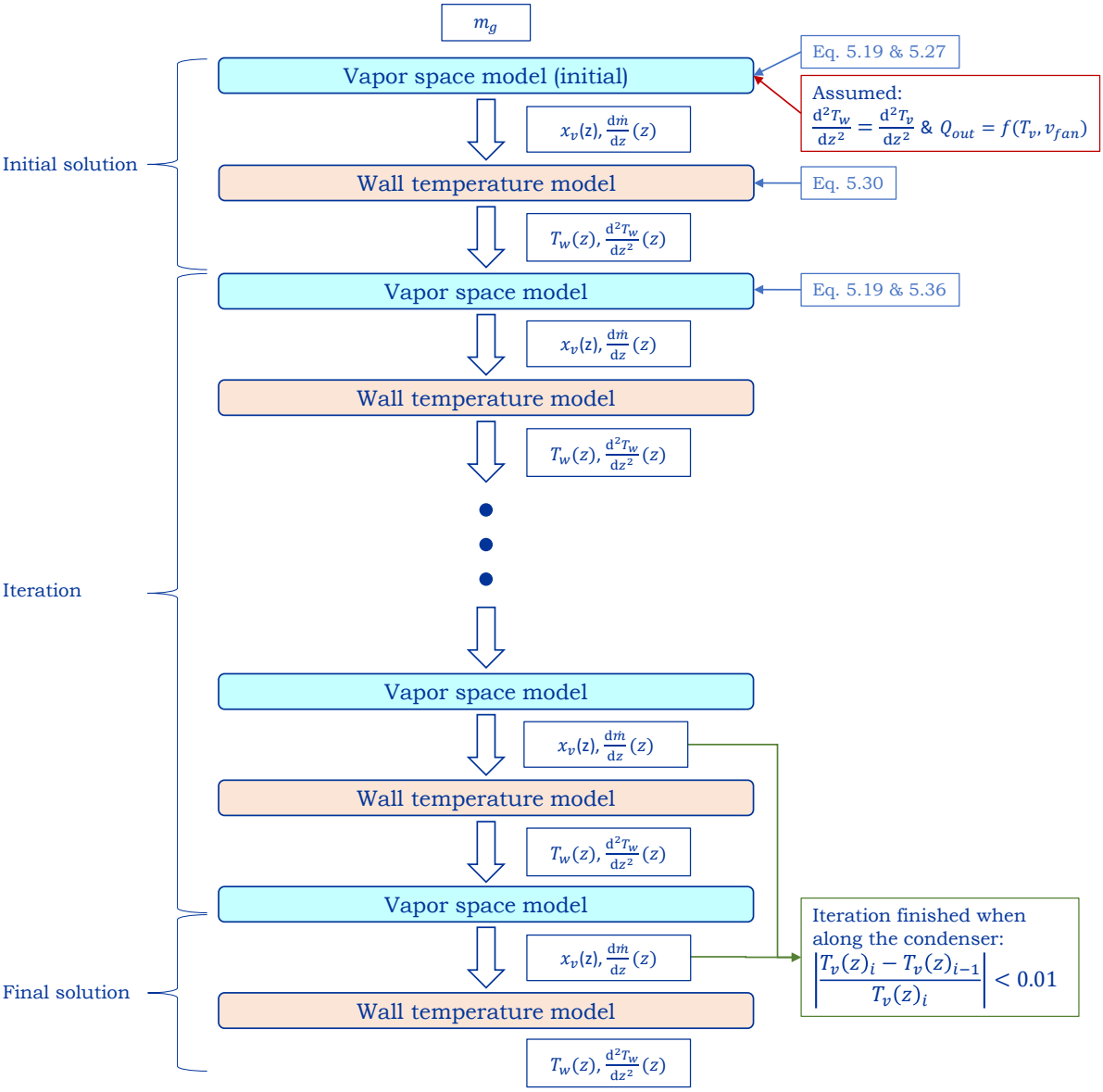

Figure 5.6: Combined model iteration process

5.5.1. Input variables

Table 5.3 provides the input variables required by the model. The values shown belong to the TU Delft experimental setup. One of the values which changes significantly with temperature is the non-condensable gas density ρ_g, due to the vapor pressure change. Material properties of Dowtherm A at saturation conditions are provided in Appendix F.

Figure 5.7 shows results of the model for the 300°C case. Both the initial vapor space result and the combined model result are shown. The effect of the wall integration is clearly visible. The concentration x_g gradient has increased at the upstream side of the front. Downstream of about $x_g = 0.55$, the line bends and the gradient decreases. This is the location from where the condensation limit is applied and results in a flattening of the front. This translates to a similar profile of T_v. Figure 5.7a also shows the associated wall temperature profile, which already decreases far left of the front. Figure 5.7b shows the associated mass flow and its gradient. Condensation rate $d\dot{m}/dz$ shows a large peak for the initial result, while after iterated this peak has flattened. The initial model assumes $d^2T_w/dz^2 = d^2T_v/dz^2$, which basically suggests that the wall temperature profile follows the vapor temperature closely, which is clearly not the case in this study, as the condensation rate profile has changed significantly

Table 5.3: Input variables of model. Values shown are applicable for TU Delft experimental setup with Dowtherm A as its working fluid

Variable		Note	Value 275°C	Value 300°C	Value 350°C	Error
k_w	[W/mK]	Eq. F.1	17.8	18.2	19.0	
C	[Wm/K]	Eq. 5.6	0.0233	0.0238	0.0248	
ρ_l	[kg/m^3]		833.4	806.8	748.6	
ρ_v	[kg/m^3]		5.74	9.07	20.43	
ρ_g	[kg/m^3]		0.949	1.445	3.007	
k_l	[W/mK]		0.098	0.094	0.086	
h_{fg}	[J/kg]		287422	274200	244000	
c	[kmol/m^3]	ρ_v/M_v	0.035	0.055	0.123	
D	[m^2/s]	Sec. F.0.4	$0.112 * 10^{-4}$	$0.076 * 10^{-4}$	$0.039 * 10^{-4}$	~4%[42]
M_v	[kg/kmol]		166			
Q_{out}/dz	$f(T_{wo}, v_{air})$		from Eq. 4.16 and Table 4.2			±25%
v_{fan}			from experimental setup			
m_g			from experimental setup			± ~ 0.3g
L_{cond}			0.195m			
r			$r_{wi} = 0.022$m		$r_{wo} = 0.030$m	

after wall integration. Furthermore, also a larger condensable mas flow $\dot{m}$ is presented after iteration. Apparently, more condensation happens in the vicinity of the front after iteration. The process of iteration can be seen in Figure L.1.

The condensation limit shows to affect the solution downstream of the front, which can be seen from the condensation rate downstream of the front in Figure 5.7b, where condensation rate at the iterated solution is lower than at the initial solution. As the limit is applied to the wall model, it is not included in the initial solution. The limit shows to yield a higher non-condensable gas fraction downstream of the front. Figure L.2 in the appendix shows the effect of wall thickness variation. A thin wall yields a less steep temperature gradient at the upstream side of the front, which is closer to the gradient of the initial solution. However, the condensation limit has resulted in the front to be upstream of the initial solution, while steepening alone causes the front to move downstream.

5.5.2. Sensitivity analysis

Figure 5.8a shows the effect of a change in diffusivity coefficient and in Q_{out}/dz. The effect of a 100% change in diffusivity coefficient is negligible, while the effect of heat outflow is clearly visible. A 25% change is equal to the expected error of the heat transfer outwards to the cooling duct. An increase in power steepens the front of vapor and non-condensable gas, which is expected due to the higher velocities pushing the non-condensable gas downstream. Figure 5.8b presents the effect of different operating temperatures on the non-condensable gas distributions. From the area under the mole fraction x_g line, it could clearly be seen that the volume of the present non-condensable gas decreases with temperature. This is as expected due to the increase in density with an increase in pressure. It can be concluded that temperature is of large influence on the location of the front, due to the changing non-condensable gas density. From the same figure it can be concluded that the condensable mass flow $\dot{m}$ increases with temperature as well, due to an increased power, as a smaller part of the condenser is blocked at a high operating temperature.

5.5.3. Literature comparison

Due to the unknown amount of non-condensable gas in the TU Delft experimental setup, it is not suitable to validate the model using obtained experimental data. Therefore, validation is done using experimental temperature data reported in literature for heat pipes with non-condensable gas. In order to validate the model with a comparable heat pipe and operating

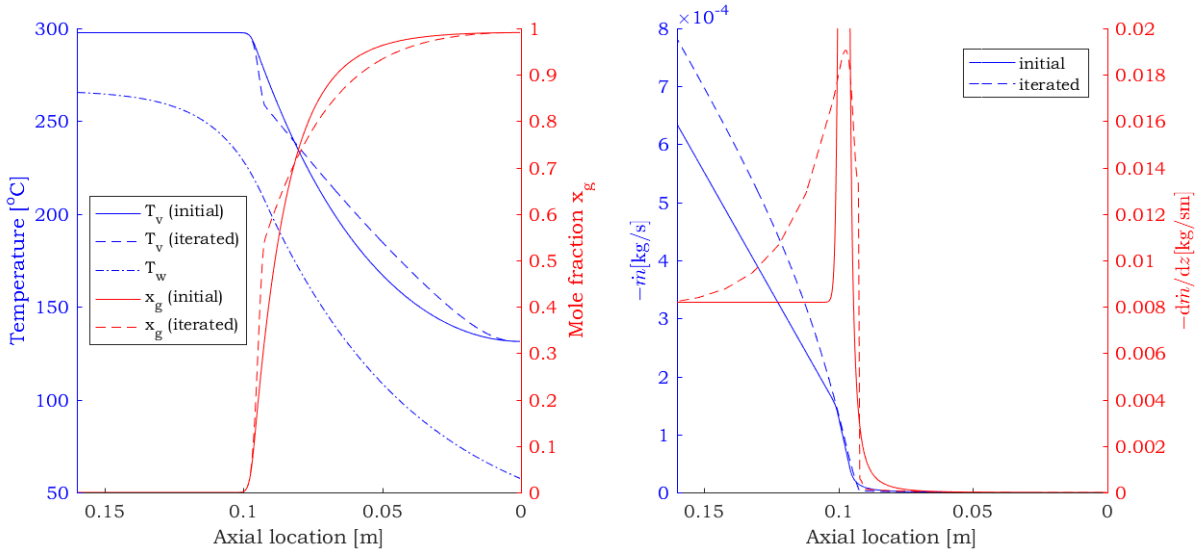

Figure 5.7: Initial and final solution after iteration of vapor space and wall temperature model for conditions as in the TU Delft experimental setup, as noted in Table 5.3. Axial location is the distance from the condenser end. $T_{ev} = 300^{o}C$, $\chi = 0.14$, $\delta = 0.0001m$, $v_{fan} = 5.1m/s$ and $m_g = 0.15g$ of air

conditions, dimensionless numbers have been set up for key heat transfer mechanisms. The first one is axial mass convection versus axial mass diffusion:

$$R_1 = \frac{x_v v}{-D\frac{\mathrm{d}x_v}{\mathrm{d}z}} \tag{5.37}$$

The second dimensionless number includes wall conduction. The TU Delft experimental setup has a thick walled heat pipe, which is uncommon for heat pipes, as it increases heat transfer resistance. From results in this section it was seen that the wall effect is expected to be notable and the developed model is designed to include wall effects. The second dimensionless number represents axial mass convection versus axial wall conduction:

$$R_2 = \frac{x_v v A_v \rho_v h_{fg}}{-k_w A_w \frac{\mathrm{d}T_v}{\mathrm{d}z}} \tag{5.38}$$

It was chosen to validate the model with experimental data of a heat pipe with water and air from a study by Edwards & Marcus[16] and with experimental data of a heat pipe with sodium and argon by Harley[19]. Both are studies on a heat pipe with a wick. The values of the two dimensionless numbers are stated in Table J.1 at the upstream($x_v = 0.95$) and downstream($x_v = 0.05$) side of the front. The values used for determination of the dimensionless numbers are shown in Appendix L. The TU Delft experimental setup has been modelled for different wall thicknesses and thus values for R_2, which showed that the steepening due to wall conduction almost disappeared at a value of 2, which is comparable to that of the case of Harley.

From the values of R_1 one could include that the experimental data of Edwards & Marcus is very similar in terms of the magnitude of convection and diffusion in the front. The data from the heat pipe with sodium and argon has relatively more mass convection compared to diffusion in the front. Unfortunately, both studies do not closely match the value for convection versus wall conductance. The value of most interest is the one upstream($x_v = 0.95$), as largest wall effects have been seen from the model at the upstream side of the front. The experimental data from the study by Harley is closest, but still has a value of R_2 more than four times larger, meaning lower wall effects. More comparable reported experimental data has not been found.

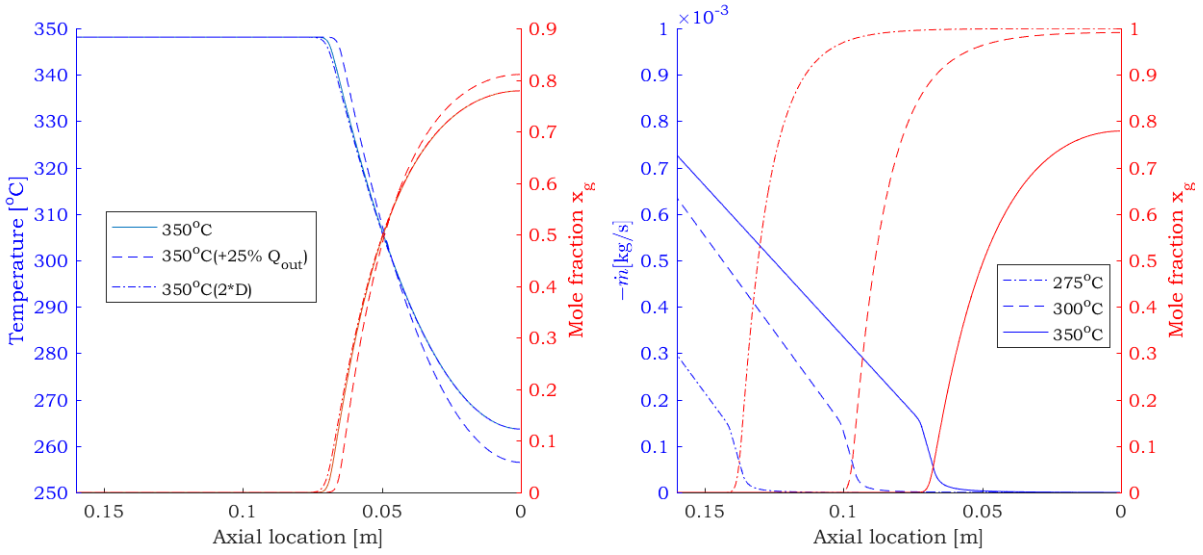

Figure 5.8: Sensitivity analysis of different parameters showing initial solution. A change in heat outflow equal to its error and dependency on diffusivity coefficient D are shown(a). Furthermore, the effect of different evaporator temperatures are presented(b). $\chi = 0.14$, $\delta = 0.0001m$ and $m_g = 0.15g$ of air. The cooling air velocities were $v_{fan} = 6.88m/s(275^oC), 5.08m/s(300^oC), 1.60m/s(350^oC)$

Table 5.4: Values of dimensionless numbers of Equation 5.37 & 5.38

	TU Delft exp setup	**Edwards**	**Harley**
Values shown @[$x_v = 0.95$ - $x_v = 0.05$]	Dowtherm A - Air	Water - Air	Sodium - argon
R_1 (convection/diffusion)	19.5-0.05	18.2-0.05	148-0.32
R_2 (convection/wall conductance)	0.42-0.0001	6.94-0.002	1.78-0.002

Figure 5.9 shows the experimental wall measurements and the results of the model of this study for the same cases. For both cases, the effect of the separate wall calculations of the combined model is almost invisible and the condensation limit is not reached, partly due to the relatively high diffusivity coefficients. The model matches the experimental data points from literature accurately, especially the shape of the front, but also the magnitude of the data points agree with the model. Edwards reported that the amount of non-condensable gas had an expected error of 5% mass basis. Model results with this extra 5% have been included, but the front still is a bit upstream. This could be due to a larger uncertainty on non-condensable gas amount. A notable radial temperature gradient from 2D effects is unexpected, according to the parametric study of Peterson for the case of Edwards. From the results presented by Harley, there is a remarkable data point, which is the fifth from the upstream side. It looks like a plateau is present just before the full temperature drop. This phenomenon has not been reported in other studies and is therefore considered a measurement error.
The validation done shows the accurateness of the developed model. However, no validation could be done on the wall conduction effects, which are clearly present in the TU Delft experimental setup.

5.5.4. TU Delft setup experiment comparison

This section provides a comparison between obtained experimental data and modelling results from the same parameters. As noted in Table 5.3, the error on the non-condensable gas

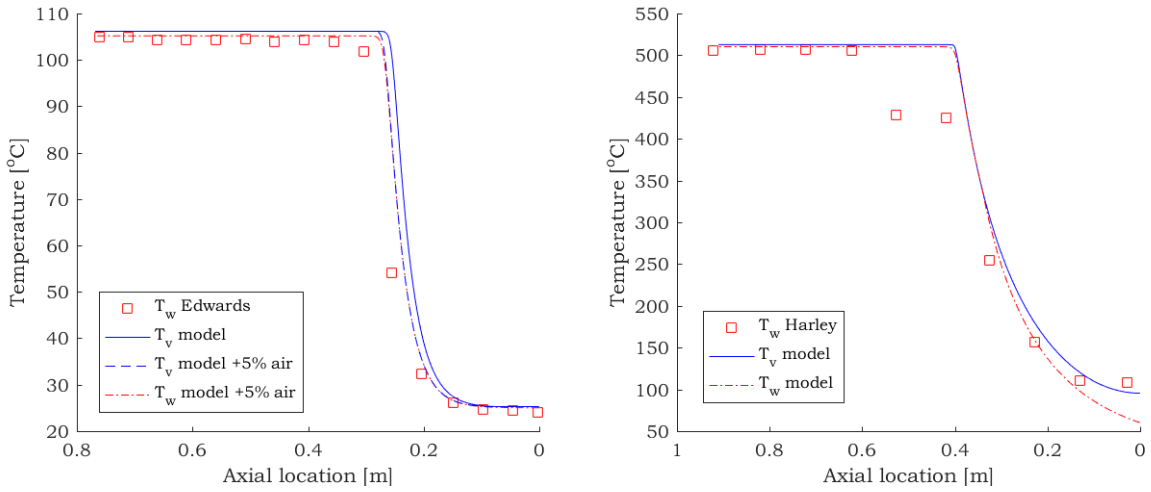

(a) Edwards & Marcus (Water - Air)[16] (b) Harley (Sodium - Argon)[19]

Figure 5.9: Model validation using experimental data from Edwards & Marcus and from Ponnapan, reported by Harley

inside the heat pipe is about 0.3g, which is more than the absolute value. From the energy balance study in Section 4.2 it seemed that the expected amount of non-condensable gas is smaller than the pressure readings suggest.
Figure 5.10 shows modelling results for different non-condensable gas amounts, temperatures and powers. It should be noted that it is impossible to do a full analysis, due to the large uncertainty in non-condensable gas amount. The difference in gas amounts of the shown results is small compared to the measurement error and it shows to shift the temperature profile significantly. One remarkable observation is that both T_v and T_w seem to decrease with about the same small amount in downstream direction. This could be clarified for the wall measurements when looking at the predicted profile. T_v is however expected to drop quickly at the upstream side of the front, so a small decrease equal for different non-condensable gas amount therefore is unexpected. It could however be a systematic error during these tests. In Figure 5.10b the vapor speed has been kept about constant between 340°C and 350°C, in order that the pure effects of non-condensable gas density change could be seen, but no conclusions could be drawn due to measurement inaccuracies.

5.6. Conclusion

This chapter presented a model able to calculate non-condensable gas distribution in a heat pipe, which is based on 1D transport equations of non-condensable gas by diffusion and convection. The non-condensable gas distribution has shown to be strongly dependent on operating pressure and amount of non-condensable gas. For the cases where wall conduction is significant compared to axial vapor convection, the inclusion of wall calculations show that the front is steepened due to wall conduction at its upstream side. A combined model has been devised in which the non-condensable gas transport equations and wall temperature calculations are iteratively solved. With the addition of wall temperature calculations, a condensation limit was required for the region with high non-condensable gas concentration. During validation it was observed that it matches literature data accurately, although the wall conduction addition could not be validated. This model provides a computationally efficient way to model non-condensable gas effects on the temperature profile of heat pipes loaded with non-condensable gas. Especially when the non-condensable gas amount is not exactly known, the error of the model may be acceptable in many cases. The separate wall temperature model can be used to determine the wall temperature profile and to consider the necessity of wall conduction integration into the calculation by the combined model.

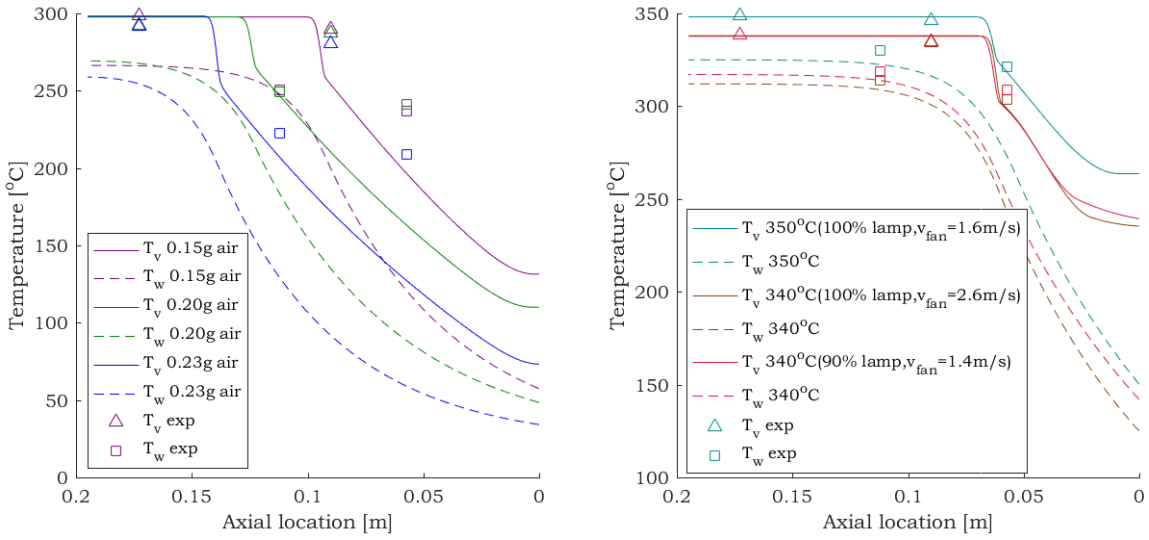

(a) (b)

Figure 5.10: Model results comparison with experimental temperature measurements. (a) shows numerous non-condensable gas amounts, with $\chi = 0.14$, $\delta = 0.0001\text{m}$ and 200rpm. $v_{fan} = 6.49\text{m/s(blue)}, 3.63\text{m/s(green)}, 5.08\text{m/s(purple)}$(b) shows two different T_{ev}, and for 340^{o}C two different powers are shown. The low power is chosen such that axial vapor velocity is equal to the case at 350^{o}C, according to Eq. 3.3. $\chi = 0.14$, $\delta = 0.0001m$ and 200rpm

6

Non-condensable gas in heat pipe assisted annealing

The value of the obtained knowledge of Dowtherm A as the working fluid in a rotating heat pipe in the non-annular flow regime and the developed model describing axial condenser temperature profile lies in its potential to predict performance of such heat pipes in a rotating heat pipe assisted annealing line. The conclusions of the experimental campaign can be translated to a rotating heat pipe as in the application, which was described in Chapter 4. However, when looking at working conditions affecting non-condensable gas distribution, there are differences between the TU Delft experimental setup and a rotating heat pipe to be used in a heat pipe assisted annealing line. This chapter aims to give insight in this difference and in the predicted non-condensable gas distribution and associated temperature profile. Furthermore, a design adjustment is suggested to ensure homogeneous heating of the cold strip.
Dimensions and characteristics of the full scale heat pipe were given in Section 1.5. The main differences in characteristics affecting non-condensable gas distribution between the TU Delft setup and the heat pipe in application at an annealing line lay in the following points.

- Sink temperature;
- Vapor velocity;
- Wall thickness;
- Type of non-condensable gas.

6.1. Rotating heat pipe operating conditions

In the application, the transfer of heat to the sink goes with a much higher heat transfer coefficient. The sink in this case is a steel strip, which wraps over the heat pipe, as was illustrated in Figure 1.5. Earlier experimental research in the heat pipe assisted annealing line project showed that the heat transfer coefficient between outer heat pipe wall and strip is around $7000\mathrm{W/m^2K}$ and the total power of each heat pipe is about 50kW[11]. In initial plant designs, the heat pipes were positioned in a way that heat transfer takes place over 110^o of the heat pipe, which is called the wrap angle. The effective heat transfer coefficient then is $7000 * 110/360 = 2100\mathrm{W/m^2K}$. With this information it can be determined that the temperature difference between steel plate and outer wall required to reach heat pipe power is about $13^o\mathrm{C}$. Typical heat transfer coefficients of the TU Delft experimental setup from outer condenser wall to cooling air were in the order of $20\mathrm{W/m^2K}$. The sink temperature is therefore very different.
Furthermore, the perimeter is 10 times larger, condenser length 5 times and the cross-sectional area of vapor space A_v is 160 times larger for the rotating heat pipe at full scale.

The power is scaled up 100x, from ~500W to ~50kW. With the relatively large increase in A_v, the maximum axial vapor velocity v_{ax} is 1.6 times smaller compared to the values in the TU Delft experimental setup. Vapor velocity is one of the key parameters when calculating non-condensable gas distribution.

6.2. Working fluid and type of non-condensable gas

Different working fluids were selected for heat pipe assisted annealing. Section 1.3.2 described the different working fluids and noted their difference in the magnitude of their vapor pressure. Different fluids are used at different temperature ranges, such that vapor pressures do not exceed 5 bar. Besides Dowtherm A, this study also includes an analysis of heat pipes with cesium as its working fluid. The two proposed fluids and their temperature range are listed in Table 6.1 and the vapor pressure of cesium is calculated using the Antoine equation given in Section F.0.5.
This table also shows the diffusivity coefficient for Dowtherm A and Cesium. The type of non-condensable gas in a heat pipe assisted annealing line is in this case not likely to be air. Annealing is done in a environment of N_2 & H_2. Hydrogen is able to diffuse through metals relatively easily, so it is likely that hydrogen enters heat pipes in a heat pipe assisted annealing line. The experimental campaign of this study has shown the large negative effects of non-condensable gas, which entered through a leak. Heat pipes in a heat pipe assisted annealing line will need to be leak-tight, so the present non-condensable gas in this case is considered to be hydrogen instead of air. For this analysis, the diffusivity coefficient for working fluid with hydrogen is taken. This binary diffusivity coefficient is calculated using the method provided in Section F.0.4 for Dowtherm A. For cesium, values from Aref'ev et al. for cesium and helium are taken, as no better alternative is available in literature, but these values are considered comparable due to the similar characteristic length of helium and hydrogen[7].

Table 6.1: Temperature range and binary diffusivity coefficient D for Dowtherm A and Cesium with hydrogen

	Temperature range[^oC]	D low T [m^2/s]	D high T [m^2/s]
Dowtherm A	150-350	$9.6 * 10^{-4}$	$0.18 * 10^{-4}$
Cesium	450-700	$43 * 10^{-4}$	$3.4 * 10^{-4}$

6.3. Non-condensable gas distribution

The results presented in this chapter are acquired with the vapor space model described in Chapter 5. For this sensitivity analysis, no wall iteration is used. The non-condensable gas distribution for the lower and upper temperature of both Dowtherm A and cesium in a heat pipe assisted annealing line have been modelled. The conditions are similar to heat pipes operating in a heat pipe assisted annealing line. Table 6.2 lists the input variables of modelling work. For the sink temperature, a difference between outer wall and vapor space of 20°C is estimated, which is similar to values found in Chapter 5, where similar heat fluxes were present. This is added to the temperature difference between steel strip and heat pipe outer wall to find the temperature difference between sink and inner heat pipe. The molar concentration for the cesium cases has been estimated by considering the molar concentration of hydrogen at the operating temperature and pressure. The non-condensable amount (0.1g of hydrogen) has been chosen arbitrarily in order to show the effects of several operating conditions.

Figure 6.1 shows the non-condensable gas distribution of heat pipes with Dowtherm A and cesium at their lower and upper internal temperature. Chapter 5 already showed the effect of temperature, which is also clearly visible in this figure. For both working fluids, an increase

Table 6.2: Input variables of model. Values shown are applicable for rotating heat pipes as in a heat pipe assisted annealing line. h_{wo} is the effective heat transfer coefficient from outer wall to sink

Variable		Dowtherm A(150°C)	Dowtherm A(350°C)	Cesium(450°C)	Cesium(700°C)
L_{cond}	[m]		1.0		
r_{wo}	[m]		0.3		
r_{wi}	[m]		0.278		
h_{wo}	[W/m^{2}K]		2100		
p_{vapor}	[bar]	0.050	5.39	0.054	1.11
T_{sink}	[°C]	117	317	417	667
M	[kg/kmol]	166	166	132.9	132.9
c	[kmol/m^3]	0.0013	0.123	0.0018	0.028
ρ_g	[kg/m^3]	0.0029	0.21	0.0018	0.028
k_l	[W/mK]	0.12	0.086	36	36
k_w	[W/mK]	15.8	19.0	20.5	24.4
h_{fg}	[J/kg]	340000	244000	510000	510000

in temperature moves the front downstream due to the decreased non-condensable gas volume. The effect of non-condensable gas is largest for cesium at 450°C, which is due to its low vapor pressure, causing the volume of non-condensable gas to be high. Furthermore, a new phenomenon is also visible. The mole fraction x_g for the low temperatures has a maximum, which is at the equilibrium value of x_v at the sink temperature.
Figure 6.2 shows the associated temperature profiles. For the low temperatures the stabilization is also clearly visible. The temperature at which it stabilizes is temperature of the strip. At this temperature, no heat is rejected to the strip and therefore no condensation takes place. This part is characterized by the absence of vapor flow and thus no gradient in mole fraction exists at steady-state, according to Equation 5.1. For cesium at 450°C, the saturation temperature equal to strip temperature corresponds to a mole fraction x_g of just below 0.5. This effect is lower for water at the shown lower temperature, as the gradient of vapor pressure over temperature is larger at that point. This gradient increases generally with vapor pressure, so this effect is worst at low vapor pressures. This phenomenon increases the condenser length affected by non-condensable gas significantly, as a lower non-condensable gas volume is stored in the blocked part of the condenser.

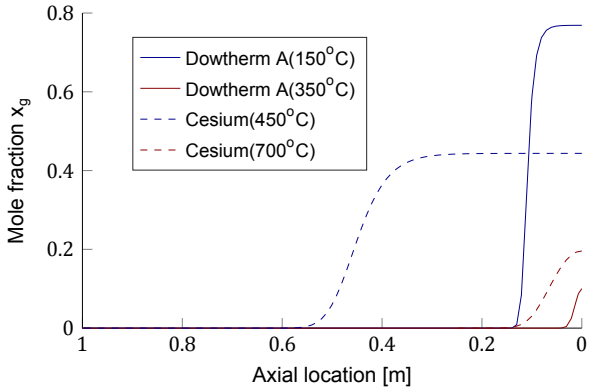

Figure 6.1: Non-condensable gas distribution over the axial length of the condenser with Dowtherm A and cesium as working fluid and hydrogen as non-condensable gas. Hydrogen amount: 0.1g, local power condenser(away from non-condensable gas front): 50kW/m, heat transfer coefficient outer wall to strip: 7000W/m^{2}K, wrap angle: 110^o

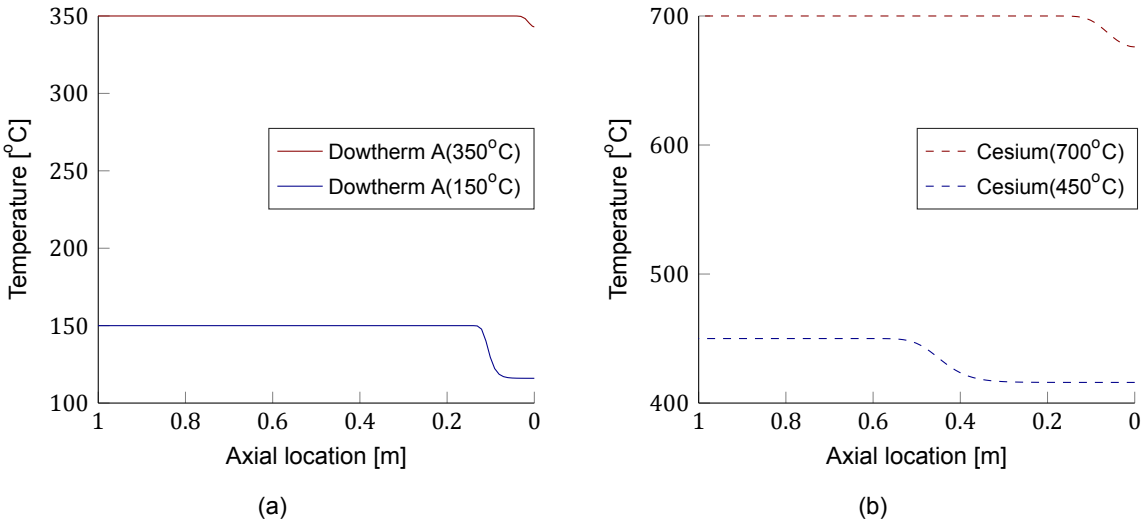

Figure 6.2: Temperature profile from non-condensable gas distribution for Dowtherm A(a) and cesium(b). $m_g = 0.1$g hydrogen

6.4. Design adjustment

The effect caused by a low temperature difference between strip and heat pipe in the condenser shown in previous section causes the effect of non-condensable gas to be even larger. To decrease its effect, a design adjustment is looked into. This adjustment simply is an extension of the heat pipe beyond the cold strip, as shown in Figure 6.3. This extension serves as extra space for the present non-condensable gas. Furthermore, it allows the condenser end to cool down below strip temperature, making it possible to decrease the blocked condenser length. This effect will be shown by modelling results. In these modelling results, the extension had its own heat transfer coefficient to the sink, which was at a much lower temperature than the steel strip.

Figure 6.3: Design adjustment shown; heat pipe with condenser side of heat pipe extended. Cold strip is shown in blue and hot strip in red. The red arrow indicates heat loss from the extension.

Figure 6.4a shows the effect of an extension of 0.2m. For the heat pipe at 700°C, the front has just moved to the right, which is the first advantageous effect of the extension. The second effect is visible at the 450°C case, where the maximum of mole fraction x_g has almost doubled due to the extension. This is due to the fact that condensation occurs at a lower temperature, due to a lower sink temperature of the extension. It is clearly visible that the blocked length has decreased more than the extended length.
Figure 6.4b subsequently shows the effect of heat transfer rate outwards at the extended part. A high heat transfer coefficient yields a steeper front and a small blocked condenser length.

An extension of the heat pipe also brings along extra heat loss. Table 6.3 states the heat outflows according to the model. For the low temperature case, the extension is full of non-

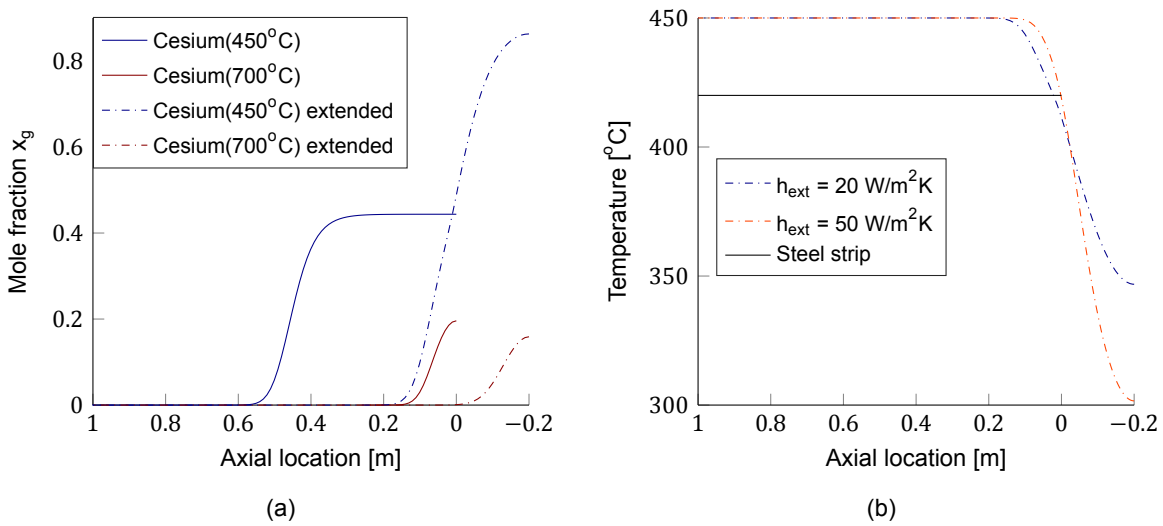

Figure 6.4: Graphs showing the effect of an extension of 0.2m, as shown in Figure 6.3. The change in mole fraction profile for cesium heat pipes is illustrated $h_{ext} = 20\mathrm{W/m^2K}$(a) and the effect of heat transfer coefficient of outer wall to environment is shown for a cesium heat pipe at $450^{o}\mathrm{C}$(b)$m_g = 0.1\mathrm{g}$ hydrogen

condensable gas, which causes it to be at a relatively low temperature. This in turn makes the energy loss of the extension low. The extra heat outputted to the strip is much higher compared to the heat loss of the extension, which shows that the heat pipe is being used more effectively. This is different at high temperature, where the heat loss is high and the increase of heat to the strip is of the same order, which is due to a lower mole fraction of non-condensable gas in the extension.

Table 6.3: Total heat outflow to strip and from extension for a cesium heat pipe at $450^{o}C$ and $700^{o}C$ with and without extension of 0.2m, $h_{ext} = 20\mathrm{W/m^2K}$

	Cesium $450^{o}\mathrm{C}$		Cesium $700^{o}\mathrm{C}$	
	Heat out [W] from extension	Heat out [W] to strip	Heat out [W] from extension	Heat out [W] to strip
w/o extension		26900		45300
0.2m extension	740	45600	3000	50000

6.5. Conclusion

The non-condensable gas distribution has been modelled for operating conditions as in a heat pipe assisted annealing line. During continuous annealing, it is essential that heat transfer to and from the strips is homogeneous to prevent strip breakage. Non-condensable gas causes a temperature gradient to exist in heat pipes, which complicates homogeneous heating. A low difference between heat pipe and cold strip temperature worsens heat pipe performance when non-condensable gas is present, especially at low operating pressure. By extending the condenser beyond the cold strip, space is created for non-condensable gas accumulation. This is especially favorable at relatively low temperatures, due to the associated low pressure and low non-condensable gas density. A high heat transfer coefficient from the outer wall of the extension has shown to increase the amount of non-condensable gas stored in the extension. However, for high temperatures, a significant extension may not be needed, which makes it beneficial to determine the most suitable extension length for every individual heat pipe.

7

Conclusions & Recommendations

Valuable knowledge has been acquired on the internal heat and mass transfer of a rotating heat pipe with Dowtherm A as its working fluid for an innovative energy-efficient concept for annealing steel. The rotating heat pipe has been studied by experiments which were supplemented by theoretical analysis. During commissioning of the experimental test rig multiple impactful deficiencies came to light, notably an eccentricity affecting liquid flow, a leak causing non-condensable gas presence and an inaccurate pressure sensor inside the heat pipe causing the amount of non-condensable gas to be unknown. The deficiencies however encouraged a thorough analysis of the perceived phenomena and resulted in additional research done on the effects of non-condensable gas in heat pipes. This study partly succeeded in acquiring full knowledge on the performance of Dowtherm A in a rotating heat pipe, which was not researched before and is required for the industrial application. Furthermore, a computationally efficient model has been derived that is able to predict non-condensable gas distribution, which can be used to model a heat pipe assisted annealing line in operation and find the operating boundaries. The model is unique, as it combines the simplicity of a 1D model with additional calculations of the wall, which is of large influence for heat pipes with a relatively thick wall.

7.1. Conclusions

The following conclusions can be given as an answer to the research questions of this study.

Heat transfer characteristics

- Dowtherm A is able to serve as the working fluid of a heat pipe and has shown to be able to transport at least 280W axially through the inner geometry, which is 192,000W/m^2 and corresponds to a vapor flow of 0.001kg/s. The internal axial vapor temperature difference between evaporator, adiabatic section and begin of the condenser was 1.7 ± 2.2^{o}C at operating conditions minimizing non-condensable gas effects. The axial convective transport shows to be between two and three orders more efficient than pure conduction through stainless steel. This makes it utmost suitable for homogeneous heating and cooling of a steel strip. The axial temperature gradient measured over the condenser is most probably due to non-condensable gas.
- A typical heat transfer coefficient radially through the film in the evaporator of $4200 \mathrm{W/m^2K} \pm$ 15% has been found in the non-annular flow regime with an expected film thickness ranging from $0.5 * 10^{-4}$m to $1.6 * 10^{-4}$m and heat fluxes between 26,200 and 39,300W/m^2. Nucleate boiling was the most likely dominant heat transfer mechanism for temperatures and rotational speeds tested, between Froude numbers 0.75 and 16 as predicted by literature for a centrifugal force below 20g(900rpm). Nucleate boiling is the heat transfer mechanism with lowest resistance at the rotational speeds studied.
- Signs of enhanced heat transport by turbulent mixing in the film in the condenser have been seen at the higher rotational speeds tested in the non-annular flow regime. A heat

transfer coefficient of $1750\mathrm{W/m^2K} \pm 15\%$ was found at rotational speeds between 700 and 750rpm with an expected film thickness of $1.7 * 10^{-4}\mathrm{m}$ at $340^{o}\mathrm{C}$. Measurements at lower temperatures and rotational speeds were considered inaccurate. It matches the correlation used for heat transport by turbulent mixing.

- An increase in rotational speed is expected to thicken the film in the non-annular flow regime, which itself causes an increase in heat transfer resistance. However, a minor decrease with rotational speed in the evaporator was seen. The obtained results in the condenser suggested that turbulent mixing was the dominant heat transfer mechanism at the upper rotational speeds tested in the non-annular flow regime, which is expected to be independent on rotational speed. The effect of thickening is apparently compensated by the increased centrifugal force and wall velocity. No accurate data is available at low rotational speeds in the condenser. Furthermore, a further increase of rotational speed to the annular flow regime was associated with a five times larger resistance of the condenser liquid layer, to $R * \mathrm{d}z = 0.050\mathrm{Km/W} \pm 15\%$ for $\chi = 0.15$. No notable change was observed in the evaporator.
- The resistance of the film in the evaporator slightly decreased with a temperature increase in the non-annular flow regime. This is according to expectations, as viscosity decreases. No accurate data was obtained for the resistance dependency on temperature in the condenser.
- No dependency on heat flux and power input/output was observed. A slight decrease of resistance of nucleate boiling is expected, which seemed present but was within the error margin. The resistance of axial fluid transport dependency on heat flux is expected to be negligible in the non-annular flow regime at the operating pressures studied. For the condenser, no accurate data was available due to non-condensable gas effects.
- The rotational speed at which complete annular flow started, was well predicted by Baker's empirical expression based on a heat pipe with water. For $\chi = 0.15$ and $340^{o}\mathrm{C}$, annular flow was reached at 1070±25rpm, while it was expected at 1100rpm. A lower filling ratio yielded in annular flow to be reached at a lower rotational speed, as expected.
- Axial liquid transport is vital for heat pipe performance. The loss of controllability of the heat pipe has been experienced to the fullest at rotational speeds where dryout occurred, as reaching steady-state at dryout was not succeeded. Evaporator dryout was considered an effect of heat pipe eccentricity and started at a rotational speed between 725 and 860rpm for different filling ratios, heat flows and temperatures. The heat pipe retook operation at around 1000rpm.
- The low figure of merit is not a perfect indicator for working fluid heat transfer performance in operating conditions studied and intended operating conditions of a heat pipe assisted annealing line. It is based on working fluid properties affecting conduction through the film, axial liquid transport and axial vapor transport. Resistance to axial vapor and liquid transport through the pool in the TU Delft experimental setup were considered negligible and other heat transfer mechanisms were dominant in both condenser and evaporator. Improved models should include properties affecting nucleate boiling, natural convection and turbulent mixing within the film, as those enhance heat transfer significantly if present.

Non-condensable gas

- The effect of non-condensable gas is most significant at low pressure, disturbing the axial temperature homogeneity of the heat pipe. High axial vapor velocity decreases this effect. Furthermore, the amount of non-condensable gas directly influences the part of the condenser influenced by it.
- For the modelling of non-condensable gas distribution in a thick walled heat pipe, the 2_{nd} derivative of wall temperature in axial direction causes a significant steepening of the condensable vapor and non-condensable gas front, making it necessary to add wall temperature profile calculations to a 1D model.

- Although validation for heat pipes with relatively high axial wall conductance could not be done, it did show to agree well with literature data for common heat pipe dimensions and operating conditions. As it has shown to be difficult in this study to measure non-condensable gas amount, the error of the gas amount is likely to bring along higher inaccuracies than the inaccuracy of the model in many cases. The computational efficiency of a 1D model is an effective way of predicting non-condensable gas effects in those cases.
- The sink temperature of the condenser is of large influence on non-condensable gas distribution, especially at low vapor pressures. A sink temperature close to internal heat pipe temperature increases the condenser length affected by non-condensable gas.
- The derived model has shown that an extension at the condenser end serves as a container for non-condensable gas and leads to a higher concentration when cooled below cold strip temperature, resulting in a decrease of blocked condenser length by more than the extension length. Extra heat losses at the extension may increase total power to the steel strip. Whether this is the case mainly depends on the amount of non-condensable gas, operating pressure and temperature difference between heat pipe and cold strip.

7.2. Recommendations

This study could not fully answer the research questions set up at the start. Further research is recommended in certain area's.

- The obtained experimental data on heat transfer through the film at the condenser did not allow strong conclusions to be drawn due to the presence of non-condensable gas. Further experiments with a more leak tight heat pipe are required to gain more knowledge about heat transfer characteristics of Dowtherm A in the condenser.
- The minor eccentricity had a large negative effect on heat pipe operation. This is not expected to be a problem at low Froude numbers. However, the phenomena observed related to eccentricity are not well understand and the effects are disruptive for heat pipe operation. It is therefore recommended to look further into the phenomena regarding eccentricity.
- Obtain experimental data on a rotating heat pipe on full scale, as this has never been done before and could result in deviations from information on rotating heat pipes in literature, which were not clearly present at the scale of TU Delft experimental setup. Compared to this study, centrifugal forces will be higher at full scale.
- Assess the minimal amount of pulled up liquid by the wall required to fully wet the evaporator wall at maximum power. This should be sufficient for the vaporization rate. If this is insufficient, local dryout occurs. The rotational speed should be increased if this is the case. Large heat pipes with similar heat fluxes are more prone to this type of dryout, as the film thickness increases with $r^{1/2}$ and the vaporization rate increases with r with constant heat flux.
- Determine the expected amount of non-condensable gas inside the heat pipes and use it to model the effect of it on a heat pipe assisted annealing line.

Bibliography

[1] Cesium - NIST Chemistry WebBook. [Date Accessed: 2020-07-31] https://webbook.nist.gov/cgi/inchi?ID=C7440462&Mask=4&Type=ANTOINE&Plot=on.

[2] Coefficients of Linear Thermal Expansion - The Engineering Toolbox. [Date Accessed: 2020-05-09] https://www.engineeringtoolbox.com/linear-expansion-coefficients-d_95.html.

[3] Circular economy, . URL https://circulareconomy.worldsteel.org/. [Date Accessed: 2020-07-30].

[4] Energy use in the steel industry - fact sheet 2019, . [Date Accessed: 2020-07-30] https://www.worldsteel.org/en/dam/jcr:f07b864c-908e-4229-9f92-669f1c3abf4c/fact_energy_2019.pdf.

[5] Slip Ring SRH2578 Series, 2018. [Date Accessed: 2020-07-30] https://www.penlink.se/fileadmin/user_upload/Penlink/Products/Rotary_Joints/Slip_Rings/Standard/SRH2578.pdf.

[6] Iron and Steel - recommended actions, 2020. [Date Accessed: 2020-02-05] https://www.iea.org/reports/iron-and-steel#recommended-actions.

[7] K. M. Aref'ev, B. F. Remarchuk, and M. A. Guseva. Diffusion of metal vapors in gases and the transport properties of vapors. *Journal of Engineering Physics*, 42(6):621–626, 1982. ISSN 00220841. doi: 10.1007/BF00835092.

[8] M. Ashby, H. Shercliff, and D. Cebon. *Materials - engineering, science, processing and design*. Butterworth-Heinemann, 2010.

[9] J. Baker, T. Oliver, L. Lin, R. Ponnapan, and J. Leland. Correlations of Critical Froude Number for Annular-Rimming Flow in Rotating Heat Pipes. *Journal of Fluids Engineering*, 123(4):909, 2001. ISSN 00982202. doi: 10.1115/1.1411967. URL http://fluidsengineering.asmedigitalcollection.asme.org/article.aspx?articleid=1484338.

[10] R. Bertossi, N. Guilhem, V. Ayel, C. Romestant, and Y. Bertin. Modeling of heat and mass transfer in the liquid film of rotating heat pipes. *International Journal of Thermal Sciences*, 52(1):40–49, 2012. ISSN 12900729. doi: 10.1016/j.ijthermalsci.2011.09.017. URL http://dx.doi.org/10.1016/j.ijthermalsci.2011.09.017.

[11] M. Çelik. *Rotating Heat Pipe Assisted Annealing*. PhD thesis, 2020. https://repository.tudelft.nl/islandora/object/uuid:1e0e9c0b-06f0-4b11-ab5f-40fcfcacbea4?collection=research.

[12] T. C. Daniels and N. S. Al-Baharnaht. Temperature and Heat Load Distribution in Rotating Heat Pipes. *AIAA Journal*, 18(2):202–207, 1980. ISSN 00011452. doi: 10.2514/3.50749.

[13] T. C. Daniels and F. K. Al-Jumaily. Investigations of the factors affecting the performance of a rotating heat pipe. *International Journal of Heat and Mass Transfer*, 18(7-8):961–973, 1975. ISSN 00179310. doi: 10.1016/0017-9310(75)90190-8.

[14] T. C. Daniels and R. J. Williams. Experimental temperature distribution and heat load characteristics of rotating heat pipes. *International Journal of Heat and Mass Transfer*, 21(2):193–201, 1978. ISSN 00179310. doi: 10.1016/0017-9310(78)90223-5.

[15] Dow Chemical Company. Dowtherm A - Heat Transfer Fluid, Product Technical Data. 1997. URL https://www.preprints.org/manuscript/201806.0048/v1/download/supplementary.

[16] D. K. Edwards and B. D. Marcus. Heat and mass transfer in vicinity of vapor- gas front in gas- loaded heat pipe. *ASME Pap 71-WA/HT-29*, (71):155–162, 1971.

[17] R. S. Gaugler. Heat Transfer Device, 1944. URL https://patentimages.storage.googleapis.com/2b/dd/b3/5f4d19cee50bf8/US2350348.pdf.

[18] J. B. Gill. Apparatus for closing and opening a metal tube(patent: 3266287), 1966.

[19] C. Harley and A. Faghri. Transient Two-Dimensional Gas-Loaded Heat Pipe Analysis. *Journal of Heat Transfer*, 116(3):716, may 1994. ISSN 00221481. doi: 10.1115/1.2910927.

[20] R. Hashimoto, H. Itani, K. Mizuta, K. Kura, and Y. Takahashi. Heat transport performance of rotating heat pipes installed in high-speed spindle. Technical report, Mitsubishi Heavy Industries, Ltd., 1996.

[21] K. Hijikata, S. J. Chen, and C. L. Tien. Non-Condensable Gas Effect On Condensation in a Two-Phase Closed Thermosyphon. Technical Report 8, 1984.

[22] H. Jouhara and A.J. Robinson. An experimental study of small-diameter wickless heat pipes operating in the temperature range 200C to 450C. *Heat Transfer Engineering*, 30 (13):1041–1048, 2009. ISSN 01457632. doi: 10.1080/01457630902921113.

[23] J. Kierzenka and L. F. Shampine. A BVP Solver based on residual control and the MATLAB PSE. *ACM Transactions on Mathematical Software*, 27(3):299–316, 2001.

[24] B. N. Krivosheev, M. P. Kukharskii, and V. D. Portnov. Experimental investigation of heat transfer in a centrifugal heat pipe with an optimized layer of heat-transfer agent. *Journal of Engineering Physics*, 43:1242, 1982.

[25] R. Laubscher and R. T. Dobson. Theoretical and experimental modelling of a heat pipe heat exchanger for high temperature nuclear reactor technology. *Applied Thermal Engineering*, 61(2):259–267, 2013. doi: 10.1016/j.applthermaleng.2013.06.063. URL http://dx.doi.org/10.1016/j.applthermaleng.2013.06.063.

[26] L. Lin and A. Faghri. Heat transfer analysis of stratified flow in rotating heat pipes with cylindrical and stepped walls. *International Journal of Heat and Mass Transfer*, 40(18):4393–4404, 1997. ISSN 00179310. doi: 10.1016/S0017-9310(97)00060-4.

[27] L. Lin and A. Faghri. Condensation in rotating stepped wall heat pipes with hysteretic annular flow. *Journal of Thermophysics and Heat Transfer*, 12(1):94–99, 1998. ISSN 08878722. doi: 10.2514/2.6307.

[28] L. Lin and M. Groll. Critical conditions for collapse of annular flow in a rotating heat pipe with a cylindrical wall. *Heat Transfer Engineering*, 17(3):29–34, 1996. ISSN 15210537. doi: 10.1080/01457639608939878.

[29] B. D. Marcus and G. L. Fleischman. Steady-state and transient performance of hot reservoir gas-controlled heat pipes. *American society of mechanical engineers*, NASA-CR-73, 1970.

[30] P. J. Marto. An analytical and experimental investigation of rotating, noncapillary heat pipes. Technical Report Report No.: NASA CR-130373, 1973.

[31] R. Marto and H. Weigel. The development of economical rotating heat pipes., 1982. URL http://dx.doi.org/10.1016/B978-0-08-027284-9.50067-X.

[32] B. Meltzer. High Temperature Rotating Heat Pipe Setup - Heat Pipe Assisted Annealing Project. Technical report, TU Delft, 2016.

[33] A. F. Mills. *Basic Heat and Mass Transfer*. Pearson, second edition, 2014.

[34] M. F. Modest. *Radiative Heat Transfer*. Academic Press, second edition, 2003.

[35] J. A. Moya and N. Pardo. The potential for improvements in energy efficiency and CO2 emissions in the EU27 iron and steel industry under different payback periods. *Journal of Cleaner Production*, 52:71–83, 2013. doi: 10.1016/j.jclepro.2013.02.028.

[36] P. Nemec, A. Čaja, and M. Malcho. Mathematical model for heat transfer limitations of heat pipe. *Mathematical and Computer Modelling*, 57(1-2):126–136, 2013. ISSN 08957177. doi: 10.1016/j.mcm.2011.06.047. URL http://dx.doi.org/10.1016/j.mcm.2011.06.047.

[37] G. Paulussen (Tata Steel). Heat pipe assisted strip treatment (patent: WO2011012257A1), 2011.

[38] H. Peller, V. Lippig, D. Straub, and R. Waibel. Thermofluiddynamic experiments with a heated and rotating circular cylinder in crossflow, part 1: Subcritical heat transfer measurements. *Experiments in Fluids*, 120:113–120, 1984.

[39] P. F. Peterson and C. L. Tien. Numerical and Analytical Solutions for Two-Dimensional Gas Distribution in Gas-Loaded Heat Pipes. *Journal of Heat Transfer*, 111(3):598, oct 1989. ISSN 00221481. doi: 10.1115/1.3250724.

[40] S. González Pinto, S. Pérez Rodríguez, and J. I.Montijano Torcal. On the numerical solution of stiff IVPs by Lobatto IIIA Runge-Kutta methods. *Journal of Computational and Applied Mathematics*, 82(1-2):129–148, 1997. ISSN 03770427.

[41] D. Reay, P. Kew, and R. McGlen. *Heat pipes: theory, design and applications*. Heinemann, 2014.

[42] R. C. Reid, J. M. Prausnitz, and B. E. Poling. *The Properties of Gases and Liquids*. McGraw-Hill, 4 edition, 1988.

[43] W. M. Rohsenow. *A method of correlating heat transfer data for surface boiling of liquids*. Cambridge, Mass. : M.I.T. Division of Industrial Cooporation, 5 edition, 1952. doi: http://hdl.handle.net/1721.1/61431.

[44] S. Saad, C. Ching, and D. Ewing. The transient response of wicked heat pipes with non-condensable gas. *Applied Thermal Engineering*, 37(May 2012):403–411, 2011. URL https://doi.org/10.1016/j.applthermaleng.2011.11.058.

[45] M. G. Semena and Y. A. Khmelëv. Hydrodynamic regimes of a liquid in a smooth-walled rotating heat pipe. *Journal of Engineering Physics*, 43(5):1235–1242, 1982. doi: 10.1007/BF00826544.

[46] K. N. Shukla. Transient response of a gas-controlled heat pipe. *AIAA Journal*, 19(8):1063–1070, 1981. doi: 10.2514/3.7842.

[47] K. N. Shukla, A. Brusly Solomon, and B. C. Pillai. Experimental studies of rotating heat pipes. *Heat Transfer - Asian Research*, 38(8):475–484, 2009. ISSN 10992871. doi: 10.1002/htj.20265.

[48] F. Song, D. Ewing, and C. Y. Ching. Fluid flow and heat transfer model for high-speed rotating heat pipes. *International Journal of Heat and Mass Transfer*, 46(23):4393–4401, 2003. ISSN 00179310. doi: 10.1016/S0017-9310(03)00292-8.

[49] F. Song, D. Ewing, and C. Y. Ching. Experimental investigation on the heat transfer characteristics of axial rotating heat pipes. *International Journal of Heat and Mass Transfer*, 47(22):4721–4731, 2004. ISSN 00179310. doi: 10.1016/j.ijheatmasstransfer.2004.06.001.

[50] F. Song, D. Ewing, and C. Y. Ching. Heat transfer in the evaporator section of moderate-speed rotating heat pipes. *International Journal of Heat and Mass Transfer*, 51(7-8): 1542–1550, 2008. ISSN 00179310. doi: 10.1016/j.ijheatmasstransfer.2007.07.020.

[51] Z. S. Spakovszky. Thermodynamics and Propulsion. Technical report, Massachusetts Institute of Technology, 2006.

[52] K. H. Sun and C. L. Tien. Thermal performance characteristics of heat pipes. *International Journal of Heat and Mass Transfer*, 18(3):363–380, 1975. doi: 10.1016/0017-9310(75)90026-5.

[53] T. W. Uhlmann, M. B. H. Mantelli, M. Manzoni, M. Marengo, and P. Eskilson. Experimental Tests on Sodium Thermosyphons. *Joint 18th IHPC and 12th IHPS*, 2016.

[54] S. van Leeuwen. Design optimisation and commissioning of the Delft rotating heat pipe setup. Technical report, TU Delft, 2018.

[55] T. W. Watson and H. E. Robinson. Thermal conductivity of a sample of type 316 stainless steel. Technical report, National Bureau of Standards, Silver Spring, Maryland, 1963. URL https://www.govinfo.gov/content/pkg/GOVPUB-C13-bb31c3f26e1bbf969c51d7614aeba8d1/pdf/GOVPUB-C13-bb31c3f26e1bbf969c51d7614aeba8d1.pdf.

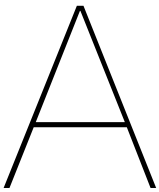

Appendix: Rotating Heat Pipe drawing

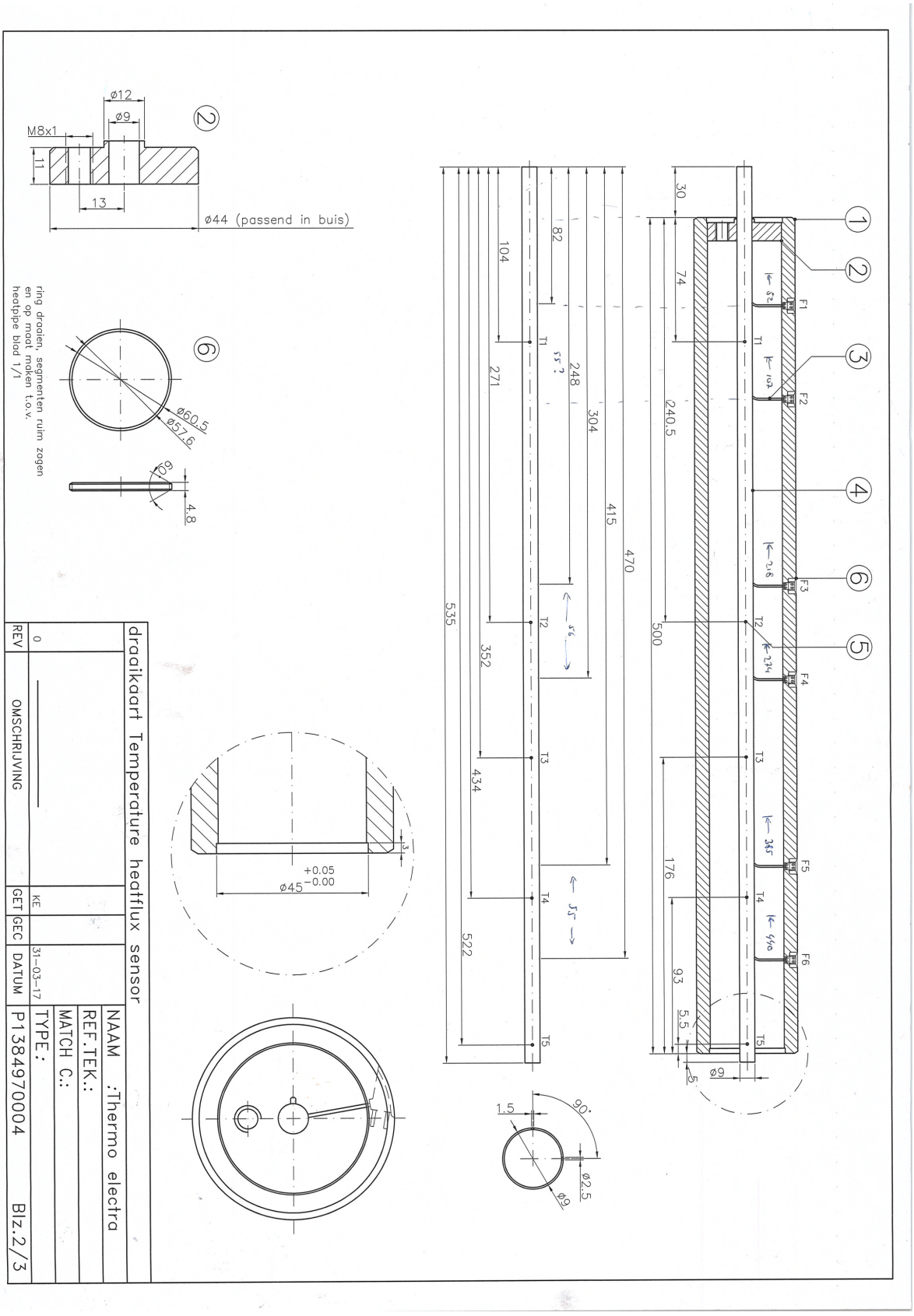
ø12
ø9
M8x1
11
13
ø44 (passend in buis)
ring draaien, segmenten ruim zagen
en op maat maken t.o.v.
heatpipe blad 1/1
ø60.5
ø57.6
90°
4.8
draaikaart Temperature heatflux sensor
NAAM :Thermo electra
REF.TEK.:
MATCH C.:
TYPE :
P1384970004
Blz.2/3
REV
OMSCHRIJVING
GET
GEC
DATUM
KE
31-03-17
0
+0.05
ø45 -0.00
3
1.5
90°
ø2.5
ø9
30
74
240.5
500
82
248
304
415
470
104
271
352
434
522
535
176
93
5.5
5
ø9
F1
F2
F3
F4
F5
F6
T1
T2
T3
T4
T5

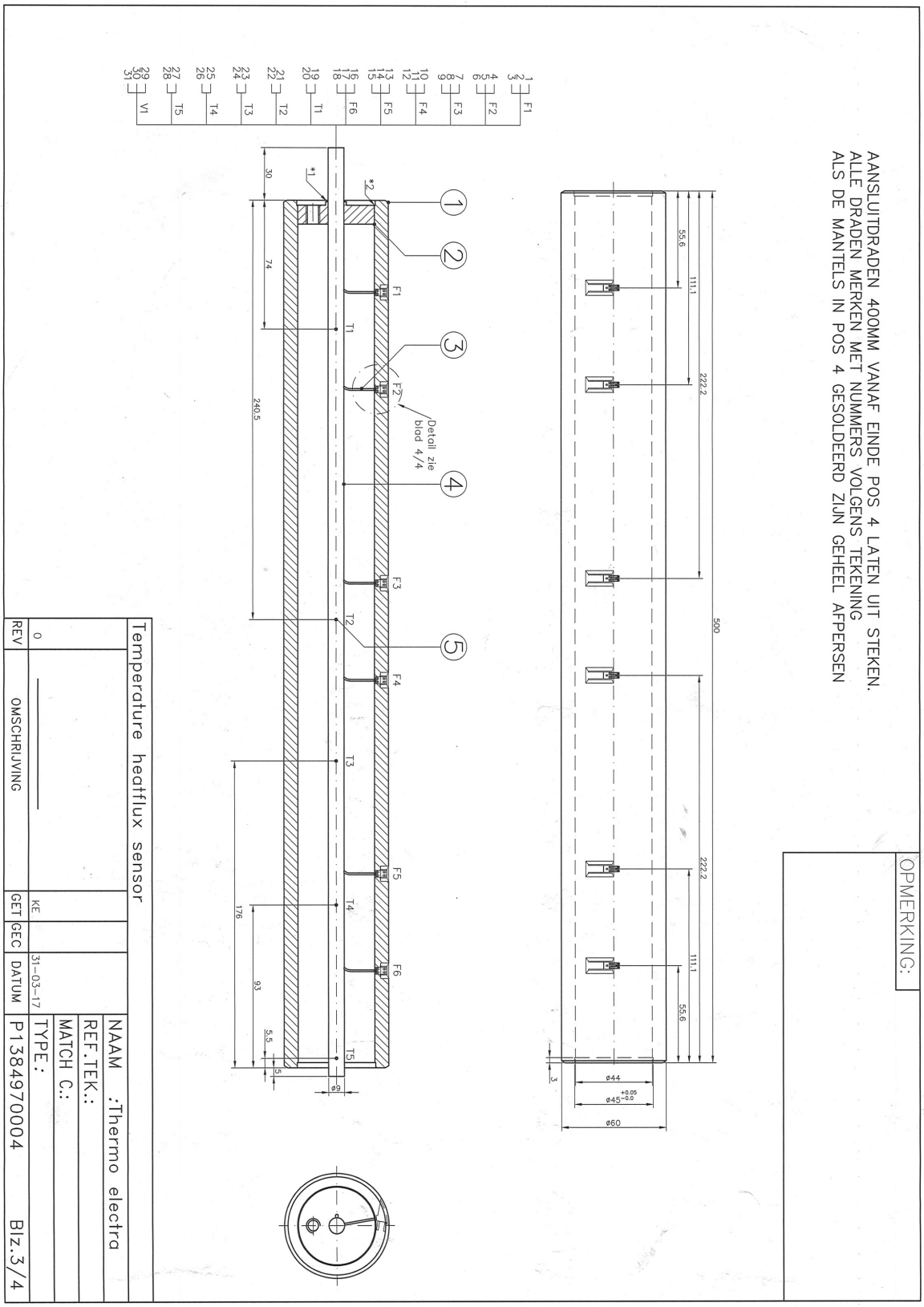
AANSLUITDRADEN 400MM VANAF EINDE POS 4 LATEN UIT STEKEN.
ALLE DRADEN MERKEN MET NUMMERS VOLGENS TEKENING
ALS DE MANTELS IN POS 4 GESOLDEERD ZIJN GEHEEL AFPERSEN
OPMERKING:
Detail zie blad 4/4
Temperature heatflux sensor
NAAM :Thermo electra
REF.TEK.:
MATCH C.:
TYPE:
P1384970004
DATUM
GEC
GET
REV
OMSCHRIJVING
31-03-17
KE
Blz.3/4

B

Appendix: Heat flux sensor error freezer test

As described in Section 3.2, a test is carried out to obtain more knowledge about the error of the heat flux sensors. During commissioning, it turned out that all heat flux sensors were measuring a radial heat inflow in stationary ambient condition. In the absence of a temperature gradient and therefore a driving force for heat flow, this is not feasible. This error is expected to be an absolute offset. The goal of this test is to check whether this error is relative or absolute. The test has been done two times. The following steps were carried out:

1. Heat pipe disconnected from slip ring and rotational motor. Upper parts removed from bearing houses, oven and air duct.
2. Inserting heat pipe in climate chamber, which is set to cool to 253K.
3. Keeping the heat pipe inside climate chamber during the day.
4. Prepared setup: insulate contact points (bearings)
5. Removed heat pipe from climate chamber, placed back into setup and connected slip ring. All as quick as possible and without touching of the central part of the heat pipe. Gloves reduced the contact heat conduction during the placement.
6. Allowing it to heat up to ambient temperature, while measuring the temperatures and heat fluxes of the heat pipe. It is not rotating during the test. The cabinet stayed closed, to minimize local air flows.

Characteristics of the two tests are given in table B.1. A picture of the heat pipe just after being placed back into the setup is shown in figure B.1. The temperature of the heat pipe right after being placed back into the setup is plotted in figure B.2.
When the heat pipe has a uniform temperature over the axial length, a more or less homogeneous heating up is expected. During the test, the values of the heat flux sensors are corrected, such that they measure zero at ambient conditions of the heat pipe. This correction is an absolute number and ranges from $-433\mathrm{W/m^2}$ to $-1074\mathrm{W/m^2}$. If the error is relative to temperature or heat flux instead, non-homogeneity would be expected in heat flux readings, in relation to the size of the correction.

The results of both the first and second test are shown in figure B.4. The applied absolute correction is the same for both tests. Wall temperature readings, heat flux readings and outer wall temperature (converted by equation G.1) are plotted. The main differences between these tests are the start temperature, the ambient temperature and whether there is liquid inside or not.

Figure B.1: Heat pipe just out of climate chamber/freezer, with insulation at contact areas and slip ring connected

Table B.1: Freezer tests characteristics

	Test #1	**Test #2**
Pressure inside	Ambient	Ambient
Ambient Temperature	18^oC	24^oC
Amount of Dowtherm A in Heat Pipe	Empty	95g
Open or closed	Open(at filling hole)	Closed
Angular position sensors	Top side	Top side

Overall results show non-homogeneous readings of the heat flux sensors. During both tests, wall sensor 4 measures relatively high heat fluxes, which is also clear from the graph showing heat flux as a function of outer wall temperature. In an ideal situation with a constant and homogeneous ambient condition, the heat flux against outer wall temperature would be equal for the six sensor locations. However, the readings show something else. From the temperature plots it is also clear that the middle of the heat pipe is heating up more quickly than the sides. This is confirmed visually by figure B.3. This could be due to a higher convective heat transfer coefficient at the outside surface in the middle.
Besides, the local peak of the heat fluxes at an outer wall temperature of about 16^oC is an interesting observation. At this wall temperature, the inner temperature reads 12^oC, which is equal to the freezing point of Dowtherm A at ambient pressure.

Conclusion

The heating up of the heat pipe did not happen in a fully homogeneous way. The geometry of the heat pipe and the non-homogeneous ambient conditions, causing the outside heat transfer coefficient to differ over the axial length, are likely to play a major role in non-homogeneity. For example, the outside wiring tube has relative small volume to outer area ratio and is therefore likely to heat up more quickly. Axial heating from that end of the heat pipe then starts to play a role as well, making the interpretation of the results more difficult. Furthermore, the distribution of solid Dowtherm A in test #2 probably was not homogeneous

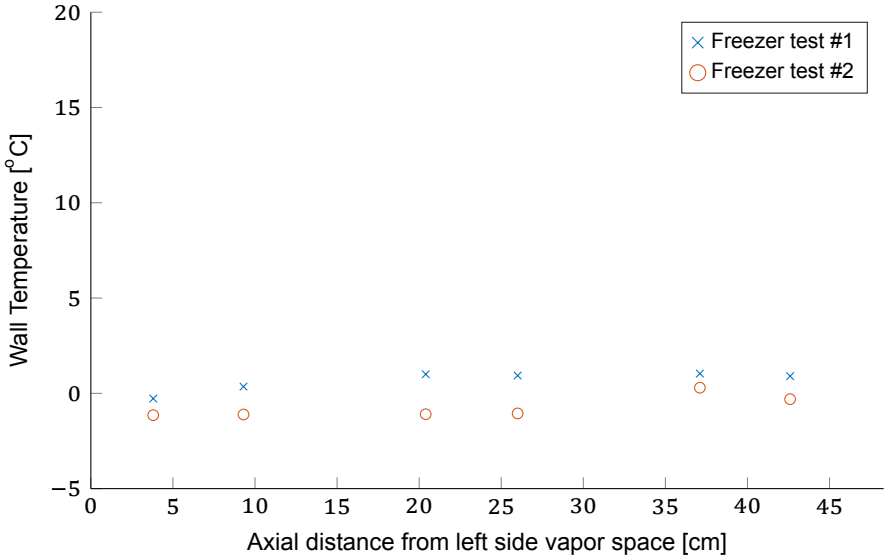

Figure B.2: Wall temperature sensors readout right after coming out of the climate chamber

as well. The heat pipe was more or less horizontal in the climate chamber, but probably not exactly, The result of this is a higher heat capacity at one end of the heat pipe, which causes non-homogeneity again.

However, no sign of a relative error has been seen in these tests. A sign would be a relation between heat flux correction and magnitude of heat flux during heating up. From these tests, no correlation could be seen. The heat fluxes of wall sensor 1 and 6 are for example close to each other during heating up, but their offset correction is very different. As there are signs of a non-uniform outside heat transfer coefficient and a non-uniform heating up due to the geometry (beside the main part) of the heat pipe, it is not possible to draw a complete conclusion on the type of offset of the wall heat flux sensors. The absence of an observable relative error in this test does give information for the worst case scenario where the offset is a relative offset. These tests give insight in the severity of this possible relative offset, although an absolute offset is more likely.

During the experimental campaign, the maximum heat fluxes typically were around $20,000\text{W/m}^2$ in the oven and $13,000\text{W/m}^2$ in the condenser. At low power, typically these were around $13,000\text{W/m}^2$ in the oven and $6,000\text{W/m}^2$ in the condenser. The accuracy of the heat flux sensor calibration is +-15%, which implies minimally +-900W/m^2 (condenser, low power). As the offset at ambient conditions is of the same order of size as the considered accuracy of the heat flux sensors, only an extreme change in the offset with temperature and heat flux would cause a worsened accuracy.

Recommendations

These tests did not allow to draw a strong conclusion. For future similar cases, it is advised to have more accurate calibration done. This is difficult due to the temperature limitations of the outside wiring tube, which cannot handle low and high temperatures. Recommendations for future tests:

- Perform the test with an empty heat pipe in order to eliminate an uneven solid Dowtherm A distribution (and thus an uneven heat capacity distribution) and the effect of the melting of the working fluid;
- Close the heat pipe with a plug in order to eliminate convective heat inflow at one side through the filling hole;

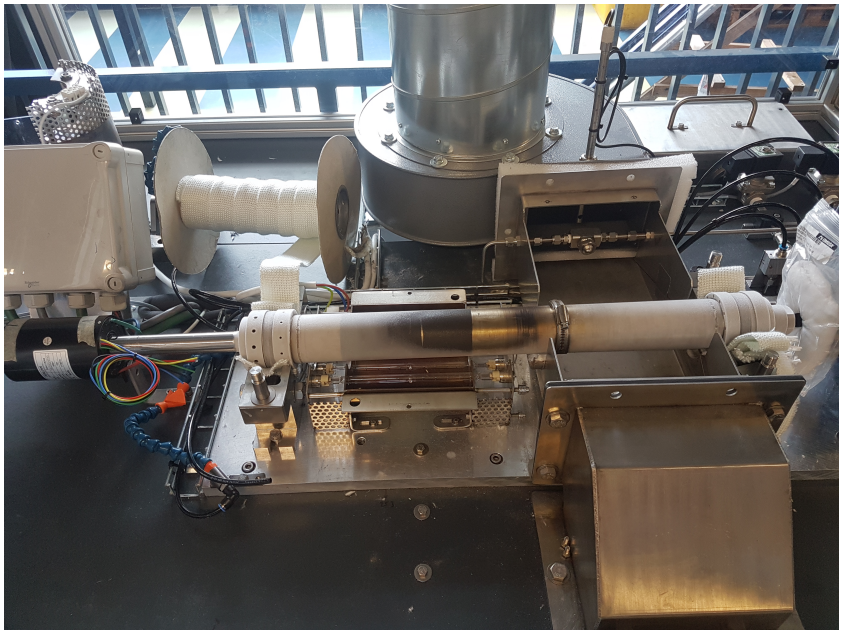

Figure B.3: Heat pipe after 2 minutes, showing ice to start disappearing in the middle of the heat pipe

- Improve the homogeneity of the outside heat transfer coefficient;
- Apply some insulation at the outside wiring tube, in such an amount that the outside wiring tube temperature profile over time equals that of the main part of the heat pipe. This can be measured with the wiring temperature sensor;
- Perform more tests to exclude randomness in the results.

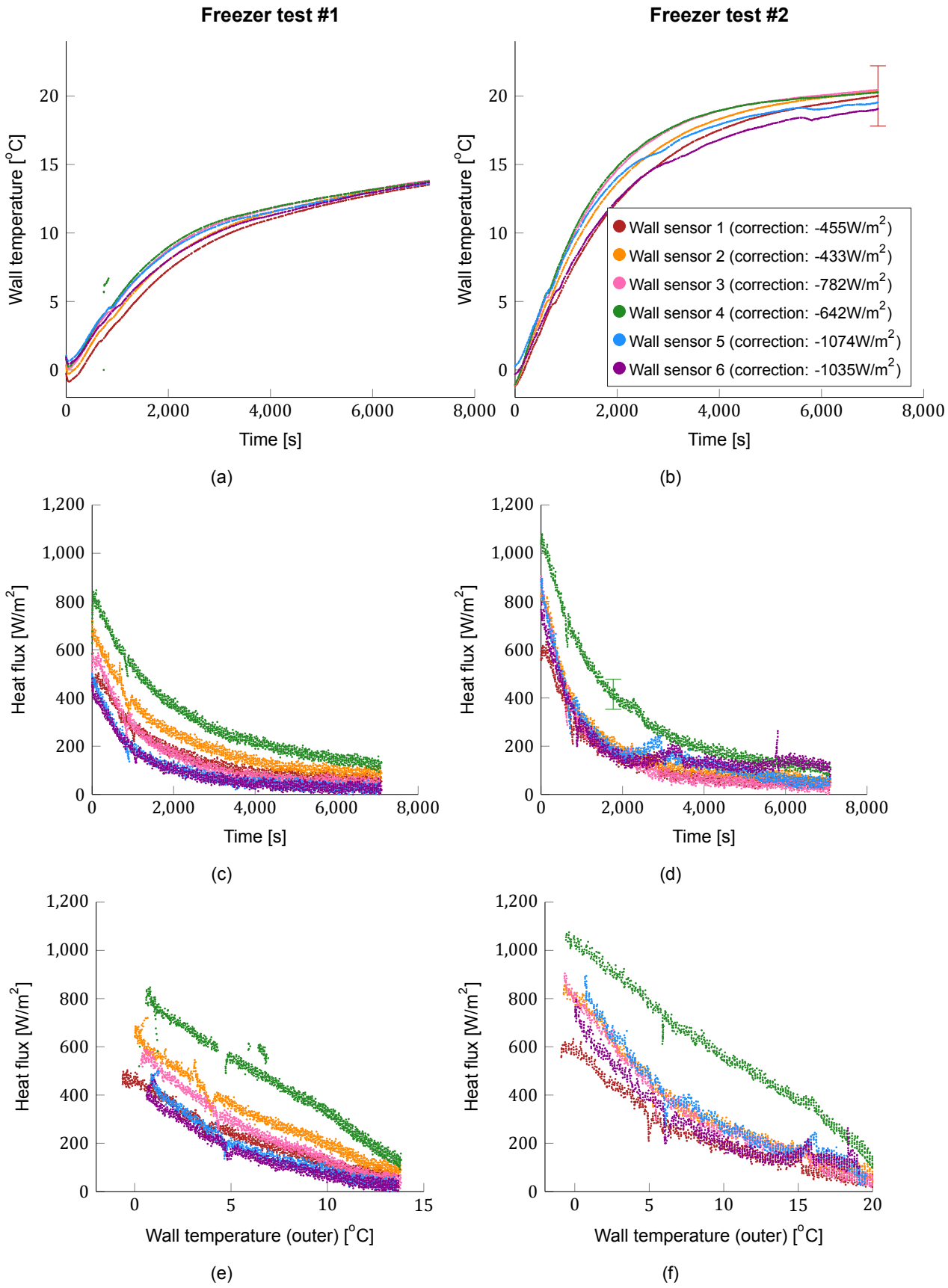

Figure B.4: Process of heat pipe going back to ambient temperature with test #1(left) and test #2(right). The two error bars show the accuracy of the temperature and heat flux sensors.

C

Appendix: Rotational unbalance heat pipe

The eccentricity also brings along a rotational unbalance. This caused heavy audible vibrations, which restricted the maximum rotational speed and could influence liquid flow inside. This has been overcome by adding balancing weights to the heat pipe. The balancing was done using rollers, as shown in Figure C.1. As the support points of the rollers are in the middle of the heat pipe instead of at the bearing surfaces at the sides, the eccentricity in this case is at the opposite side in angular direction. These rollers can be used to determine the size and angular location of the balancing weight. Once balanced on the rollers, the balancing weight is moved 180 degrees in angular direction to have a balanced heat pipe in the actual setup. The balancing weight is placed at the heat pipe part in the condenser, as shown in Figure 3.6. Lightweight screws are inserted into special holes in the bearing block to fine tune the balancing. The total weight of the material used for balancing was about 95g on a total weight of the heat pipe of 11.3kg. The weight could have been reduced if the balancing weight was placed on a smaller angular range, but this way of mounting the weight was most practical, also with regard to the limited space in the setup.
The rollers had some resistance, which brought along inaccuracy. The resistance was low enough to balance the heat pipe accurate enough, such that the entire range of rotational speed was accessible without remarkable vibrations.

Figure C.1: Process of balancing showing the heat pipe on the rollers

D

Appendix: Setup control & safety measures

The setup is controlled via a connected PC. Measures are taken to minimize hazards and to protect the components of the heat pipe.

The setup is controlled by Labview via a GUI in which rotational speed, lamp power and cooling fan power can be set. The lamp power is set as a percentage of the maximum power. The measurements of all the sensors are visible. Inside temperature, heat flow and inside & wall temperature measurements are plotted real-time to allow the monitoring of the heat pipe, which visualizes measurement trends and slopes during running. Furthermore, an estimation of the total heat input by the oven is calculated real-time according to the method described in Section 4.2.1. The GUI is shown in below. The cooling of the outside wiring tube is controlled directly via four needle valves.

Safety measures are taken first of all to protect people working with the setup or in the lab in general. The combination of the high speed rotation of a large mass and the working temperatures bring along potential risks for people working with it. Secondly, measures are taken to prevent the heat pipe's components from breaking. The following is done to ensure a safe and durable operation of the heat pipe:

- The setup is in a closed cabinet with acrylic panels. This allows visual monitoring of the components, but will prevent potential flying objects leaving the cabinet, which have come loose;
- The setup has an emergency button, which shuts down the rotational motor, oven and condenser cooling fan;
- Contact sensors check whether the cabinet doors are closed;
- Contact sensors check the position of the hot upper oven panel. If it is not in the correct place, the setup stops automatically. It is essential that the lamps are shut down when the oven panel is not in the position as designed, as it gets much hotter than other components;
- The oven and cooling fan can only be started when the heat pipe is rotating;
- The set rotational speed is constantly compared with the actual rotational speed. A discrepancy may be caused by the heat pipe being blocked. Rotational power is undesired in this situation and therefore the rotational motor is stopped when a discrepancy occurs;

- An upper limit for the pressure is set in two ways. Exceeding this limit shuts down the oven. The pressure is measured with the inaccurate pressure sensor. Furthermore, it is also determined from the inner temperature readings using the vapor pressure of Dowtherm A. This pressure limit also functions as a temperature limit.

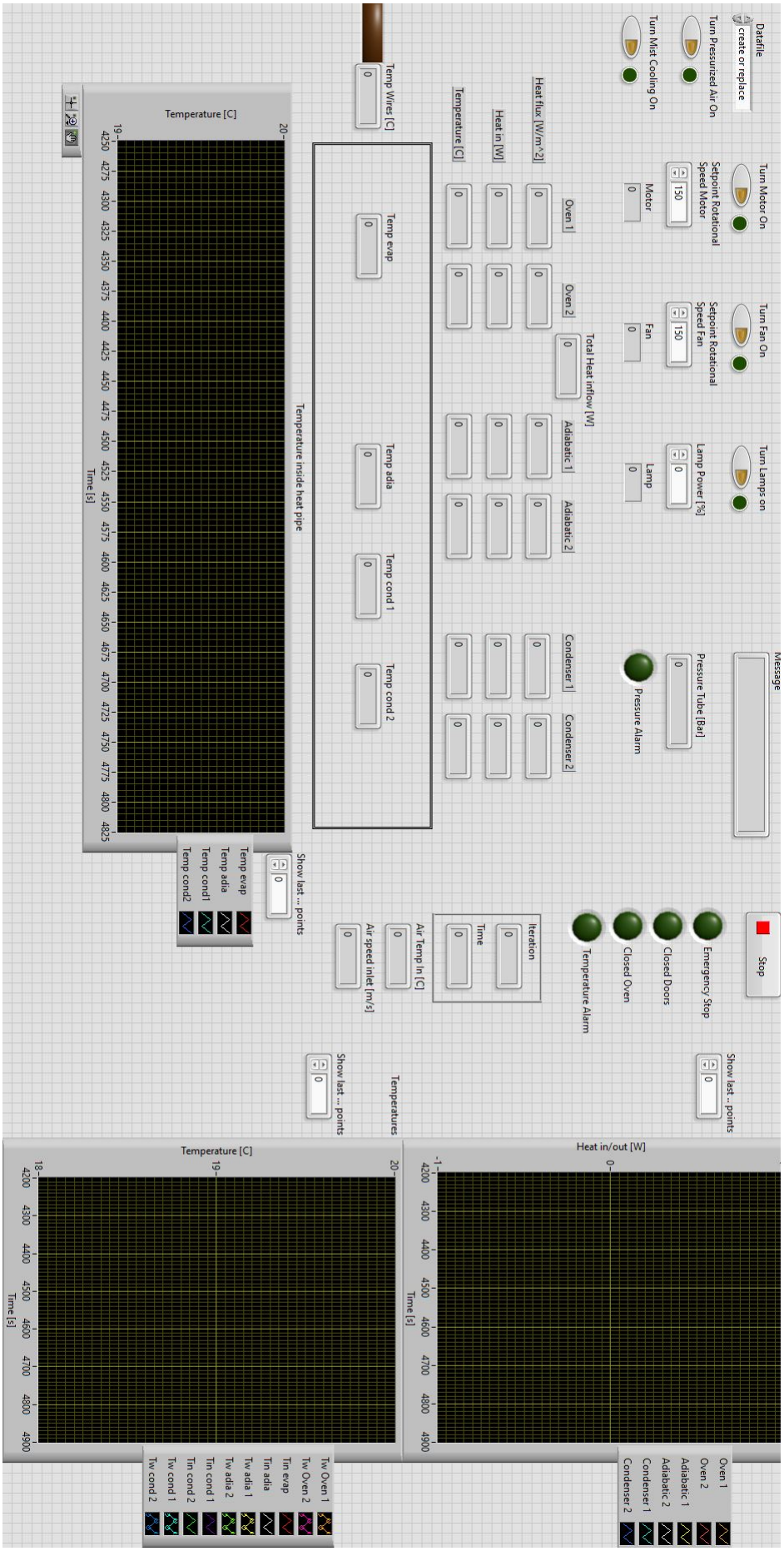
Datafile
create or replace
Turn Pressurized Air On
Turn Mist Cooling On
Turn Motor On
Setpoint Rotational Speed Motor
Motor
Turn Fan On
Setpoint Rotational Speed Fan
Fan
Turn Lamps on
Lamp Power [%]
Lamp
Message
Pressure Tube [Bar]
Pressure Alarm
Stop
Emergency Stop
Closed Doors
Closed Oven
Temperature Alarm
Heat flux [W/m^2]
Heat in [W]
Temperature [C]
Oven 1
Oven 2
Total Heat inflow [W]
Adiabatic 1
Adiabatic 2
Condenser 1
Condenser 2
Iteration
Time
Air Temp In [C]
Air speed inlet [m/s]
Temp Wires [C]
Temp evap
Temp adia
Temp cond 1
Temp cond 2
Temperature inside heat pipe
Show last ... points
Temperature [C]
Time [s]
Temp evap
Temp adia
Temp cond1
Temp cond2
Heat in/out [W]
Oven 1
Oven 2
Adiabatic 1
Adiabatic 2
Condenser 1
Condenser 2
Temperatures
Tw Oven 1
Tw Oven 2
Tin evap
Tin adia
Tw adia 1
Tw adia 2
Tin cond 1
Tin cond 2
Tw cond 1
Tw cond 2

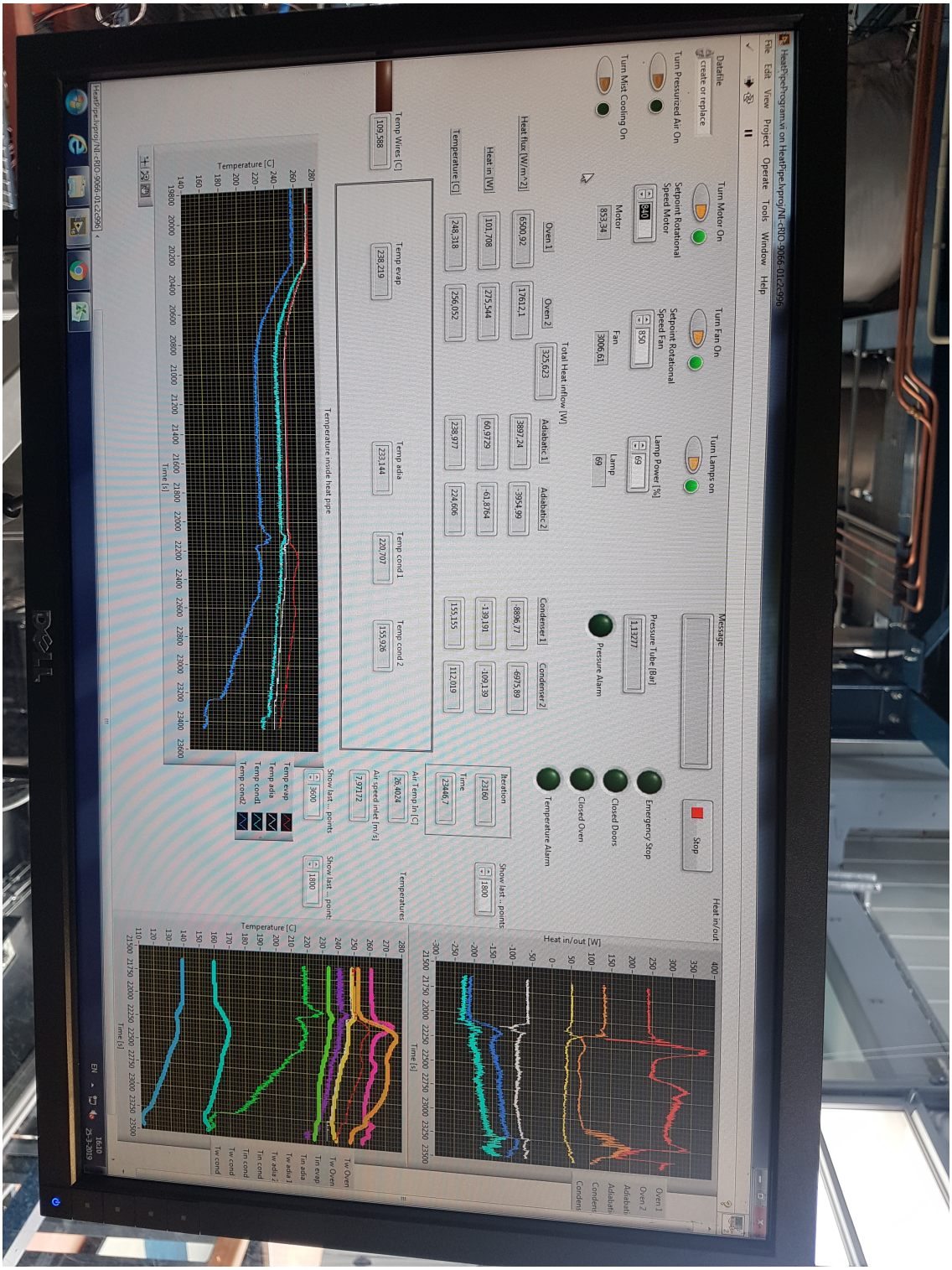
HeatPipeProgramvi on HeatPipeHypro/NI-cRIO-9066-01c2c996
File Edit View Project Operate Tools Window Help
Datafile
create or replace
Turn Motor On
Turn Fan On
Turn Lamps on
Turn Pressurized Air On
Setpoint Rotational Speed Motor
Setpoint Rotational Speed Fan
Lamp Power [%]
Turn Mist Cooling On
Motor
Fan
Lamp
Message
Stop
Heat in/out
Heat flux [W/m^2]
Heat in [W]
Temperature [C]
Oven1
Oven2
Total Heat inflow [W]
Adiabatic1
Adiabatic2
Condenser1
Condenser2
Pressure Tube [Bar]
Pressure Alarm
Emergency Stop
Closed Doors
Closed Oven
Temperature Alarm
Heat in/out [W]
Show last ... points
Iteration
Time
Air Temp in [C]
Air speed inlet [m/s]
Temperatures
Temp Wires [C]
Temp evap
Temp adia
Temp cond 1
Temp cond 2
Temperature inside heat pipe
Temperature [C]
Time [s]
Tw Oven
Tin evap
Tin adia
Tw adia 2
Tw adia 1
Tin cond
Tw cond

E

Appendix: Working fluid degradation

This section provides the data of the gas chromatography–mass spectrometry analysis on used Dowtherm A in the rotating heat pipe setup. It has been used for about 80 hours at a maximum temperature of 350°C

Figure E.1 shows the qualitative results, which shows the presence of phenol, naphthalene and dibenzofuran. Subsequently, a quantitative analysis has been done, which results in the following concentrations:

- Phenol 97mg/kg;
- Dibenzofuran 88mg/kg;
- Naphthalene 12mg/kg.

The relevance of this analysis is the potentially extra non-condensable gas formation. Phenol and naphthalene have vapor pressures higher than that of Dowtherm A, making it a potential non-condensable gas. The values showed that the mass concentration of those substances is 0.01%. It has been calculated that this causes about 1% extra non-condensable gas, which is considered negligible compared to the large non-condensable gas uncertainty in the rotating heat pipe.

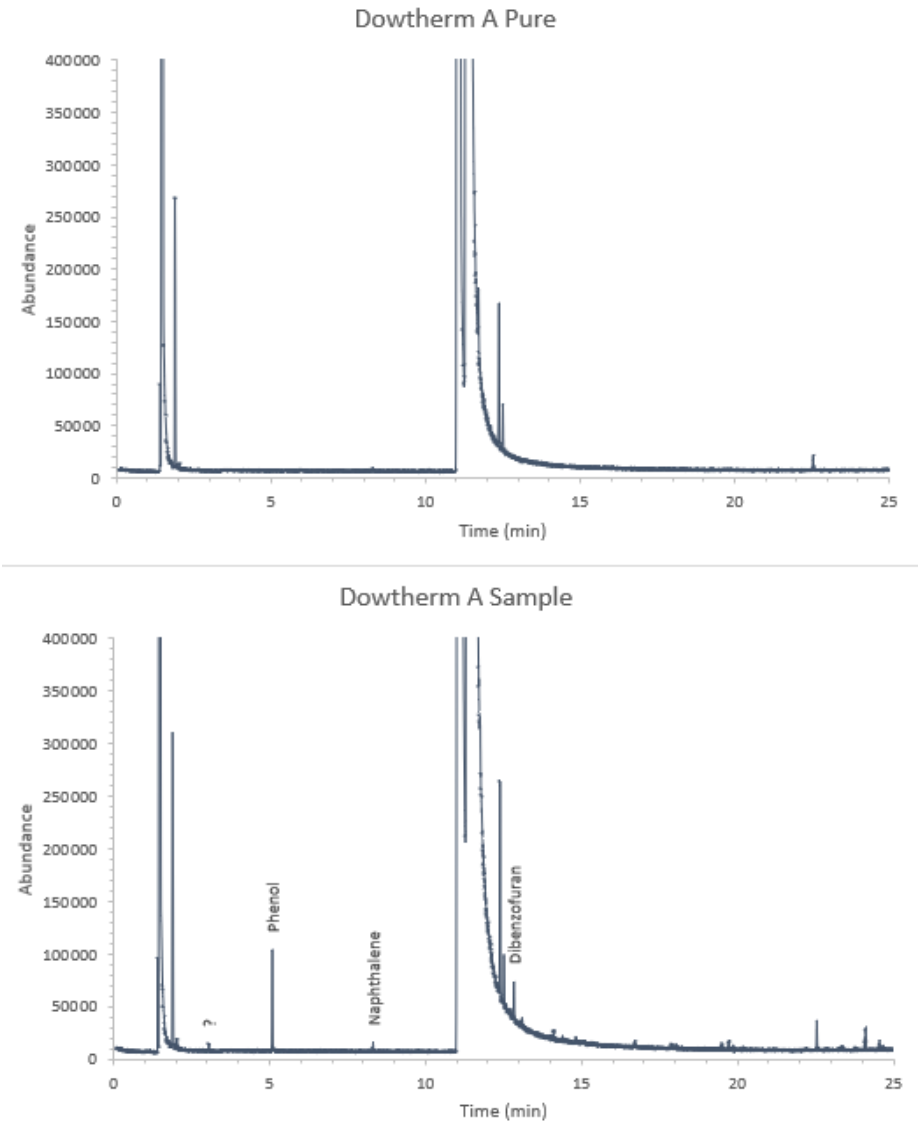
Dowtherm A Pure
Abundance
400000
350000
300000
250000
200000
150000
100000
50000
0
0
5
10
15
20
25
Time (min)
Dowtherm A Sample
Abundance
400000
350000
300000
250000
200000
150000
100000
50000
0
?
Phenol
Naphthalene
Dibenzofuran
0
5
10
15
20
25
Time (min)

Figure E.1

F

Appendix: Material properties

F.0.1. Thermal conductivity of SS316

The following equation based on experimental results by Watson and Robinson is used[55]:

$$k_{SS316} = 100 * \left(0.1333 + 0.1727\frac{T}{1000} - 0.04334\left(\frac{T}{1000}\right)^2 + 0.0332\left(\frac{T}{1000}\right)^3\right) \quad \text{(F.1)}$$

With k_{SS316} in W/mK and T in ^oC.

F.0.2. Surface tension of liquid Dowtherm A

The following equation is an expression for surface tension of Dowtherm A in air is found in literature.
Source: https://www.thermalfluidscentral.org/encyclopedia/index.php/Thermophysical_Properties:_Dowtherm

$$\sigma = 1/1000 * exp\Big(4.3058 - (1.7285 * 10^{-2})T + (1.4156 * 10^{-4})T^2 - (6.784 * 10^{-7})T^3 + (1.524 * 10^{-9})T^4 - (1.3701 * 10^{-12})T^5\Big) \quad \text{(F.2)}$$

Where T is in ^oC and σ in kg/s^2.

F.0.3. Coefficient of thermal expansion Dowtherm A

$$\beta = 1.158 * 10^{-8}T^2 - 2.157 * 10^{-6}T + 9.916 * 10^{-4} \quad \text{(F.3)}$$

Where β is in $1/K$ and T in ^oC.

F.0.4. Diffusivity coefficient

The binary diffusivity coefficient of Dowtherm A with air and of Dowtherm A with hydrogen is determined according to the method of Fuller et al. described in the book 'The Properties of Gases and Liquids'[42]. It states that the diffusivity coefficient can be determined with an error of about 4% with the following equation for substances A and B.

$$D_{AB} = \frac{0.00143T^{1.75}}{PM_{AB}^{0.5}\left((\sum_v)_A^{1/3} + (\sum_v)_B^{1/3}\right)^2} \quad \text{(F.4)}$$

Where T is in Kelvin, P in bar, $M_{AB} = 2\left(1/M_A + 1/M_B\right)^{-1}$ and D_{AB} is the binary diffusion coefficient in cm^2/s. $\sum_v$ is the sum of atomic diffusion volumes, as stated by Figure F.1.

TABLE 11-1 Atomic Diffusion Volumes

Atomic and Structural Diffusion Volume Increments			
C	15.9	F	14.7
H	2.31	Cl	21.0
O	6.11	Br	21.9
N	4.54	I	29.8
Aromatic ring	−18.3	S	22.9
Heterocyclic ring	−18.3		

Diffusion Volumes of Simple Molecules			
He	2.67	CO	18.0
Ne	5.98	CO_2	26.9
Ar	16.2	N_2O	35.9
Kr	24.5	NH_3	20.7
Xe	32.7	H_2O	13.1
H_2	6.12	SF_6	71.3
D_2	6.84	Cl_2	38.4
N_2	18.5	Br_2	69.0
O_2	16.3	SO_2	41.8
Air	19.7		

Figure F.1: Atomic diffusion volumes[42]

F.0.5. Cesium vapor pressure

Vapor pressure of cesium according to the Antoine equation and its parameters[1]:

$$log_{10}(p) = A - \frac{B}{T + C} \tag{F.5}$$

With vapor pressure p in bar and temperature T in Kelvin

A	B	C
3.69576	3453.122	-26.829

F.0.6. Dowtherm A saturated liquid and vapor properties

Table F.2 and F.3 show the saturated liquid and vapor properties of Dowtherm A supplied by the manufacturer.

Figure F.2: Saturated liquid properties of Dowtherm A[15]

Table 3—Saturated Liquid Properties of DOWTHERM A Fluid (SI Units)

TEMP °C	VAPOR PRESS. bar	VISCOSITY mPa sec	SPECIFIC HEAT kJ/kg K	THERMAL COND. W/mK	DENSITY kg/m³	TEMP °C	VAPOR PRESS. bar	VISCOSITY mPa sec	SPECIFIC HEAT kJ/kg K	THERMAL COND. W/mK	DENSITY kg/m³
12	0.00	5.52	1.550	0.1400	1065.9	225	0.48	0.33	2.148	0.1059	883.5
15	0.00	5.00	1.558	0.1395	1063.5	230	0.54	0.32	2.162	0.1051	878.7
20	0.00	4.29	1.573	0.1387	1059.6	235	0.61	0.31	2.176	0.1043	873.8
25	0.00	3.71	1.587	0.1379	1055.7	240	0.69	0.30	2.190	0.1035	868.9
30	0.00	3.25	1.601	0.1371	1051.7	245	0.77	0.29	2.204	0.1027	864.0
35	0.00	2.87	1.616	0.1363	1047.8	250	0.87	0.28	2.218	0.1019	859.0
40	0.00	2.56	1.630	0.1355	1043.8	255	0.97	0.27	2.231	0.1011	854.0
45	0.00	2.30	1.644	0.1347	1039.8	257.1	1.01	0.27	2.237	0.1008	851.9
50	0.00	2.07	1.658	0.1339	1035.8	260	1.08	0.27	2.245	0.1003	849.0
55	0.00	1.88	1.673	0.1331	1031.8	265	1.20	0.26	2.259	0.0995	843.9
60	0.00	1.72	1.687	0.1323	1027.8	270	1.33	0.25	2.273	0.0987	838.7
65	0.00	1.58	1.701	0.1315	1023.7	275	1.48	0.24	2.288	0.0979	833.6
70	0.00	1.46	1.715	0.1307	1019.7	280	1.63	0.24	2.302	0.0971	828.3
75	0.00	1.35	1.729	0.1299	1015.6	285	1.80	0.23	2.316	0.0963	823.0
80	0.00	1.25	1.744	0.1291	1011.5	290	1.98	0.22	2.330	0.0955	817.7
85	0.00	1.17	1.758	0.1283	1007.4	295	2.17	0.22	2.344	0.0947	812.3
90	0.00	1.09	1.772	0.1275	1003.2	300	2.38	0.21	2.359	0.0939	806.8
95	0.00	1.03	1.786	0.1267	999.1	305	2.60	0.20	2.373	0.0931	801.3
100	0.01	0.97	1.800	0.1259	994.9	310	2.84	0.20	2.388	0.0923	795.8
105	0.01	0.91	1.814	0.1251	990.7	315	3.10	0.19	2.403	0.0915	790.1
110	0.01	0.86	1.828	0.1243	986.5	320	3.37	0.19	2.417	0.0907	784.4
115	0.01	0.82	1.842	0.1235	982.3	325	3.66	0.18	2.432	0.0899	778.6
120	0.01	0.77	1.856	0.1227	978.1	330	3.96	0.18	2.448	0.0891	772.8
125	0.02	0.73	1.870	0.1219	973.8	335	4.29	0.17	2.463	0.0883	766.9
130	0.02	0.70	1.884	0.1211	969.5	340	4.64	0.17	2.479	0.0875	760.9
135	0.03	0.67	1.898	0.1203	965.2	345	5.00	0.17	2.494	0.0867	754.8
140	0.03	0.64	1.912	0.1195	960.9	350	5.39	0.16	2.511	0.0859	748.6
145	0.04	0.61	1.926	0.1187	956.6	355	5.80	0.16	2.527	0.0851	742.3
150	0.05	0.58	1.940	0.1179	952.2	360	6.24	0.15	2.544	0.0843	735.9
155	0.06	0.56	1.954	0.1171	947.8	365	6.69	0.15	2.561	0.0835	729.4
160	0.07	0.53	1.968	0.1163	943.4	370	7.18	0.15	2.579	0.0827	722.8
165	0.08	0.51	1.982	0.1155	938.9	375	7.68	0.14	2.597	0.0819	716.1
170	0.09	0.49	1.996	0.1147	934.5	380	8.22	0.14	2.616	0.0811	709.2
175	0.11	0.47	2.010	0.1139	930.0	385	8.78	0.14	2.636	0.0803	702.2
180	0.13	0.46	2.023	0.1131	925.5	390	9.37	0.13	2.657	0.0795	695.0
185	0.15	0.44	2.037	0.1123	920.9	395	9.99	0.13	2.678	0.0787	687.7
190	0.18	0.42	2.051	0.1115	916.4	400	10.64	0.13	2.701	0.0779	680.2
195	0.21	0.41	2.065	0.1107	911.8	405	11.32	0.12	2.725	0.0771	672.5
200	0.24	0.39	2.079	0.1099	907.1	410	12.03	0.12	2.751	0.0763	664.6
205	0.28	0.38	2.093	0.1091	902.5	415	12.78	0.12	2.779	0.0755	656.5
210	0.32	0.37	2.107	0.1083	897.8	420	13.56	0.11	2.809	0.0747	648.1
215	0.37	0.35	2.120	0.1075	893.1	425	14.38	0.11	2.842	0.0739	639.4
220	0.42	0.34	2.134	0.1067	888.3						

Figure F.3: Saturated vapor properties of Dowtherm A[15]

Table 5—Saturated Vapor Properties of DOWTHERM A Fluid (SI Units)

TEMP °C	VAPOR PRESSURE bar	LIQUID ENTHALPY kJ/kg	LATENT HEAT kJ/kg	VAPOR ENTHALPY kJ/kg	VAPOR DENSITY kg/m³	VAPOR VISCOSITY mPa sec	VAPOR THERMAL COND. W/mK	Z_{VAPOR}	SPECIFIC HEAT (c_p) kJ/kg K	RATIO OF SPECIFIC HEATS c_p/c_v
12	0.00	0.0	409.0	409.0		0.0053	0.0074	1.000	1.032	1.050
15	0.00	4.9	407.2	412.1		0.0054	0.0075	1.000	1.044	1.050
20	0.00	13.1	404.4	417.4		0.0055	0.0078	1.000	1.062	1.050
25	0.00	21.3	401.5	422.8		0.0056	0.0081	1.000	1.081	1.049
30	0.00	29.5	398.8	428.3		0.0057	0.0084	1.000	1.100	1.048
35	0.00	37.7	396.1	433.8		0.0058	0.0086	1.000	1.118	1.047
40	0.00	46.0	393.4	439.5		0.0059	0.0089	1.000	1.137	1.046
45	0.00	54.4	390.9	445.2	0.0011	0.0060	0.0092	1.000	1.155	1.045
50	0.00	62.7	388.3	451.0	0.0015	0.0061	0.0095	1.000	1.173	1.045
55	0.00	71.2	385.8	457.0	0.0021	0.0062	0.0098	1.000	1.191	1.044
60	0.00	79.6	383.4	463.0	0.0029	0.0062	0.0101	1.000	1.209	1.043
65	0.00	88.1	380.9	469.1	0.0040	0.0063	0.0104	1.000	1.227	1.043
70	0.00	96.7	378.6	475.2	0.0053	0.0064	0.0107	1.000	1.245	1.042
75	0.00	105.3	376.2	481.5	0.0072	0.0065	0.0110	1.000	1.262	1.041
80	0.00	114.0	373.9	487.9	0.0095	0.0066	0.0113	1.000	1.280	1.041
85	0.00	122.7	371.6	494.3	0.0125	0.0067	0.0116	1.000	1.297	1.040
90	0.00	131.5	369.4	500.8	0.0162	0.0068	0.0120	0.999	1.315	1.040
95	0.00	140.3	367.1	507.4	0.0210	0.0069	0.0123	0.999	1.332	1.039
100	0.01	149.2	364.9	514.1	0.0268	0.0070	0.0126	0.999	1.349	1.039
105	0.01	158.1	362.7	520.9	0.0341	0.0071	0.0129	0.999	1.366	1.038
110	0.01	167.1	360.6	527.7	0.0430	0.0072	0.0133	0.999	1.382	1.038
115	0.01	176.2	358.4	534.6	0.0538	0.0073	0.0136	0.999	1.399	1.037
120	0.01	185.4	356.3	541.6	0.0669	0.0074	0.0139	0.998	1.416	1.037
125	0.02	194.6	354.1	548.7	0.0826	0.0075	0.0143	0.998	1.432	1.037
130	0.02	203.8	352.0	555.9	0.1013	0.0076	0.0146	0.998	1.448	1.036
135	0.03	213.2	349.9	563.1	0.1235	0.0077	0.0149	0.997	1.464	1.036
140	0.03	222.6	347.8	570.4	0.1498	0.0078	0.0153	0.997	1.481	1.036
145	0.04	232.1	345.7	577.8	0.1806	0.0078	0.0156	0.996	1.497	1.035
150	0.05	241.6	343.6	585.2	0.2165	0.0079	0.0160	0.995	1.512	1.035
155	0.06	251.2	341.5	592.7	0.2583	0.0080	0.0163	0.995	1.528	1.035
160	0.07	260.9	339.4	600.3	0.3065	0.0081	0.0167	0.994	1.544	1.035
165	0.08	270.7	337.3	608.0	0.3621	0.0082	0.0170	0.993	1.560	1.035
170	0.09	280.5	335.2	615.7	0.4257	0.0083	0.0174	0.992	1.575	1.034
175	0.11	290.4	333.1	623.5	0.4984	0.0084	0.0178	0.991	1.590	1.034
180	0.13	300.4	331.0	631.3	0.5809	0.0085	0.0181	0.990	1.606	1.034
185	0.15	310.4	328.8	639.2	0.6744	0.0086	0.0185	0.988	1.621	1.034
190	0.18	320.5	326.7	647.2	0.7798	0.0087	0.0189	0.987	1.636	1.034
195	0.21	330.7	324.6	655.2	0.8984	0.0088	0.0192	0.985	1.651	1.034
200	0.24	340.9	322.4	663.3	1.031	0.0089	0.0196	0.984	1.666	1.034
205	0.28	351.2	320.2	671.5	1.179	0.0090	0.0200	0.982	1.681	1.034
210	0.32	361.6	318.0	679.7	1.344	0.0091	0.0204	0.980	1.696	1.034
215	0.37	372.1	315.8	687.9	1.528	0.0092	0.0207	0.978	1.711	1.034
220	0.42	382.6	313.6	696.2	1.730	0.0093	0.0211	0.975	1.726	1.034
225	0.48	393.2	311.4	704.6	1.954	0.0094	0.0215	0.973	1.741	1.034
230	0.54	403.9	309.1	713.0	2.201	0.0095	0.0219	0.970	1.755	1.034
235	0.61	414.6	306.8	721.4	2.471	0.0096	0.0223	0.967	1.770	1.035
240	0.69	425.4	304.5	729.9	2.768	0.0097	0.0227	0.964	1.785	1.035
245	0.77	436.3	302.1	738.4	3.092	0.0098	0.0231	0.961	1.799	1.035
250	0.87	447.2	299.8	747.0	3.446	0.0099	0.0234	0.958	1.814	1.036
255	0.97	458.2	297.4	755.6	3.831	0.0100	0.0238	0.954	1.829	1.036
257.1	1.01	462.9	296.4	759.2	4.003	0.0100	0.0240	0.953	1.835	1.036
260	1.08	469.3	294.9	764.3	4.250	0.0101	0.0242	0.951	1.843	1.036
265	1.20	480.5	292.5	773.0	4.704	0.0102	0.0246	0.947	1.858	1.037
270	1.33	491.7	290.0	781.7	5.196	0.0103	0.0250	0.942	1.872	1.037
275	1.48	503.0	287.5	790.4	5.727	0.0104	0.0254	0.938	1.887	1.038
280	1.63	514.3	284.9	799.2	6.301	0.0105	0.0258	0.934	1.902	1.038
285	1.80	525.8	282.3	808.1	6.920	0.0106	0.0263	0.929	1.916	1.039
290	1.98	537.3	279.6	816.9	7.586	0.0107	0.0267	0.924	1.931	1.040
295	2.17	548.8	277.0	825.8	8.302	0.0108	0.0271	0.919	1.946	1.041
300	2.38	560.5	274.2	834.7	9.071	0.0109	0.0275	0.913	1.961	1.042
305	2.60	572.2	271.5	843.6	9.896	0.0110	0.0279	0.908	1.976	1.042
310	2.84	583.9	268.6	852.6	10.78	0.0111	0.0283	0.902	1.991	1.044
315	3.10	595.8	265.8	861.5	11.73	0.0113	0.0287	0.896	2.006	1.045
320	3.37	607.7	262.8	870.5	12.74	0.0114	0.0292	0.889	2.021	1.046
325	3.66	619.7	259.8	879.5	13.82	0.0115	0.0296	0.883	2.036	1.047
330	3.96	631.7	256.8	888.6	14.98	0.0116	0.0300	0.876	2.052	1.048
335	4.29	643.9	253.7	897.6	16.21	0.0117	0.0304	0.869	2.068	1.050
340	4.64	656.1	250.5	906.6	17.53	0.0119	0.0309	0.862	2.084	1.052
345	5.00	668.4	247.3	915.7	18.93	0.0120	0.0313	0.854	2.100	1.053
350	5.39	680.7	244.0	924.7	20.43	0.0121	0.0317	0.846	2.116	1.055
355	5.80	693.1	240.6	933.8	22.03	0.0122	0.0322	0.838	2.133	1.057
360	6.24	705.7	237.2	942.8	23.73	0.0124	0.0326	0.830	2.150	1.060
365	6.69	718.2	233.6	951.9	25.54	0.0125	0.0331	0.821	2.168	1.062
370	7.18	730.9	230.0	960.9	27.47	0.0126	0.0335	0.812	2.186	1.065
375	7.68	743.7	226.3	970.0	29.53	0.0128	0.0340	0.803	2.204	1.068
380	8.22	756.5	222.5	979.0	31.73	0.0129	0.0344	0.793	2.224	1.071
385	8.78	769.4	218.6	988.0	34.07	0.0131	0.0349	0.783	2.244	1.075
390	9.37	782.4	214.5	997.0	36.58	0.0132	0.0354	0.773	2.264	1.079
395	9.99	795.5	210.4	1005.9	39.25	0.0134	0.0358	0.762	2.286	1.083
400	10.64	808.7	206.1	1014.8	42.11	0.0136	0.0363	0.751	2.309	1.088
405	11.32	822.0	201.7	1023.7	45.17	0.0138	0.0368	0.740	2.333	1.094
410	12.03	835.4	197.1	1032.5	48.45	0.0139	0.0373	0.728	2.359	1.100
415	12.78	848.9	192.4	1041.3	51.98	0.0141	0.0378	0.715	2.387	1.107
420	13.56	862.5	187.5	1050.0	55.77	0.0143	0.0383	0.703	2.417	1.115
425	14.38	876.3	182.3	1058.6	59.86	0.0145	0.0388	0.689	2.450	1.125

G

Appendix: Heat inflow oven calculations

G.0.1. Heat inflow profile of non-homogeneous part of oven

FLIR measurements were done at three different temperatures (T_{ev}) and at two different runs/days. Axial locations accessible were measured, which was between 0 and 0.048m from the left end of the central oven chamber. The averages of the two measurements at $T_{ev} = 300^{o}$C are shown in Figure G.1a. In this plot, the temperatures derived from wall sensors HF1 and HF2 are also shown. As those temperatures are measured inside the wall, Equation G.1 is used to calculate the outside wall temperature, which can consequently be compared with the values obtained by the thermographic camera. In this equation, r_w is the radial position of the wall temperature sensors, which is 0.024m. k_w is the temperature dependent thermal conductivity of the SS316 wall, which can be found in Appendix F.

$$T_{wo} = T_w + \frac{Q/\mathrm{d}z \ln\left(\frac{r_{wo}}{r_w}\right)}{2\pi k_w} \tag{G.1}$$

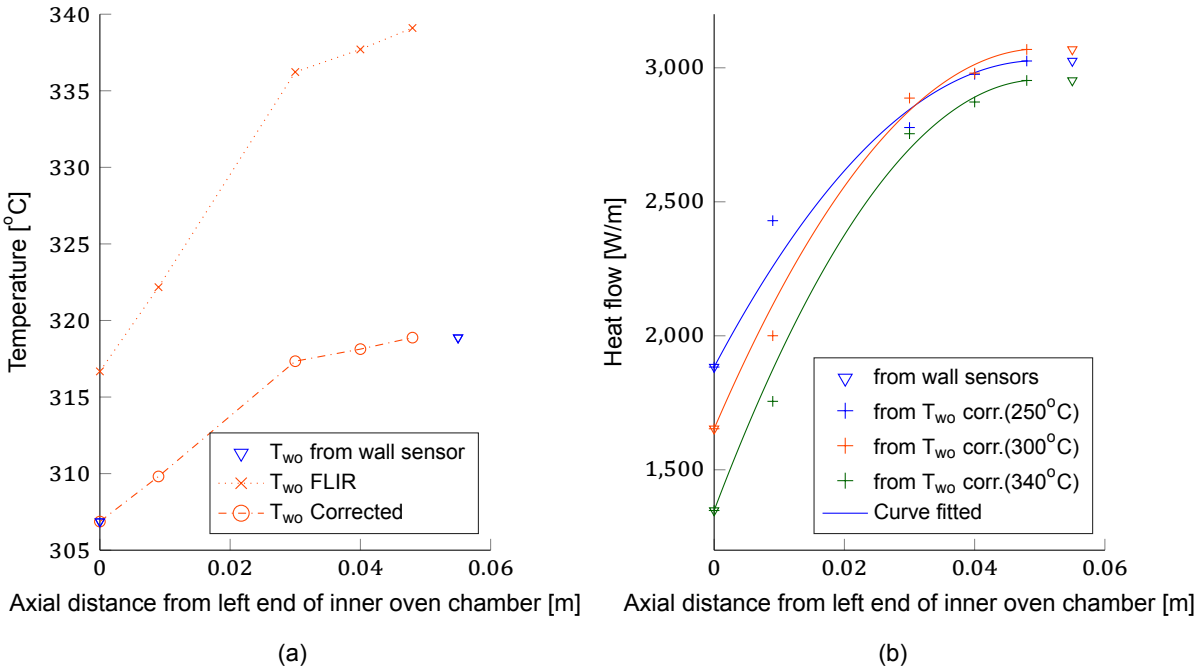

Figure G.1: Plots showing thermographic camera measurements at $T_{ev} = 300^{o}$C and its correction(a) and heat flow determination(b) at sides of central oven chamber. Power was 100%

One could see a significant difference between temperatures measured with the thermographic camera and the two points obtained from the wall sensors in Figure G.1a. This is most probably due to inaccuracy of the measurement method using the thermographic camera. The gap between upper and lower oven panel was small, through which had to be measured. Furthermore, escaping radiation through the gap was also likely to give higher values for the temperature. It was also difficult to measure perpendicular to the heat pipe. The thermographic camera is not very accurate itself, but due to the other inaccuracies, it was chosen to continue with this camera. The measured values were corrected to match with the value derived from the wall sensors at the sides of the measuring domain. For this, it is taken that the wall surface temperature stays equal from the most right measurement onward, from $z = 0.048$, as the gradient is relatively low at this point compared to at $z = 0$. The correction was done according to the following equation, in which T_{FLIR} are thermographically measured values and T_{wo} the values derived from the wall sensors:

$$T_{FLIR,corr.}(z) = \frac{T_{FLIR}(z) - T_{FLIR}(0)}{T_{FLIR}(0.048) - T_{FLIR}(0)}\Big(T_{wo}(0) - T_{wo}(0.055)\Big) + T_{wo}(0) \tag{G.2}$$

Now that an approximation of the outside wall temperature at multiple points in the non-homogeneous section is obtained, the local heat flow can be calculated using:

$$Q/\mathrm{d}z(z) = \frac{\Delta T(z) - \Delta T(0)}{\Delta T(0.048) - \Delta T(0)}\Big((Q/\mathrm{d}z)_{HF2} - (Q/\mathrm{d}z)_{HF1}\Big) + (Q/\mathrm{d}z)_{HF1} \tag{G.3}$$

Where $\Delta T(z) = T_{FLIR,corr.}(z) - T_{ev}$ and $(Q/\mathrm{d}z)_{HF1}$ is the heat flow per unit axial length measured by heat flux sensor 1. Consequently, curve fitting was applied to get to a function for the heat flow per unit axial length for each T_{ev} in the form of $Az^2 + Bz + C$. The obtained components were rewritten in terms of T_{ev}, $(Q/\mathrm{d}z)_{HF1}$ and $(Q/\mathrm{d}z)_{HF2}$. The result is shown in Figure G.1b and the obtained expression is given in Equation G.4.

$$Q/\mathrm{d}z(z) = -Az^2 + Bz + C \tag{G.4}$$

$$A = 2031T_{ev} - 50360$$

$$B = 20.833\Big((Q/\mathrm{d}z)_{HF2} - (Q/\mathrm{d}z)_{HF1}\Big) + 0.048A$$

$$C = (Q/\mathrm{d}z)_{HF1}$$

Integrating Equation G.4 results in the following expression for the heat input at the non-homogeneous heating part of the central oven chamber:

$$Q_{non-hom} = 0.0374T_{ev} + 0.024\Big((Q/\mathrm{d}z)_{HF1} + (Q/\mathrm{d}z)_{HF2}\Big) - 0.9282 \tag{G.5}$$

Where T_{ev} is the inside evaporator temperature in ^oC.

Appendix: Additional experimental results

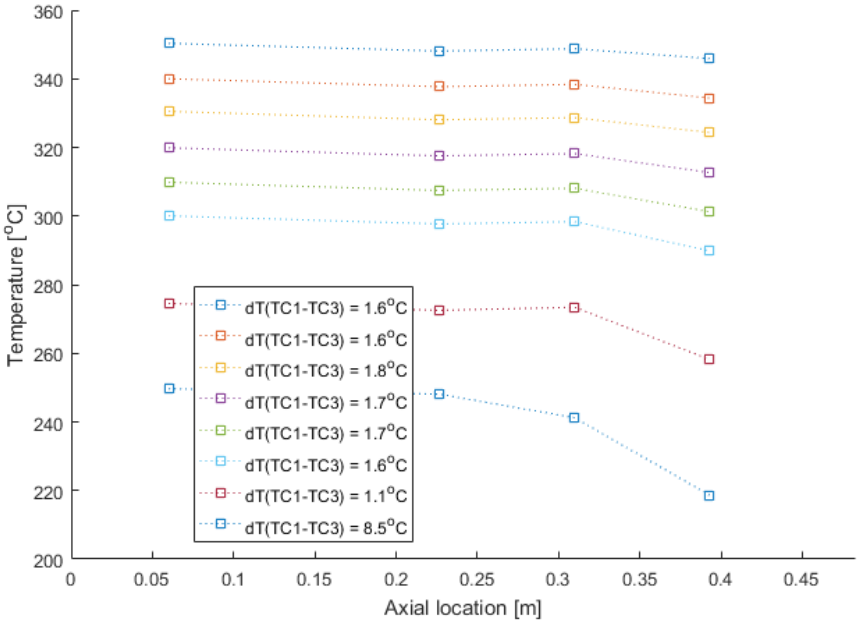

Figure H.1: Graph showing internal temperature measurements at different axial locations of the heat pipe. In the legend, the difference between TC1(left) and TC3 is indicated. The error of the thermocouples is $2.2^{o}C$. Operating conditions: $\chi = 0.14$, $m_g \sim 0.15g$, 200rpm and 100% lamp power* except for lowest temperature.

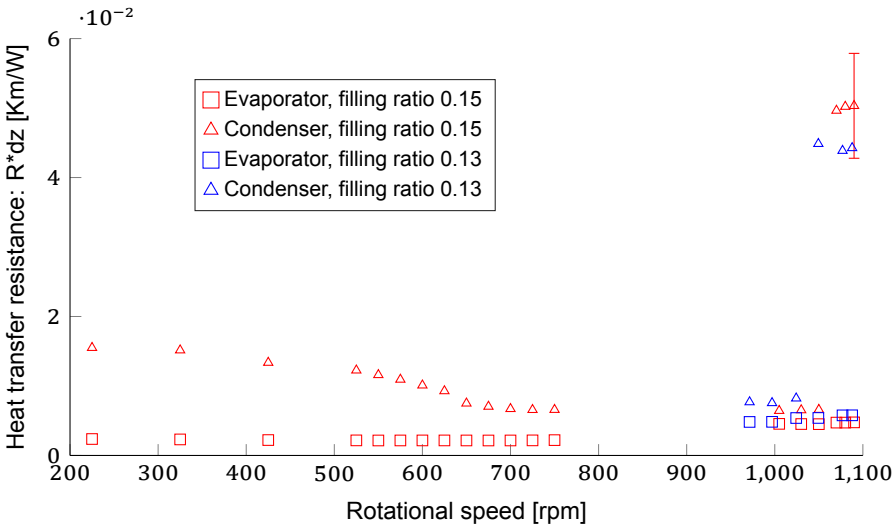

Figure H.2: Resistances of condenser and evaporator for different filling ratios at 340^oC(red) and 350^oC(blue). Values between 750 and 975rpm are not included due to dryout occurring at these rotational speeds

Appendix: Derivation model equations

$$ln(x_v) = -\frac{h_{fg}}{R}\left(\frac{1}{T_v} - \frac{1}{T_{ev}}\right) \tag{I.1}$$

$$x_v = e^{-\frac{h_{fg}}{R}\left(\frac{1}{T_v} - \frac{1}{T_{ev}}\right)} \tag{I.2}$$

$$x_g = 1 - e^{-\frac{h_{fg}}{R}\left(\frac{1}{T_v} - \frac{1}{T_{ev}}\right)} \tag{I.3}$$

$$e^{-\phi} = 1 - e^{-\frac{T_0}{T_{ev}}\left(\frac{T_{ev}}{T_v} - 1\right)} \tag{I.4}$$

where $T_0 = h_{fg}/R$

Derivation to z:

$$\frac{\mathrm{d}e^{-\phi}}{\mathrm{d}z} = \frac{\mathrm{d}}{\mathrm{d}z}\left(1 - e^{-\frac{T_0}{T_{ev}}\left(\frac{T_{ev}}{T_v} - 1\right)}\right) \tag{I.5}$$

$$\frac{\mathrm{d}\phi}{\mathrm{d}z}e^{-\phi} = e^{T_0/T_{ev}}\frac{\mathrm{d}}{\mathrm{d}z}\left(e^{-T_0/T_v}\right) \tag{I.6}$$

$$\frac{\mathrm{d}\phi}{\mathrm{d}z}e^{-\phi} = \frac{T_0}{T_v^2}\frac{\mathrm{d}T_v}{\mathrm{d}z}e^{-\frac{T_0}{T_{ev}}\left(\frac{T_{ev}}{T_v} - 1\right)} \tag{I.7}$$

$$\frac{\mathrm{d}T_v}{\mathrm{d}z} = \frac{\mathrm{d}\phi}{\mathrm{d}z}\frac{T_v^2}{T_0}\frac{e^{-\phi}}{e^{-\frac{T_0}{T_{ev}}\left(\frac{T_{ev}}{T_v} - 1\right)}} \tag{I.8}$$

From equation I.4 follows:

$$\frac{\mathrm{d}T_v}{\mathrm{d}z} = \frac{\mathrm{d}\phi}{\mathrm{d}z}\frac{T_v^2}{T_0}\frac{e^{-\phi}}{1 - e^{-\phi}} \tag{I.9}$$

By combining this equation with equation 5.19:

$$\frac{\mathrm{d}T_v}{\mathrm{d}z} = -\frac{\dot{m}}{cA_vM_vD}\frac{T_v^2}{T_0}\frac{e^{-\phi}}{1 - e^{-\phi}} \tag{I.10}$$

The second derivative then is obtained by differentiating with respect to z once more:

$$\frac{\mathrm{d}^2T_v}{\mathrm{d}z^2} = \frac{\mathrm{d}}{\mathrm{d}z}\left(-\frac{\dot{m}}{cA_vM_vD}\frac{T_v^2}{T_0}\frac{e^{-\phi}}{1 - e^{-\phi}}\right) \tag{I.11}$$

$$\frac{\mathrm{d}^2T_v}{\mathrm{d}z^2} = -\frac{1}{cA_vM_vDT_0}\frac{\mathrm{d}}{\mathrm{d}z}\left(\dot{m}T_v^2\frac{e^{-\phi}}{1-e^{-\phi}}\right) \tag{I.12}$$

Where:

$$\frac{\mathrm{d}}{\mathrm{d}z}\left(\dot{m}T_v^2\frac{e^{-\phi}}{1-e^{-\phi}}\right) = \frac{\mathrm{d}\dot{m}}{\mathrm{d}z}T_v^2\frac{e^{-\phi}}{1-e^{-\phi}} + 2\dot{m}T_v\frac{\mathrm{d}T_v}{\mathrm{d}z}\frac{e^{-\phi}}{1-e^{-\phi}} + \dot{m}T_v^2\frac{\mathrm{d}}{\mathrm{d}z}\left(\frac{e^{-\phi}}{1-e^{-\phi}}\right)$$

In which the equation below can be inserted in the above equation:

$$\frac{\mathrm{d}}{\mathrm{d}z}\left(\frac{e^{-\phi}}{1-e^{-\phi}}\right) = \frac{\mathrm{d}\phi}{\mathrm{d}z}\frac{\frac{\mathrm{d}(e^{-\phi})}{\mathrm{d}\phi}(1-e^{-\phi}) - e^{-\phi}\frac{\mathrm{d}(1-e^{-\phi})}{\mathrm{d}\phi}}{(1-e^{-\phi})^2} = -\frac{\mathrm{d}\phi}{\mathrm{d}z}\frac{e^{-\phi}}{(1-e^{-\phi})^2}$$

$$\frac{\mathrm{d}}{\mathrm{d}z}\left(\dot{m}T_v^2\frac{e^{-\phi}}{1-e^{-\phi}}\right) = \frac{\mathrm{d}\dot{m}}{\mathrm{d}z}T_v^2\frac{e^{-\phi}}{1-e^{-\phi}} + 2\dot{m}T_v\frac{\mathrm{d}T_v}{\mathrm{d}z}\frac{e^{-\phi}}{1-e^{-\phi}} - \dot{m}T_v^2\frac{\mathrm{d}\phi}{\mathrm{d}z}\frac{e^{-\phi}}{(1-e^{-\phi})^2}$$

After substituted in Equation I.12:

$$\frac{\mathrm{d}^2T_v}{\mathrm{d}z^2} = -\frac{1}{cA_vM_vDT_0}\left(\frac{\mathrm{d}\dot{m}}{\mathrm{d}z}T_v^2\frac{e^{-\phi}}{1-e^{-\phi}} + 2\dot{m}T_v\frac{\mathrm{d}T_v}{\mathrm{d}z}\frac{e^{-\phi}}{1-e^{-\phi}} - \dot{m}T_v^2\frac{\mathrm{d}\phi}{\mathrm{d}z}\frac{e^{-\phi}}{(1-e^{-\phi})^2}\right) \tag{I.13}$$

Expressions for $\mathrm{d}\phi/\mathrm{d}z$ and $\mathrm{d}T_v/\mathrm{d}z$ given by Equation 5.19 and 5.24 respectively can be filled in. This finally results in an expression for $\mathrm{d}^2T_v/\mathrm{d}z^2$ as a function of T_v, ϕ, $\dot{m}$ and $\mathrm{d}\dot{m}/\mathrm{d}z$.

$$\frac{\mathrm{d}^2T_v}{\mathrm{d}z^2} = -\frac{1}{cA_vM_vDT_0}\left(\frac{\mathrm{d}\dot{m}}{\mathrm{d}z}T_v^2\frac{e^{-\phi}}{1-e^{-\phi}} - 2\dot{m}T_v\frac{\dot{m}}{cA_vM_vD}\frac{T_v^2}{T_0}\frac{e^{-\phi}}{1-e^{-\phi}}\frac{e^{-\phi}}{1-e^{-\phi}} + \dot{m}T_v^2\frac{\dot{m}}{cA_vM_vD}\frac{e^{-\phi}}{(1-e^{-\phi})^2}\right)$$

$$\frac{\mathrm{d}^2T_v}{\mathrm{d}z^2} = -\frac{1}{cA_vM_vDT_0}\left(\frac{\mathrm{d}\dot{m}}{\mathrm{d}z}T_v^2\frac{e^{-\phi}}{1-e^{-\phi}} - 2\frac{\dot{m}^2}{cA_vM_vD}\frac{T_v^3}{T_0}\frac{e^{-2\phi}}{(1-e^{-\phi})^2} + T_v^2\frac{\dot{m}^2}{cA_vM_vD}\frac{e^{-\phi}}{(1-e^{-\phi})^2}\right)$$

$$\frac{\mathrm{d}^2T_v}{\mathrm{d}z^2} = -\frac{1}{cA_vM_vD}\frac{T_v^2}{T_0}\frac{e^{-\phi}}{1-e^{-\phi}}\frac{\mathrm{d}\dot{m}}{\mathrm{d}z} + \left(\frac{\dot{m}}{cA_vM_vD}\right)^2\frac{T_v^2}{T_0}\left(2\frac{T_v}{T_0}\frac{e^{-2\phi}}{(1-e^{-\phi})^2} - \frac{e^{-\phi}}{(1-e^{-\phi})^2}\right) \tag{I.14}$$

Equation I.14 is subsequently used in Chapter 5.

J

Appendix: Computational efficiency

As one of the requirements of the model is its computational efficiency, the influence of mesh size on the solution has been tested, such that a mesh size can be chosen which results in efficient and accurate modelling. A base case has been set with a fine mesh and subsequently coarser meshes are compared with the base case. The difference between the two solutions is considered the error due to the mesh size. x_g and $\dot{m}$ are considered of main relevance on the results. The results are presented in Table J.1.

A mesh size of 1000/mm showed an error of well below 1% for both x_g and $\dot{m}$. A coarser mesh results in significant increasing of the error. One could conclude that a mesh of 100/mm results in an entirely different solution. 1000/mm is considered to result in an solution which is accurate enough.

Table J.1: Deviations in solutions of x_g and $\dot{m}$ when a coarser mesh is used compared to the base case. The maximum deviation is stated, with the relative error between the brackets

Mesh density	$\Delta x_{g,max}$	$\Delta \dot{m}_{max}$
Base case (10000/mm)	0	0
1000/mm	$6 * 10^{-5}$ (0.06%)	$2 * 10^{-7}$ (0.13%)
500/mm	$9.2 * 10^{-4}$ (0.9%)	$4.1 * 10^{-6}$ (2.7%)
100/mm	0.05 (50%)	0.00045 (300%)

Appendix: Condensation limit wall model derivation

$$-\frac{dx_v}{dr}cDM2\pi r_v = \frac{d^2x_v}{dz^2}cDM(\pi r_v^2 - \pi r_x^2) \tag{K.1}$$

$$-\frac{dx_v}{dr}2r_v = \frac{d^2x_v}{dz^2}(r_v^2 - r_x^2) \tag{K.2}$$

$$-dx = (\frac{1}{2}\frac{d^2x_v}{dz^2}r_v - \frac{1}{2}\frac{d^2x_v}{dz^2}\frac{r_x^2}{r_v})dr \tag{K.3}$$

$$x = \int \frac{1}{2}\frac{d^2x_v}{dz^2}r_x^2\frac{1}{r}dr - \int \frac{1}{2}\frac{d^2x_v}{dz^2}rdr \tag{K.4}$$

$$x = \frac{1}{2}\frac{d^2x_v}{dz^2}r_x^2 ln(r) - \frac{1}{4}\frac{d^2x_v}{dz^2}r^2 + C_1 \tag{K.5}$$

$$@r = r_v \rightarrow x = 0 \quad @limit \tag{K.6}$$

$$0 = \frac{1}{2}\frac{d^2x_v}{dz^2}r_x^2 ln(r_v) - \frac{1}{4}\frac{d^2x_v}{dz^2}r_v^2 + C_1 \tag{K.7}$$

$$C_1 = \frac{1}{4}\frac{d^2x_v}{dz^2}r_v^2 - \frac{1}{2}\frac{d^2x_v}{dz^2}r_x^2 ln(r_v) \tag{K.8}$$

$$x_v = \frac{1}{2}\frac{d^2x_v}{dz^2}r_x^2 ln(\frac{r}{r_v}) + \frac{1}{4}\frac{d^2x_v}{dz^2}(r_v^2 - r^2) \tag{K.9}$$

The average mole fraction can then be expressed by the following equation. From r = 0 –> r_x, x_v is constant. Between r_x and r_v, it is given by Equation K.9.

$$x_{avg} = \frac{\int_{r_x}^{r_v} x_v 2\pi r dr + x(r_x)\pi r_x^2}{(1-\chi)\pi r_v^2} \tag{K.10}$$

$$\int_{r_x}^{r_v} x_v 2\pi r dr = \frac{d^2x_v}{dz^2}r_x^2\pi \int ln(\frac{r}{r_v})rdr + \frac{1}{2}\frac{d^2x_v}{dz^2}\pi r_v^2 \int rdr - \frac{1}{2}\frac{d^2x_v}{dz^2}\pi \int r^3 dr \tag{K.11}$$

where:

$$\int_{r_x}^{r_v} ln(\frac{r}{r_v})rdr = ln(\frac{r}{r_v}) \int rdr - \frac{d}{dr}(ln(\frac{r}{r_v}))(\int rdr)dr \tag{K.12}$$

$$\int_{r_x}^{r_v} ln(\frac{r}{r_v})rdr = ln(\frac{r}{r_v})\frac{1}{2}r^2 - \int \frac{1}{r}\frac{1}{2}r^2dr \tag{K.13}$$

$$\int_{r_x}^{r_v} ln(\frac{r}{r_v})rdr = -ln(\frac{r_x}{r_v})\frac{1}{2}r_x^2 + \frac{1}{4}r_x^2 - \frac{1}{4}r_v^2 \tag{K.14}$$

Which can be substituted in Equation K.11:

$$\int x_v 2\pi r dr = \frac{d^2x_v}{dz^2}r_x^2\pi(\frac{1}{4}r_x^2 - \frac{1}{4}r_v^2 - ln(\frac{r_x}{r_v})\frac{1}{2}r_x^2) + \frac{1}{4}\frac{d^2x_v}{dz^2}\pi r_v^2(r_v^2 - r_x^2) - \frac{1}{8}\frac{d^2x_v}{dz^2}\pi(r_v^4 - r_x^4) \tag{K.15}$$

$$\int_{r_x}^{r_v} x_v 2\pi r dr = \frac{d^2x_v}{dz^2}\pi r_x^2(-\frac{1}{2}r_v^2 + \frac{3}{8}r_x^2 - \frac{1}{2}r_x^2 ln(\frac{r_x}{r_v}) + \frac{1}{8}\frac{d^2x_v}{dz^2}\pi r_v^4) \tag{K.16}$$

Subsequently,

$$\int x(r_x)2\pi r dr = \int \frac{1}{2}\frac{d^2x_v}{dz^2}r_x^2 ln(\frac{r_x}{r_v})2\pi r dr + \int \frac{1}{4}\frac{d^2x_v}{dz^2}(r_v^2 - r_x^2)2\pi r dr \tag{K.17}$$

$$\int_0^{r_x} x(r_x)2\pi r dr = \frac{1}{2}\frac{d^2x_v}{dz^2}r_x^4 ln(\frac{r_x}{r_v})\pi + \frac{1}{4}\frac{d^2x_v}{dz^2}r_v^2 r_x^2\pi - \frac{1}{4}\frac{d^2x_v}{dz^2}r_x^4\pi \tag{K.18}$$

Equation K.10 becomes:

$$x_{avg} = \frac{\frac{1}{2}\frac{d^2x_v}{dz^2}r_x^4 ln(\frac{r_x}{r_v})\pi + \frac{1}{4}\frac{d^2x_v}{dz^2}r_v^2 r_x^2\pi - \frac{1}{4}\frac{d^2x_v}{dz^2}r_x^4\pi + \frac{d^2x_v}{dz^2}\pi(r_x^2(-\frac{1}{2}r_v^2 + \frac{3}{8}r_x^2 - \frac{1}{2}r_x ln(\frac{r_x}{r_v})) + \frac{1}{8}r_v^4}{\pi r_v^2} \tag{K.19}$$

$$x_{avg} = \frac{d^2x_v}{dz^2}(\frac{1}{8}r_v^2 + r_x^2(\frac{1}{8}\frac{r_x^2}{r_v^2} - \frac{1}{4})) \tag{K.20}$$

r_x can subsequently be determined:

$$\frac{d\dot{m}}{dz} = \pi(r_v^2 - r_x^2)cDM\frac{d^2x_v}{dz^2} \tag{K.21}$$

$$r_x^2 = r_v^2 - \frac{\frac{d\dot{m}}{dz}}{\pi cDM\frac{d^2x_v}{dz^2}} \tag{K.22}$$

$$x_{avg} = \frac{d^2x_v}{dz^2}(\frac{1}{8}r_v^2 - \frac{1}{4}r_v^2 + \frac{1}{4}\frac{\frac{d\dot{m}}{dz}}{\pi cDM\frac{d^2x_v}{dz^2}} + \frac{1}{8}\frac{r_x^2}{r_v^2}) \tag{K.23}$$

$$r_x^4 = (r_v^2 - \frac{\frac{d\dot{m}}{dz}}{\pi cDM\frac{d^2x_v}{dz^2}})^2 = r_v^4 + \frac{(\frac{d\dot{m}}{dz})^2}{\pi^2c^2D^2M^2(\frac{d^2x_v}{dz^2})^2} \tag{K.24}$$

$$x_{avg} = \frac{d^2x_v}{dz^2}(\frac{1}{8}r_v^2 - \frac{1}{4}r_v^2 + \frac{1}{4}\frac{\frac{d\dot{m}}{dz}}{\pi cDM\frac{d^2x_v}{dz^2}} + \frac{1}{8}r_v^2 + \frac{1}{8}\frac{(\frac{d\dot{m}}{dz})^2}{r_v^2\pi^2c^2D^2M^2(\frac{d^2x_v}{dz^2})^2} - \frac{1}{4}\frac{\frac{d\dot{m}}{dz}}{\pi cDM\frac{d^2x_v}{dz^2}}) \tag{K.25}$$

$$x_{avg} = \frac{d^2x_v}{dz^2}(\frac{1}{8}(\frac{\frac{d\dot{m}}{dz}}{r_v\pi cDM\frac{d^2x_v}{dz^2}})^2) \tag{K.26}$$

$$\frac{d\dot{m}}{dz} = \sqrt{8x_{v_{avg}}\frac{d^2x_v}{dz^2}}r_v c\pi DM \tag{K.27}$$

These model equations were derived when the sign of $\dot{m}$ was still the other way around. Conversion to new:

$$\frac{d\dot{m}}{dz} = -\sqrt{8x_{v_{avg}}\frac{d^2x_v}{dz^2}r_v c\pi DM} \tag{K.28}$$

Appendix: Modelling additional information and graphs

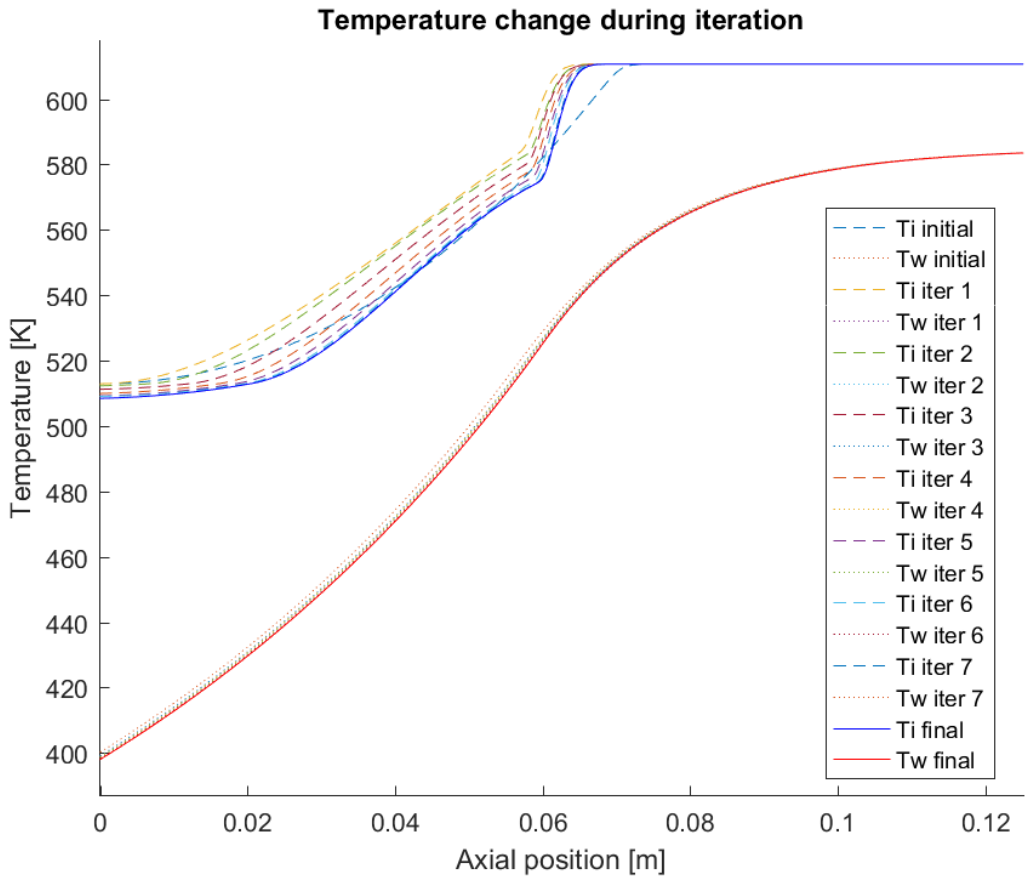

Figure L.1: Graph showing iteration process of combined model for TU Delft experimental setup. The result was obtained after eight iterations.

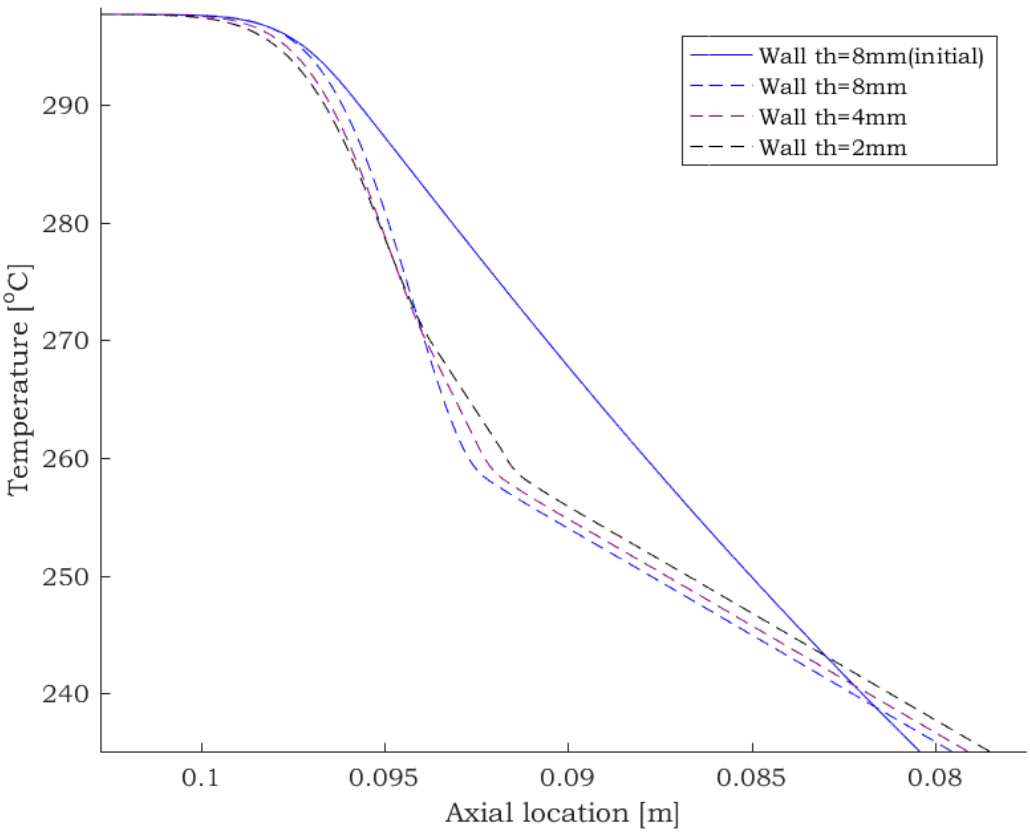

Figure L.2: Graph showing internal temperature T_v for different wall thicknesses. The initial case is as stated in Table 5.3. Different values for R_2 (Eq. 5.38): 0.42(8mm wall), 0.95(4mm wall) and 1.99(2mm wall)

Figure L.3: Values of TU Delft experimental setup for determination of dimensionless numbers of Eq. 5.37 & 5.38

Values of dimensionless parameters for experimental setup

TU Delft setup @ 300°C (2.38 bar)	Upstream front	In front (x_v = 0.95 – 0.05)	Downstream front
D [m^2/s]	$7.93*10^{-6}$		
A_v [m^2]	0.0013		
A_w [m^2]	0.0013		
ρ_v [kg/m^3]	9.071		
h_{fg} [J/kg]	274200		
R [J/kgK]	50.08		
k_w [W/(m-K)]	16.3		
k [W/(m-K)]	0.0275(DowA)	0.0356 (avg.)	0.0444 (Air,refp)
T [K]	573	570-450	370
v [m/s]	0.05	0.007-0.00003	0
x_v	1	0.95-0.05	0
dx_v/dz [1/m]	0	43-3.7	0
dx_v/dT [1/K]	0.017	0.016-0.0020	0.00021
dT/dz [K/m]	0	2410-1850	0

TU Delft setup @ 300°C	Upstream front	In front	Downstream front
R_1 (convection / mass diffusion)	∞	19.5-0.0511	*no conv*
R_2 (convection / wall conductance)	∞	0.421-0.000124	*no conv*
R_3 (diffusion / wall conductance)	0.0206	0.0194-0.00240	0.000256
R_4 (convection / vapor or gas conductance)	∞	193-0.0566	*no conv*
R_5 (diffusion / vapor or gas conductance)	12.2	8.88-1.10	0.0939

Figure L.4: Values of Edwards & Marcus experimental setup for determination of dimensionless numbers of Eq. 5.37 & 5.38

Comparison with literature

Edwards & Marcus (water, air 1.2525 bar)	Upstream front	In front (x_v = 0.95 – 0.05)	Downstream front
D [m^2/s]	$0.41*10^{-4}$		
A_v [m^2]	$1.086*10^{-4}$		
A_w [m^2]	$3.8596*10^{-5}$		
ρ_v [kg/m^3]	0.7272		
h_{fg} [J/kg]	2240500		
R [J/kgK]	461.5		
k_w [W/(m-K)]	16.1		
k [W/(m-K)]	0.02578 (water)	0.02610 (avg.)	0.02632 (air)
T [K]	379.2	378 - 307	299
v [m/s]	0.096	0.011–0.000040	0
x_v	1	0.95-0.05	0
dx_v/dz [1/m]	0	14 – 0.93	0
dx_v/dT [1/K]	0.034	0.033 – 0.0025	0.0018
dT/dz [K/m]	0	429 - 363	0

Edwards & Marcus (water, air 1.2525 bar)	Upstream front	In front	Downstream front
R_1 (convection / mass diffusion)	∞	18.2 – 0.0525	*no conv*
R_2 (convection / wall conductance)	∞	6.94 – 0.00160	*no conv*
R_3 (diffusion / wall conductance)	0.397	0.385 – 0.0292	0.0210
R_4 (convection / vapor or gas conductance)	∞	1521 – 0.344	*no conv*
R_5 (diffusion / vapor or gas conductance)	88.1	84.5 – 6.40	4.57

Figure L.5: Values of experiment reported by Harley for determination of dimensionless numbers of Eq. 5.37 & 5.38

Harley (Sodium, argon)	Upstream front	In front (x_v = 0.95 – 0.05 – 0.025)	Downstream front
D [m^2/s]	0.0204 (p = 1250pa, T = 717.5K)		
A_v [m^2]	$1.267*10^{-4}$		
A_w [m^2] (wall + wick)	$2.604*10^{-4}$		
ρ_v [kg/m^3]	0.003		
h_{fg} [J/kg]	4370000		
R [J/kgK]	361.6		
C = k_w * A_w [Wm/K]	0.0081		
k [W/(m-K)]	0.034 (Sodium, est.)	0.028 (avg)	0.0225 (Argon)
T [K]	782.2	780 – 655 - 634	339.6
V [m/s]	94	27 – 0.48 – 0.07	0
x_v	1	0.95-0.05-0.025	0
dx_v/dz [1/m]	0	8.5 – 3.7-1.8	0
	0.020	0.019 – 0.0014 – 0.00081	$2*10^{-10}$
dT/dz [K/m]	0	2950 – 2634 - 2467	0

Harley (Sodium, Argon)	Upstream front	In front	Downstream front
R_1 (convection / mass diffusion)	∞	148 – 0.318 – 0.0477	*no conv*
R_2 (convection / wall conductance)	∞	1.78 – 0.00190	*no conv*
R_3 (diffusion / wall conductance)	0.0837	0.0795 – 0.0059	$8.37*10^{-10}$
R_4 (convection / vapor or gas conductance)	∞	4071 – 4.27	*no conv*
R_5 (diffusion / vapor or gas conductance)	157	181 – 13.4	$2.38*10^{-6}$